# NASA TECHNICAL NOTE

NASA TN D-4961

# EFFECT OF UNIT REYNOLDS NUMBER, NOSE BLUNTNESS, ANGLE OF ATTACK, AND ROUGHNESS ON TRANSITION ON A 5° HALF-ANGLE CONE AT MACH 8

by P. Calvin Stainback

Langley Research Center
Langley Station, Hampton, Va.

# EFFECT OF UNIT REYNOLDS NUMBER, NOSE BLUNTNESS,

# ANGLE OF ATTACK, AND ROUGHNESS ON TRANSITION

# ON A 5° HALF-ANGLE CONE AT MACH 8

By P. Calvin Stainback

Langley Research Center
Langley Station, Hampton, Va.

NATIONAL AERONAUTICS AND SPACE ADMINISTRATION

# EFFECT OF UNIT REYNOLDS NUMBER, NOSE BLUNTNESS, ANGLE OF ATTACK, AND ROUGHNESS ON TRANSITION ON A 5° HALF-ANGLE CONE AT MACH 8

By P. Calvin Stainback
Langley Research Center

## SUMMARY

A 5° half-angle cone has been tested at a nominal free-stream Mach number of 8 over a range of local, sharp cone unit Reynolds numbers from about $4.5 \times 10^6$ per meter $\left(1.3 \times 10^6 \text{ per foot}\right)$ to $4.5 \times 10^7$ per meter $\left(1.3 \times 10^7 \text{ per foot}\right)$ in a conventional blow-down tunnel. The nominal ratio of wall temperature to free-stream total temperature was about 0.4. The purpose of the investigation was to determine the effect of unit Reynolds number, nose bluntness, angle of attack, and roughness on the beginning of transition and on laminar and turbulent heating. The results obtained with the smooth models indicated that there was an increase in the transition Reynolds number with increasing unit Reynolds number and a rearward movement of the location of transition with increasing nose bluntness and angle of attack for the windward ray. Although the hypersonic laminar boundary layer could be tripped with various types of roughness elements, large three-dimensional elements caused circumferential nonuniformities in the heat-transfer distribution around the cone for large distances into the turbulent boundary-layer region. The local transition Reynolds numbers for all bluntnesses (including the sharp tip cone) were correlated reasonably well as a single function of local unit Reynolds number if the local flow quantities were obtained from boundary-layer solutions with variable stream entropy effects included. Also, the agreement between laminar heat-transfer data and theory, in the form of Stanton number as a function of Reynolds number, appeared to be improved if variable-entropy effects were taken into account.

## INTRODUCTION

The optimum design of high performance missiles and spacecraft requires a better understanding of problems associated with transition and turbulent flow in the hypersonic flow region. These problems include the accurate prediction of the initial locations of transition and fully developed turbulent flow and the heating rates and shear stresses in the fully developed turbulent flow regions. The present report is limited to the determination of the location of the beginning of transition without regard to facility turbulence

levels and frequencies which are presently unknown. Although many factors influence the transition Reynolds number, the only ones considered herein are unit Reynolds number, nose bluntness, angle of attack, and roughness.

Until recently, very little data were available on the influence of these parameters on the location of transition for Mach numbers greater than 8. Potter and Whitfield (refs. 1 and 2) present data which include the effects of unit Reynolds number, nose bluntness, and roughness on the location of transition at Mach numbers up to 18. However, most of the data are limited to the lower Mach numbers. Palko, Burt, and Ray reported transition results obtained on a "sharp" flat plate at Mach numbers from 5 to 10 in reference 3. Deem and Murphy (ref. 4) have also reported transition data taken on a flat plate at Mach numbers from 5 to 10. Nagamatsu, Graber, and Sheer (refs. 5 and 6) have conducted tests on sharp and blunted cones with and without roughness at angles of attack and at Mach numbers up to 16 in a shock tunnel. Although these data (refs. 5 and 6) appear to be the most extensive transition data available at high Mach numbers, the results may be affected by the pressure gradient and upstream flow history caused by the conical nozzle in which the data were obtained.

McCauley, Saydah, and Bueche (ref. 7) have investigated the effects of spherical roughness elements, bluntness, and angle of attack on the beginning of transition on a cone at one value of unit Reynolds number.

Recently, there have been several investigations reported which have advanced our understanding of transition on simple bodies such as cones, flat plates, and hollow cylinders. Some of these investigations were reported in references 8 to 11.

The present paper, which supplements the results of these reports, presents the influence of various factors (unit Reynolds number, nose bluntness, angle of attack, and roughness) on the location of the beginning of transition on a $5^O$ half-angle cone at a nominal free-stream Mach number of 8 over a sharp-cone unit Reynolds number range from about $4.5 \times 10^6$ per meter $\left(1.3 \times 10^6 \text{ per foot}\right)$ to $4.5 \times 10^7$ per meter $\left(1.3 \times 10^7 \text{ per foot}\right)$ in a conventional blowdown tunnel. A quantitative measurement of the heat transfer behind roughness elements is also presented since some investigations (refs. 12 to 14) indicate that roughness could have a significant influence on conditions behind roughness elements while others (refs. 7 and 15) indicate that roughness elements produce only a small influence on the heat transfer aft of the elements.

Although there are several theories available (refs. 16 to 21) to describe the effect of bluntness-induced variable entropy on the fluid properties external to the boundary layer, the only transition data available where these effects are accounted for appears to be those of references 8 and 22. The present transition data were reduced and correlated in terms of the fluid properties exterior to the boundary layer as obtained from variable-entropy conditions.

<center>SYMBOLS</center>

A      area

$c_p$      specific heat at constant pressure

d      cylindrical roughness diameter

f      similar stream function, $\dfrac{\partial f}{\partial \eta} = \dfrac{u}{u_e}$

H      total enthalpy

h      static enthalpy

$\bar{h}$      heat-transfer coefficient

j      exponent in equations (A2) and (A3) (j = 0 for yawed infinite cylinder; j = 1 for body of revolution)

k      roughness height

$l$      model axial length

M      Mach number

$N_{St,b}$      Stanton number based on normal-shock entropy, $\left(\dfrac{h}{\rho_e u_e c_{p,e}}\right)_b$

$N_{St,s}$      Stanton number based on sharp-cone fluid properties, $\left(\dfrac{h}{\rho_e u_e c_{p,e}}\right)_s$

$N_{St,v}$      Stanton number based on variable-entropy fluid properties, $\left(\dfrac{h}{\rho_e u_e c_{p,e}}\right)_v$

P      shear parameter, $-\dfrac{dp_e/d\xi}{\beta \dfrac{t_e}{t_s} \rho_e \dfrac{u_e^2}{2\xi}}$

p      pressure

$p_{t,2,\theta}$      total pressure behind oblique shock with slope $\theta$

$p_{t,\infty}$      free-stream total pressure

$p_t'$      total pressure behind normal shock

$q$      heat-transfer rate

$R_b$      unit Reynolds number based on normal-shock entropy, $\left(\dfrac{\rho_e u_e}{\mu_e}\right)_b$

$R_{o,r_n}$      reference Reynolds number, $\dfrac{\rho_o \sqrt{2H_e}\, r_n}{\mu_o}$

$R_s$      unit Reynolds number based on sharp-cone fluid properties, $\left(\dfrac{\rho_e u_e}{\mu_e}\right)_s$

$R_v$      unit Reynolds number using variable-entropy fluid properties, $\left(\dfrac{\rho_e u_e}{\mu_e}\right)_v$

$R_\infty$      unit Reynolds number based on free-stream fluid properties

$r$      radius of body of revolution (see fig. 36)

$r_n$      nose radius

$r_s$      shock cylindrical radius (see fig. 36)

$s$      surface distance from stagnation point or sharp-cone apex

$T$      temperature

$t = \dfrac{h}{H_e}$

$\bar{t}$      time

$u$      velocity along $s$

$v$      velocity along $y$

$w$      circumferential spacing of roughness elements

$x$      axial distance

$y$      coordinate normal to wall

$\alpha$      angle of attack

$\beta$      pressure gradient parameter, $\dfrac{2\xi}{u_e}\dfrac{du_e}{d\xi}\dfrac{t_s}{t_e}$

$\gamma$      ratio of specific heats

$\delta$      physical boundary-layer thickness

$\delta^*$      boundary-layer displacement thickness

$\zeta = \dfrac{H}{H_e}$

$\theta$      shock slope

$\theta_c$      cone half-angle

$\mu$      viscosity coefficient

$\xi, \eta$      similarity variables

$\rho$      density

$\phi = \dfrac{\rho\mu}{\rho_w \mu_w}$

Subscripts:

b      blunt-body constant-entropy conditions

e      conditions at edge of boundary layer

k      roughness element

o      based on stagnation-point pressure and stagnation-point wall temperature

p      paint melting temperature

s      stagnation value

s           sharp cone

t           transition

v           variable entropy

w           wall value

∞           free-stream value

Primed quantities represent differentiation with respect to  $\eta$ .

## MODEL CONSTRUCTION, TESTING TECHNIQUE, AND DATA REDUCTION

The models (fig. 1) were $5^O$ half-angle right circular cones.  Two models were used during the investigation.   One was 0.7240 meter long and was used for most of the tests. The model had interchangeable steel noses with radii of 0 (actually 0.14 mm), 2.54, 6.30, and 12.7 millimeters.   A second model 0.3049 meter long was made since the location of transition sometimes occurred on the steel portion of the nose of the 0.7240-meter model, and as a result of the testing technique (to be described subsequently), the data obtained on the steel nose could not be used.   The nose radius of this latter model was also approximately 0.14 millimeter.

The models were fabricated by casting a thin layer of high-temperature plastic on an aluminum mandrel and grinding the plastic to the desired dimensions.   This method of fabrication was required because of the testing technique used.

Heat-transfer data, from which the transition locations were deduced, were obtained on the model by recording the time and location of the melt line of a fusible paint.   This method consists of coating a model (made from a plastic with a low thermal conductivity) with a material which melts at a known temperature.   (See refs. 23 to 25.)   The painted model was injected into an established flow and the time required for the paint to melt was recorded with a movie camera.   A photograph of the recording camera and injection mechanism with the model in position is shown in figure 2.

With the time and location of the melt line known, it is possible to calculate the heating rate to the model from the solution of the heat-conduction equation for a semi-infinite slab.   It should be noted that the physical and thermal properties of the model material (ref. 26) must be known and that restrictions are placed on the length of the test period for a given model material and material thickness.   The details of this technique with its limitations and possible sources of error can be found in references 23 to 25.

An example of typical paint patterns obtained with the technique is shown in figure 3. In this figure the blunt conical model is viewed through a narrow window in the tunnel wall. Since the window is rectangular in shape, the rear of the cone flanks is obscured from view in the figure. The contrast between the melted paint (dark region) and the unmelted paint (light regions) is good in this photograph; thus the melt line can be accurately located. However, it should be noted that some paints give better contrast than others and some experimentation is required to obtain the best contrast in a given temperature range. Since the paint is available in small increments of melting temperature, changing paint at a given heating level does not present any appreciable problem. The stripe down the model center line in figure 3 represents an unpainted region on the model. It was necessary to paint the model in this manner to reduce the glare from the melted paint. The secondary light region noted in figure 3 is due to the removal of the melted paint by high shear stresses and should be ignored.

The tests were conducted in the Langley Mach 8 variable-density tunnel. This tunnel is of the blowdown type and has an axially symmetric nozzle with contoured walls. There is about a 0.2 Mach number variation with pressure over the Reynolds number range included in these tests. A calibration curve for the tunnel can be found in reference 27. The nominal total temperature for the tunnel ranged from about $740^{\circ}$ K to $840^{\circ}$ K. The lower temperature is associated with the lowest Reynolds number at which tests were conducted and the higher temperature with the highest Reynolds number available with the facility.

## DISCUSSION OF RESULTS

### Heat-Transfer Distribution

Sharp cone.- The data taken with the sharp cone over the test Reynolds number range are presented in figure 4 for the 0.7240-meter model and in figure 5 for the 0.3049-meter model. There were very little laminar data obtained with the 0.7240-meter sharp cone since transition often occurred on the steel nose where data could not be obtained by the technique employed. Figure 4 indicates that some of the data, although it has the correct slope for laminar heating, is about 20 percent high when compared with the theory obtained by the method of reference 28. The complete reason for this effect is not known at the present; however, it has been found that different batches of the plastic material used to construct models can have different material properties. Therefore, the model could have different material properties than the samples tested in reference 26; this difference could result in a consistent error in the heating rate for a given temperature level. From figure 4, it appears that this error in the material properties did not become appreciable until the surface temperatures exceeded $43^{\circ}$ C. In any case, it is felt that if the level of the data is consistently high, it would have no effect on the location of transition which has been taken as the point where the value of the Stanton

number is a minimum. (See fig. 4.) The laminar data taken with the 0.3049-meter model (fig. 5) indicate an increase in heating above the theoretical value near the nose. This increase could be due to several factors which are: induced-pressure effects, wall-curvature effects, inability to identify the initial time with great accuracy, and the assumption that the model is a semi-infinite slab. The first three of these effects have been found to be small. The effect of the last assumption was checked by assuming the model to be a cylinder heated at the surface with a constant heat-transfer coefficient. The results of these calculations are shown in figure 5. For low heating rates the cylindrical assumption resulted in the data agreeing with the laminar theory; this condition is not true for the high heating rates. It has been found that in addition to the nonuniformity of the plastic material from batch to batch, the inert filler used with the plastic carrier can stratify and cause a variation of material properties within a model depending on how the model is positioned during curing. This fact is believed to contribute to the difference between the data and theory shown in figure 5 for the 0.3049-meter model. Since the data appear to approach the laminar curve near the rear of the model, it is believed that the location of the beginning of transition should not be adversely affected by the physical property variation.

The measured turbulent heating rates for both the 0.7240- and the 0.3049-meter models are in fair agreement with the reference temperature method of reference 29 by using the end of transition as the virtual origin of the turbulent flow. The theory of reference 30 predicts turbulent heating rates that are below the present data; however, because of the influence of possible unknown model material on the heating rate (as noted above), it is not possible, with the present data, to make a valid comparison between the two theories and the data. Also, the limited amount of turbulent data probably would preclude making a comparison.

Blunt cone.- Heat-transfer data taken with the blunt models are presented in figure 6. In general, the laminar data appear to fall on a single curve instead of having different levels at the various unit Reynolds numbers as given by the theory of reference 28 when constant entropy along the cone at the edge of the boundary layer is assumed. This aspect of the data is further investigated when variable-entropy conditions outside the boundary layer are considered. The agreement between the laminar data and laminar theory is good at the low unit Reynolds numbers but the data are high compared with the theory for the higher unit Reynolds numbers. The pressure distribution used with the theory was obtained by the method of references 31 and 32. The pressure ratios for the three noses with different bluntness ratios are presented in figure 7.

The data of figure 6 show that no fully developed turbulent flow was obtained on any of the blunt models for the test Reynolds number range. Also, only a small amount of transition data was obtained with the model with the 12.7-millimeter nose radius (fig. 6(c)).

## Effect of Unit Reynolds Number on Location of Transition

The variation of the transition Reynolds number with unit Reynolds number that has previously been found in wind-tunnel tests has been explained in various ways by different investigations. For example, in reference 33 stability theory was used to demonstrate that the transition Reynolds number should increase with unit Reynolds number for the simple case of the boundary layer on a flat plate in subsonic flow. On the other hand, many investigators (for example, ref. 34) indicate that the observed variation of transition Reynolds number in a wind tunnel with unit Reynolds number is associated with the variation of free-stream turbulence level of a facility resulting from noise generated by the turbulent boundary layer on the tunnel wall. Generally, much of the turbulence affecting transition in subsonic or very low supersonic tunnels originates in or upstream of the stagnation chamber. In high supersonic wind tunnels, the turbulence level in the stagnation chamber has relatively little effect on transition in the test section. In high supersonic and hypersonic wind tunnels, a strong generator of stream disturbances is the sound and pressure pulses created by the turbulent boundary layer on the tunnel wall. (See refs. 35 to 37.)

If the location of transition is related to the stability of the boundary-layer flow, the transition Reynolds number on a model will presumably be governed by some relationship determined by the magnitude and frequency of the free-stream and model-surface disturbances and the response (that is, amplification or damping ability) of the boundary-layer flow to these disturbances. There appear to be little data from which details of these effects on transition can be evaluated. The unit Reynolds number effect in this paper is therefore limited to a discussion of observed values and trends without regard to facility turbulence levels and frequencies which are presently unknown.

The present tests were conducted at several local unit Reynolds numbers to investigate the influence of unit Reynolds number on the location of transition under present conditions. Figure 8 is a plot of wetted length to transition ($s_t$) against unit Reynolds number and it can be seen that for all nose radii of the tests, the distance from the nose to the location of transition decreased with increasing unit Reynolds number except for $r_n$ = 2.54 mm. Figure 9 indicates, however, that the transition Reynolds number based on assumed sharp-cone flow properties increases significantly with unit Reynolds number. At a given nose radius, the variation of transition Reynolds number with unit Reynolds number is approximately linear except for the case of $r_n$ = 2.54 mm in the vicinity of the highest unit Reynolds number of the investigation. In figure 9 the magnitude of the transition Reynolds number (based on sharp-cone flow conditions) for the blunt-cone data is larger than that for the sharp cone. However, when variable entropy is taken into account, as will be shown later, the magnitude of the transition Reynolds number is approximately the same, at a given unit Reynolds number, for sharp and blunt cones.

## Effect of Bluntness on the Location of Transition

It is well known that blunting the sharp leading edge of a flat plate or the sharp point of a cone can result in a rearward movement of transition. (See, for example, ref. 38.) The reason given for this rearward movement (ref. 39) is that bluntness reduces the local Reynolds and Mach numbers at the outer edge of the boundary layer. Consequently, if it is assumed that transition occurs at the same local Reynolds number, a larger distance from the leading edge is required with a blunt leading edge to obtain the same local transition Reynolds number than is required with a sharp leading edge.

The present results obtained with the blunted cone are presented in figures 8 and 9 and indicate a substantial rearward movement of the location of transition as bluntness is increased. For a bluntness of 12.7 mm, the location of transition is downstream of the model for all unit Reynolds numbers less than about $1.5 \times 10^7$ per meter.

In reference 1, blunted-cone transition data are correlated as the difference between the sharp- and blunt-cone transition Reynolds numbers as a function of Reynolds number based on nose radius. The present data for a cone and that of reference 1 for a hollow cylinder are plotted in this form in figure 10. Although there is some difference in the absolute level of the present data and that of reference 1 (which represent the end of transition), the general trend of the two sets of data tends to agree. One advantage of this correlation is that the effect of the variation of unit Reynolds number does not appear directly. Because of this effect, one might reason that the effect of changing bluntness on the transition Reynolds numbers obtained in a tunnel may be extrapolated to flight conditions. However, the absolute value of the transition Reynolds number is not known from this type of correlation.

## Effect of Angle of Attack on Location of Transition

Angle of attack would be expected to have an effect on the location of transition since the boundary layer on the most windward ray would be thinned whereas the boundary layer on the most leeward ray would be increased in thickness because of cross-flow effects. Transition data on the most windward and most leeward ray of the cone at an angle of attack of $1^\circ$ are presented in figures 11 and 12. It should be noted that the data have been reduced by using the local condition obtained from the tangent-cone method for the most windward and leeward rays. The general variation of the transition Reynolds number with unit Reynolds number and bluntness is the same as that found for zero angle of attack. The level of the transition Reynolds number tends to increase for the windward ray and decrease for the leeward ray (figs. 12(a) and 12(b)) when compared with the zero-angle-of-attack data (fig. 9). The distance from the stagnation point to the location of transition on the windward ray is presented in figure 11(a) and both the 2.54 mm and 6.35 mm radius

nose models indicate a rearward movement of transition with increasing unit Reynolds number for the highest unit Reynolds number.

The transition Reynolds numbers for various unit Reynolds numbers for the sharp cone at higher angles of attack are presented in figure 13. A summary plot for the distance to transition on the most windward and most leeward rays as a function of angle of attack for the sharp cone at various unit Reynolds numbers is shown in figure 14. In general, increasing angle of attack moves the transition location rearward on the most windward ray and forward on the most leeward ray except for $\alpha > 2.50$. The variation of transition location with angle of attack is greatest at the low unit Reynolds numbers except possibly for large angle of attack on the most leeward ray.

### Effect of Roughness on Location of Transition

Spherical roughness elements.- Most of the roughness tests used spherical roughness elements as the tripping device. Two nose bluntnesses $\left(r_n = 2.54 \text{ mm and } 6.35 \text{ mm}\right)$ were tested with spherical roughness elements of various diameters located at various distances along the cone. A table representing the six geometrical configurations employed during the tests follows:

| $r_n$, mm | $k$, mm | $x_k$, mm | $w$, mm | $w/k$ | Number of spheres |
|---|---|---|---|---|---|
| 2.54 | 1.19 | 31.1 | 3.17 | 2.667 | 10 |
| 2.54 | 1.19 | 50.2 | 3.25 | 2.730 | 13 |
| 2.54 | 1.59 | 50.1 | 4.22 | 2.656 | 10 |
| 6.35 | 1.19 | 78.6 | 3.47 | 2.918 | 23 |
| 6.35 | 2.38 | 78.1 | 6.62 | 2.783 | 12 |
| 6.35 | 3.18 | 77.7 | 8.81 | 2.776 | 9 |

A photograph of the six nose pieces with the spherical roughness elements included is shown in figure 15.

Schlieren pictures were taken to obtain the shock pattern from the roughness element. These results are shown in figure 16 and reveal that shocks are produced by all the roughness elements tested and for all unit Reynolds numbers. These secondary shocks in the inviscid flow field would presumably affect the fluid properties at the edge of the boundary layer and would therefore have to be accounted for in any analysis of the turbulent boundary layer. For gross effects of the turbulent boundary layer on quantities such as lift, drag, and control effectiveness, the influence of these shocks on the fluid properties at the edge of the boundary may or may not be significant, depending upon the aims of the tests.

The location of transition as a function of unit Reynolds number is presented in figure 17 for the tests conducted with spherical roughness elements. From the figure it can be seen that for low unit Reynolds numbers and small roughnesses there is little or no influence of roughness on the location of transition when compared with the smooth data. As the unit Reynolds number is increased for the small roughness elements, there is a narrow range of Reynolds number over which there is a rapid forward movement of the location of transition followed by little further change in the location of transition. The Reynolds number where the forward movement of transition essentially ends is defined as the Reynolds number where the trip becomes effective. (See, for example, fig. 17(a).)

As noted above, increasing the unit Reynolds number above the so-called effective value had little effect on the forward movement of transition; however, at large unit Reynolds numbers above the effective value, streaks were observed in the paint patterns downstream of the roughness elements. An example of these streaks is shown in figure 18. These streaks indicate that there is a circumferential heat-transfer distribution around the model for high unit Reynolds numbers. These streaks persist to the end of the model well into the region where the boundary layer is turbulent. From these results it appears that roughness elements somewhat greater than the effective values result in nonuniform flow distributions that would make it difficult to obtain useful turbulent-flow data downstream of roughness elements. It should be noted that similar disturbances have been observed by Van Driest and McCauley during their oil-flow studies (ref. 13).

These nonuniform circumferential heat-transfer distributions are discussed in more detail later, but first consider these data plotted in the more conventional manner of $s_t/r_n$ as a function of $k/\delta_k^*$ as presented in figure 19, where $\delta_k^*$ is computed by conventional constant-entropy blunt-body methods. From figure 19, it can be seen that the effective value for $k/\delta_k^*$ ranges from 1.7 to 2.2 depending somewhat on nose radius or $x_k$ or both. The effective values of $k/\delta_k^*$ are in agreement with the values obtained in reference 7 for a sharp cone. The effective values of $k/\delta_k^*$ for the blunt cones in reference 7 are many times the values of the present investigation. This difference is probably due to the difference in the location of the roughness elements for the two investigations. In reference 7 the elements were on the spherical portion of the body; in the present investigation they were well downstream of the nose.

Also noted in figure 19 are the values of $k/\delta_k^*$ where the nonuniform circumferential heat-transfer distribution appeared in the turbulent flow region for the length of the model aft of the roughness elements. The values of $k/\delta_k^*$ where the nonuniformities first appeared were about 2.7 to 3.5 depending on nose radius or $x_k$ or both and are not much larger than the effective values of $k/\delta_k^*$. Therefore, once the effective value of $k/\delta_k^*$ has been obtained for these test conditions, it appears that $\delta_k^*$ cannot be reduced significantly without introducing nonuniformities in the heat transfer for large downstream distances into the turbulent boundary-layer region.

12

Heat-transfer rates were obtained for the high and low heating rate striae and an example of the results is shown in figure 20. The heating rates in the low heating region tended to agree with the turbulent theory of reference 29 when the virtual origin of the turbulent flow was assumed to be located at the roughness elements. The high heating rates were well above the theory and exceeded the rates in the low regions by about 30 to 45 percent. As pointed out previously, the theory of reference 30 is low when compared with the present data.

In general, the ratio of peak to valley heating rates around the model for various tests ranged from 1.13 to 2.38, most of the data being in the 1.40 range. This perturbation is significant and indicates that roughness elements larger than the effective size should be used with caution when tripping the laminar boundary for basic turbulent boundary-layer investigations. It should be noted that the nonuniform circumferential heating distribution develops gradually. At low values of $k/\delta_k^*$ there is no sign of this type of distribution except near the roughness element. However, as $k/\delta_k^*$ is increased, this distribution extends into the laminar and transitional flow region but cannot be discerned in the turbulent region. With a further increase in $k/\delta_k^*$, the distribution was present in the turbulent flow region for the entire length of the present model.

Closeup photographs of the paint patterns immediately behind the roughness elements were made for three unit Reynolds numbers. Typical results at one Reynolds number are presented in figure 21. The light areas in the photographs initially indicate unmelted paint and the dark regions indicate melted paint. After the paint melts, it is often locally removed from the model by high shearing stress. This removal of the paint can cause this area of the model to appear light in the photographs if the light is reflected from this surface into the camera. This reflection causes the secondary light regions which appear in the photographs in figure 21.

From the photograph it can be seen that the highest heating rates are behind the roughness elements on either side of the element center line (that is, where the paint melts first). The lowest heating rates exist in the region between and downstream of the roughness elements. The necking in and subsequent flaring out of the melted regions, seen between 1.6 and 4.5 seconds in figure 21, indicate that there probably is some mutual interference between the flow fields produced by the roughness elements. Contours of constant heating rates were plotted for the region immediately downstream of the roughness element and are presented in figure 22. These contours show that the lowest heating rate exists as a small island between and just downstream of the roughness element.

Various roughness shapes and configurations.- Because of the disturbances caused by spherical roughness elements, a preliminary investigation was made to determine whether an effective type of roughness could be found that would not produce significant

disturbances in the turbulent boundary layer. The types of roughness configurations tested are pictured in figure 23 and include double rows of spheres, cylinders perpendicular to the surface, screw threads, an annular groove, and two-dimensional wire. It should be noted that for the screw threads and annular groove, k is the depth of the threads or groove and $x_k$ is measured to the beginning of the threads or groove.

Transition data obtained with these roughnesses are presented in figure 24, and all the roughness data are summarized in figure 25 in the form of transition location as a function of $k/\delta_k^*$. In general, the double row of spheres and cylinders perpendicular to the surface is as effective as a single row of spheres in tripping the laminar boundary; however, the nonuniform heating rate is of the same order as those generated by the single row of spheres. The two-dimensional wire is somewhat less effective than the row of spheres but produced no nonuniform circumferential heating distribution around the model. The shocks formed by a two-dimensional wire, however, would probably influence a larger volume of the cone inviscid flow field than single roughness elements, and would therefore increase the region downstream of the element influenced by variable-entropy conditions. The annular groove and screw threads were completely ineffective over the unit Reynolds number range of the tests.

### Effect of Variable Entropy at Edge of Boundary Layer

In the previous discussion it has been tacitly assumed that the conditions outside the boundary layer can be obtained for a blunt body by expanding the gas isentropically from the stagnation point to the local pressure on the body. For a model with small bluntness compared with the body length, the external conditions cannot be calculated correctly by this method because of the curvature of the bow shock and the gradual engulfment into the boundary layer of the high entropy air associated with the normal portion of the bow shock which leaves lower entropy air external to the boundary layer. This effect has been considered by several investigators and solutions, with various degrees of approximations, have been obtained. See, for example, references 16 to 21. Another method for partly accounting for variable-entropy effects on the laminar boundary layer is presented in the appendix and in reference 40. Unfortunately, the calculations presented in reference 40 were subsequently found to be in error. The error was made in computing the shear parameter P, which should have been variable; however, the results in reference 40 are essentially the same as if P was taken to be 1 – the usual procedure used by other investigators in references 16 to 21. Subsequent calculations using the correct values of P resulted in extremely slow convergence of the solutions to acceptable values of $f_w''$ and $\zeta_w'$. This condition is true although the convergence criteria for $f_w''$ and $\zeta_w'$ were relaxed from 0.1 percent to 0.2 percent. An example of the difference between the results for P = 1 and variable P is shown in figure 26 for one value of $R_{0,r_n}$. It can be seen from the figure that although there is

14

some difference in the edge conditions computed by the two methods (a difference of at most about 1 in Mach number and a factor of 2 in Reynolds number), the experimental data to be presented herein are reduced by the conventional solution for $P = 1$ because of the large increase in machine time required to obtain the solutions for variable $P$ and because of approximations inherent in both methods. As more data become available to describe the influence of most of the important factors controlling transition and as this information is incorporated into boundary-layer correlation parameters, it may become necessary to improve boundary-layer calculations to include the value of variable $P$ and $\left(\frac{\partial u}{\partial y}\right)_e \neq 0$ when computing the boundary edge conditions.

Some general results obtained with the method of the appendix for $P = 1$ are presented in figures 27 to 29. The shock shape and body pressure distribution required for the calculation were obtained by the method of references 31 and 32. There is a significant variation of these parameters from those obtained by the blunt-body constant-entropy method depending on the reference Reynolds number and $s/r_n$. For $s/r_n$ values less than about 10, the blunt-body method should give good results at all reference Reynolds numbers of interest for the present experimental investigation $\left(10^4 < R_{o,r_n} < 10^7\right)$. For small values of $R_{o,r_n}$ in this range $\left(10^4 < R_{o,r_n} < 10^7\right)$, there is a significant difference between the constant- and variable-entropy methods when $s/r_n$ is greater than 10. Figure 28 presents the Reynolds number at the edge of the boundary layer for several values of $R_{o,r_n}$. Figure 29 compares the values of local Reynolds number based on variable-entropy conditions with Reynolds number based on normal-shock entropy at $R_{o,r_n} = 10^5$. For $s/r_n \gtrsim 200$ the variable-entropy Reynolds number is about 10 times larger than the Reynolds number for normal-shock entropy.

Figure 30 presents laminar boundary-layer velocity and enthalpy profiles for three values of $s/r_n$ and three values of $R_{o,r_n}$. If one notes the $R_{o,r_n} = 10^6$ case, it can be seen how the velocity and enthalpy profiles develop from the blunt-body, constant-entropy case near the nose to the sharp cone value at large values of $s/r_n$. For certain values of $R_{o,r_n}$ and $s/r_n$, the local values of the velocity ratio can exceed the sharp-cone values whereas the local values of the enthalpy ratio will be less than the sharp-cone values. This situation develops before the profiles ultimately approach sharp-cone values.

The velocity and enthalpy gradient in the transformed $\eta$ plane at the wall does not appear to vary greatly for the conditions considered. It is interesting to note that transforming the enthalpy gradient at the wall to the physical plane gives values of the heating rate that are little affected by variable-entropy effects (see fig. 31) for the present free-stream and wall conditions. This result is contrary to the results found by other investigators (ref. 20) who found that variable-entropy effects resulted in an increase in the heat-transfer rate. This disagreement on the effect of variable entropy

may be due to the differences in the free-stream and wall conditions considered herein and in reference 20 which were, in general, for higher Mach number and lower ratios of wall temperature to total temperature than those of the present investigation.

In order to investigate the reason for the similarity between the gradient at the wall in the transformed and physical plane for both the blunt-body and variable-entropy conditions, the ratio of the heating rate for the variable-entropy and constant-entropy conditions was formed. In terms of the transformation variables in the appendix, this ratio is

$$\frac{q_v}{q_b} = \frac{\zeta'_{w,v}}{\zeta'_{w,b}} \frac{\dfrac{\sqrt{\left[\displaystyle\int_0^{s/r_n} \left(\frac{\rho_w \mu_w}{\rho_0 \mu_0}\right) \frac{u_e}{\sqrt{2H_e}} \left(\frac{r}{r_n}\right)^{2j} \frac{ds}{r_n}\right]_b}}{\left(\dfrac{u_e}{\sqrt{2H_e}}\right)_b}}{\dfrac{\sqrt{\left[\displaystyle\int_0^{s/r_n} \left(\frac{\rho_w \mu_w}{\rho_0 \mu_0}\right) \frac{u_e}{\sqrt{2H_e}} \left(\frac{r}{r_n}\right)^{2j} \frac{ds}{r_n}\right]_v}}{\left(\dfrac{u_e}{\sqrt{2H_e}}\right)_v}} \tag{1}$$

The ratio of the enthalpy gradient at the wall in the transformed plane $\zeta'_{w,v}/\zeta'_{w,b}$ is less than but nearly equal to 1 for the case considered. Also, for the variable-entropy case, the larger value of the integral is divided by the larger velocity; therefore the value of the second ratio in equation (1) is greater than but almost equal to 1. The combination of the two ratios for the present conditions results in a value for the heating-rate ratio that is very nearly 1.

The heat-transfer data for the blunt cones are presented in the form of the variation of $N_{St,v}$ with $R_{v,s}$ in figure 32 where variable-entropy conditions outside the boundary layer are accounted for. Theoretical results for the different unit Reynolds numbers for this method group close together as was observed for the data when reduced by the blunt-body constant-entropy method (fig. 6). The theory and data are in good agreement for the $r_n = 2.54$ mm model. For the other models, the agreement near the nose for some unit Reynolds numbers is not too good, but the laminar data, in general, approach the laminar-theory curve at large distances from the nose. From these data it appears that good agreement between theory and data for slender blunt-nosed bodies, in terms of Stanton number as a function of Reynolds number, can be obtained when both the theory and data-reduction techniques include the effects of variable-entropy conditions at the edge of the boundary layer. On the other hand, direct comparison of the heat-transfer rate, as in figure 31, would evidently give good agreement between the variable- and constant-entropy methods for conditions near those reported herein.

16

The transition data are presented in figure 33 as local transition Reynolds number as a function of local unit Reynolds number with variable-entropy conditions accounted for according to the method of the appendix. Although there is some scatter, the data appear to correlate reasonably well for both the sharp and blunt models. It should be noted that there is about a factor of 2 variation in local Mach number for these data; this variation indicates that transition Reynolds number for tests in a given constant Mach number wind tunnel may not be a significant function of local Mach number for a cone provided local conditions exterior to the boundary layer and the distance to the beginning of transition are used.

Some very preliminary evidence of this effect was given for cones in reference 40 where the local Mach number was varied by changing the cone angle. Since the ratio of $R_s/R_\infty$ is a double-valued function of $\theta_c$, a pair of cones can be found such that the only variable which changes, if the models are tested at a given free-stream unit Reynolds number, is the strength of the shock generated by the cones. Temperature-sensitive-paint data taken with such a pair of cones were presented in reference 40 and the data appeared to correlate somewhat independent of the local Mach number; however, the Mach number range was very restricted. When these data were extended to a somewhat wider range of Mach numbers, it was found that the invariance of the transition Reynolds number with Mach number held only for the high unit Reynolds number as shown in figure 34. Although there is some scatter in the data, this scatter is relatively small compared with the usual trends of transition Reynolds number as a function of Mach number in this Mach number range. For example, the variation of the transition Reynolds number over the present Mach number range has been shown to be a factor of 2 or 3 in reference 6.

It is interesting to note that recent wind-tunnel results described in reference 9 indicate that transition data for flat plate and hollow cylinders can be correlated by using parameters asssociated with the generation of aerodynamic noise in a turbulent boundary layer on the tunnel wall (that is, displacement thickness and skin friction), and the tunnel test-section circumference. This finding might explain the previously noted invariance of transition Reynolds number with Mach number when the tests are conducted in a given tunnel. Also, if the correlations of reference 9 are shown to be universally true, the attempt to correlate transition data with Mach number from different tunnels would be invalid unless the aerodynamic noise intensity parameter (whatever it might be) for the various tunnels is properly accounted for. Although noise intensity parameters were used to correlate transition data in reference 9, it appears, at least from linear stability theory, that frequency or frequency spectrum of the noise might also be important in attempts to correlate wind-tunnel transition data.

17

# CONCLUSIONS

From tests conducted with a 5° half-angle cone in a conventional blowdown tunnel with a free-stream Mach number of 8 over a local (sharp cone) unit Reynolds number range from about $4.5 \times 10^6$ to $4.5 \times 10^7$ per meter ($1.3 \times 10^6$ to $1.3 \times 10^7$ per foot), the following conclusions can be stated: The conclusions for the transition data are presented without quantitative consideration of the disturbance present in the tunnel test section.

1. Increasing the unit Reynolds number at zero angle of attack tends to increase the transition Reynolds number and, in general, to decrease the distance from the cone tip or stagnation point to the location of the beginning of transition.

2. In general, the effect of increasing nose bluntness increased the distance from the stagnation point to the location of transition for the range of bluntness investigated.

3. In general, small increases in the angle of attack increased the transition Reynolds number on the windward ray and reduced the transition Reynolds number on the leeward ray.

4. The laminar boundary layer can be tripped to produce turbulent flow on a blunt-conical model and the values of the ratio of roughness height to boundary-layer displacement thickness $k/\delta_k^*$ required to accomplish this effect range from 1.7 to 2.2 when the roughness is located well downstream from the spherical nose.

5. If the roughness height is somewhat greater $\left(k/\delta_k^* = 2.7 \text{ to } 3.5\right)$ than the effective value required to bring transition approximately up to the roughness element, a nonuniform circumferential heat-transfer rate is produced on the model downstream of the roughness element in the turbulent boundary-layer region for the length of the present model.

6. For a blunt cone, variable-entropy effects were found to have a significant effect on the Mach number and Reynolds number at the edge of the boundary layer depending on distance from the stagnation point and the reference Reynolds number.

7. Transition Reynolds number data, for both the sharp and blunt cones, based on the variable-entropy conditions at the edge of the boundary layer appeared to correlate reasonably well with unit Reynolds number independent of local Mach number which varied from about 3.5 to 7.

8. Experimental laminar heat-transfer data (in terms of the variation of Stanton number with Reynolds number) were in better agreement with theory when variable entropy was included in both data and theory.

Langley Research Center,
National Aeronautics and Space Administration,
Langley Station, Hampton, Va., August 1, 1968,
129-01-08-38-23.

# APPENDIX

# EFFECT OF VARIABLE ENTROPY AT OUTER EDGE OF

# BOUNDARY LAYER ON CHARACTERISTICS OF A

# LAMINAR BOUNDARY LAYER

By P. Calvin Stainback and Kathleen C. Wicker
Langley Research Center

In the present method, the boundary-layer equations of reference 26 are modified to account for variable-entropy effects resulting from curved bow shocks. The equations are solved numerically and an iteration procedure is used to determine the external flow conditions. In the iteration procedure the mass flow in the boundary layer at a given station, obtained by conventional constant-entropy blunt-body methods (see ref. 28) as the first iteration, is equated to the free-stream mass flow through the bow shock. This mass-flow balance plus the shock shape makes it possible to locate the streamline at the shock that is just entering the boundary layer at the selected station. Since the shock shape is assumed to be known, the total pressure behind the shock on the streamline can be calculated. The gas with this total pressure is expanded isentropically to the static pressure at the selected station. These calculations give new values for conditions exterior to the boundary layer for the second iteration. The boundary-layer equations are solved again with the new exterior conditions and a second mass flow balance is made. This procedure is continued until convergence in external flow conditions is obtained. In accordance with the usual boundary-layer assumptions, the pressure is assumed to be independent of $y$ and equal to the surface distribution which is held constant throughout the iteration procedure.

The major difference between the present method and that of reference 18 is the boundary-layer equations used. In reference 20, conventional similar boundary-layer equations were used where it was assumed that Bernoulli's equation applies outside the boundary layer. If the entropy varies along the edge of the boundary layer, this assumption is not correct. Also, considerable difficulty is encountered in specifying the boundary conditions at the outer edge of the boundary layer. This problem has been considered in some detail in reference 41. In the present method Bernoulli's equation is not used; however, the gradient in the fluid properties with respect to distance perpendicular to the surface is assumed to be small at the outer edge of the boundary layer in order to obtain an asymptotic solution at large distances from the wall.

With these assumptions, only the momentum equation requires alteration from its usual form. The momentum equation is:

# APPENDIX

$$\rho u \frac{\partial u}{\partial s} + \rho v \frac{\partial u}{\partial y} = -\frac{dp}{ds} + \frac{\partial}{\partial y}\left(\mu \frac{\partial u}{\partial y}\right) \tag{A1}$$

and the equations for the similarity variables (ref. 28) can be put into the following form:

$$\xi = R_{o,r_n} \int_0^{s/r_n} \frac{\rho_w \mu_w}{\rho_o \mu_o} \frac{u_e}{\sqrt{2H_e}} \left(\frac{r}{r_n}\right)^{2j} \frac{ds}{r_n} \tag{A2}$$

$$\eta = R_{o,r_n} \frac{\frac{u_e}{\sqrt{2H_e}}}{\sqrt{2\xi}} \left(\frac{r}{r_n}\right)^j \int_0^{y/r_n} \frac{\rho}{\rho_o} \frac{dy}{r_n} \tag{A3}$$

where $u_e$ is the local value of the velocity at $y = \delta$. Thus, if $\delta$ is considered as a predetermined fixed value of $y$ (where viscous shear becomes negligible), $u_e$ and $\xi$ are functions only of $x$ for a given iteration.

With these assumptions, the momentum equation becomes

$$(\phi f'')' = -ff'' - \beta \frac{t_e}{t_s}\left(P \frac{\rho_e}{\rho} - f'^2\right) + 2\xi\left(f' \frac{\partial^2 f}{\partial \xi \partial \eta} - f'' \frac{\partial f}{\partial \xi}\right) \tag{A4}$$

where $P$ can be expressed as

$$P = -\frac{dp_e/d\xi}{\beta \left(\frac{t_e}{t_s}\right)\frac{\rho_e u_e^2}{2\xi}} \tag{A5}$$

or in a more convenient form for computing

$$P = \frac{\left[\frac{\rho_e}{\rho_o} \frac{u_e}{\sqrt{2H_e}} \frac{d}{d\frac{s}{r_n}}\left(\frac{u_e}{\sqrt{2H_e}}\right)\right]_{\text{1st iteration}}}{\left[\frac{\rho_e}{\rho_o} \frac{u_e}{\sqrt{2H_e}} \frac{d}{d\frac{s}{r_n}}\left(\frac{u_e}{\sqrt{2H_e}}\right)\right]} \tag{A6}$$

These equations, without the nonsimilar terms ($\partial/\partial\xi$ terms), plus the energy equation have been solved numerically, the local edge conditions being calculated by the iterative procedure.

It should be noted that in the derivation of these boundary-layer equations, certain inconsistent assumptions were made. It was assumed that $\left(\frac{\partial u}{\partial y}\right)_e$ is small in order to obtain an asymptotic solution to the boundary-layer equations at large values of $\eta$. This assumption and the momentum equation lead to the following result:

$$\frac{dp}{dx} = -\rho_e u_e \frac{\partial u_e}{\partial x} \tag{A7}$$

that is, Bernoulli's equation. However, as pointed out, it has been further assumed that Bernoulli's equation does not apply at the edge of the boundary layer. These two assumptions are, therefore, incompatible. Also, it is not entirely clear that the restrictions on $u_e$ in the transformation equations (A2) and (A3) are strictly valid. That is, should $\left(\frac{\partial \xi}{\partial y}\right)_s$ and $\left(\frac{\partial \eta}{\partial y}\right)_s$ include the variation of $\left(\frac{\partial u}{\partial y}\right)_e$? Although these equations do contain inconsistencies, they are believed to represent a reasonable approximation to a more exact system.

The external conditions for successive iterations can be obtained by equating the mass flow in the boundary layer to that through the shock. This mass balance gives

$$\rho_\infty u_\infty \int_0^{r_s} dA = \int_w^e \rho u \, dA \tag{A8}$$

From the geometry shown in figure 35 and the transformation equations (A2) and (A3), the following expression for the shock radius is obtained:

$$\left(\frac{r_s}{r_n}\right)^2 = \frac{2\sqrt{2\xi}}{R_{0,r_n}} \frac{\sqrt{2H_e}}{u_\infty} \frac{\rho_0}{\rho_\infty}(f_e - f_w) \tag{A9}$$

where for zero mass flow through the wall, $f_w = 0$. Since $f_e$ strongly influences the value of $r_s/r_n$ in equation (A9) and $f_e$ is a function of $\eta_e$, the method for determining $\eta_e$ can have a significant effect on the results. In the present method $\eta_e$ is obtained as follows: Values for $f_w''$ and $\zeta_w'$ are estimated and the boundary-layer equations integrated to a given value of $\eta = \eta_1$ where $\eta_1$ is less than the final value of $\eta_e$. The boundary conditions at $\eta_1$ on $f'$ and $\zeta$ are assumed to be $1.0000 \pm 0.0005$ which are obtained by standard procedures. (See ref. 42.) Primarily to determine whether this solution is the correct asymptotic solution, a second value of $\eta = \eta_2$ is chosen, where $\eta_2 > \eta_1$, and a second solution is obtained. The values of both $\zeta_w'$ and $f_w''$ from the first and second solutions are compared; if the difference is greater than 0.1 percent, another value of $\eta > \eta_2$ is chosen and a third solution is obtained. This method is continued until the difference in $f_w''$ and $\zeta_w'$ from successive solutions is less than 0.1 percent. In the present solutions the value of $\eta_{i+1} - \eta_i = 0.1$ was used. The value of $\eta$ at the edge of the boundary layer required to obtain this convergence in $f_w''$ and $\zeta_w'$ is then denoted as $\eta_e$, and the corresponding value of $f_e$ is used in equation (A9).

Since the shock shape is assumed to be known,

$$\theta = f_1\left(\frac{r_s}{r_n}\right) \tag{A10}$$

Therefore, the total pressure behind the shock can be obtained as

$$\frac{p_{t,2\theta}}{p_{t,\infty}} = f_2\left(\frac{r_s}{r_n}\right) \tag{A11}$$

21

# APPENDIX

Since the expansion from $p_{t,2\theta}$ to $p_w$ is along a streamline, it is isentropic; thus, the velocity outside the boundary layer, for an ideal gas, can be expressed as

$$\frac{u_e}{\sqrt{2H_e}} = \left[1 - \left(\frac{p_w}{p_{t,2\theta}}\right)^{\frac{\gamma-1}{\gamma}}\right]^{1/2} \tag{A12}$$

or

$$\frac{u_e}{\sqrt{2H_e}} = \left[1 - \left(\frac{p_w}{p_t'}\right)^{\frac{\gamma-1}{\gamma}}\left(\frac{p_t'}{p_{t,\infty}}\right)^{\frac{\gamma-1}{\gamma}}\left(\frac{p_{t,\infty}}{p_{t,2\theta}}\right)^{\frac{\gamma-1}{\gamma}}\right]^{1/2} \tag{A13}$$

Other flow properties then follow from the relations:

$$t_e = 1 - \left(\frac{u_e}{\sqrt{2H_e}}\right)^2 \tag{A14}$$

$$M_e = \sqrt{\frac{2}{\gamma-1}} \frac{\frac{u_e}{\sqrt{2H_e}}}{\sqrt{t_e}} \tag{A15}$$

$$\frac{\rho_e}{\rho_o} = \left(\frac{p_w}{p_t'}\right)\frac{t_{w,s=0}}{t_e} \tag{A16}$$

These equations and the boundary-layer energy equation, together with the shock shape and the pressure distribution for the body, provide all the information needed to determine the local external-flow conditions.

The external velocity $u_e$ was used to establish a convergence criterion for these equations. If $P = 1$, convergence of the equations was very rapid. If $P$ is a variable, convergence of these equations is very slow. In fact, several iterations (up to 6) are required to obtain a solution to the accuracy described. Even though the convergence requirements for $f_w''$ and $\zeta_w'$ are relaxed to 0.2 percent, several iterations are still required. Because of this increase in machine time and the inherent limitations in the method due to the boundary-layer assumptions, it is felt that the $P = 1$ solutions are sufficiently accurate for boundary-layer transition correlation studies at the present time. (See fig. 26.) As transition data correlations become more accurate and complete, it might be necessary to use variable values of $P$ and take into account the fact that $\left(\frac{\partial u}{\partial y}\right)_e \neq 0$ in obtaining solutions for the viscous layer.

It should be noted that the solutions to the boundary-layer equations with variable $P$ uncouple the velocity gradient from the pressure gradient. Whereas Bernoulli's equation states that an increasing velocity requires a decreasing pressure, this is not true for the

22

variable-entropy method. For example, in the present variable $P$ solutions, it is common to have both the velocity at the edge of the boundary layer and pressure increasing with distance along a body. If $P$ is forced to be 1, the asymptotic solution to the boundary-layer equations is obtained for a body with a fictitious pressure distribution as noted in reference 16. However, the pressure distribution obtained from the inviscid flow program is used to compute the velocities at the edge of the boundary. Therefore, the $P = 1$ solution contains an additional inconsistency; that is, the pressure distribution on the body used in the solution of the boundary-layer equation is different from the one used to obtain flow conditions at the edge of the boundary layer.

The case for variable $P$ where the velocity at the edge of the boundary layer and the surface pressure can vary independently of each other leads to interesting speculations as to the effect of variable entropy on boundary-layer characteristics such as transition and separation. An increase in pressure with distance usually promotes transition and separation; however, when the velocity at the edge of the boundary layer also increases with distance, it might be possible to add enough momentum to the boundary-layer flow to counteract or reduce the effect of the increase in pressure.

## REFERENCES

1. Potter, J. Leith; and Whitfield, Jack D.: Effects of Slight Nose Bluntness and Rough-
ness in Boundary-Layer Transition in Supersonic Flows. J. Fluid Mech., vol. 12,
pt. 4, Apr. 1962, pp. 501-535.

2. Potter, J. Leith; and Whitfield, Jack D.: Boundary-Layer Transition Under Hyper-
sonic Conditions. Recent Developments in Boundary Layer Research, Pt. III,
AGARDograph 97, May 1965, pp. 1-62.

3. Palko, R. L.; Burt, R. H.; and Ray, A. D.: An Experimental Investigation of
Boundary-Layer Transition on Flat Plates at Mach Numbers 5, 8, and 10.
AEDC-TDR-64-167, U.S. Air Force, Aug. 1964.

4. Deem, Ralph E.; and Murphy, James S.: Flat Plate Boundary Layer Transition at
Hypersonic Speeds. AIAA Paper No. 65-128, Jan. 1965.

5. Nagamatsu, H. T.; Graber, B. C.; and Sheer, R. E., Jr.: Combined Effects of Rough-
ness, Bluntness, and Angle of Attack on Hypersonic Boundary Layer Transition.
$M_1 \approx 8.5$ to 10.5. Tech. Inform. Ser. No. 65-C-011, Res. Develop. Center, Gen.
Elec. Co., Sept. 1965.

6. Nagamatsu, H. T.; Graber, B. C.; and Sheer, R. E., Jr.: Hypersonic Laminar Bound-
ary Layer Transition on 8-Foot Long $10^{\circ}$ Cone. Rept. No. BSD-TR-65-471, Gen.
Elec. Co., Dec. 1965.

7. McCauley, W. D.; Saydah, A.; and Bueche, J.: The Effect of Controlled Three Dimen-
sional Roughness on Hypersonic Laminar Boundary Layer Transition. AIAA Paper
No. 66-26, Jan. 1966.

8. Stetson, Kenneth F.; and Rushton, George H.: A Shock Tunnel Investigation of the
Effects of Nose Bluntness, Angle of Attack and Boundary Layer Cooling on Bound-
ary Layer Transition at a Mach Number of 5.5. AIAA Paper No. 66-495, June 1966.

9. Pate, S. R.; and Schueler, C. J.: The Influence of Radiated Aerodynamic Noise on
Model Boundary-Layer Transition in Supersonic and Hypersonic Wind Tunnels.
Boundary Layer Transition Study Group Meeting, Vol. III, William D. McCauley,
ed., BSD-TR-67-213, Vol. III, U.S. Air Force, Aug. 1967, pp. 21-1 − 21-40.

10. Larson, Howard K.; and Mateer, George G.: Transition Measurements on Cones in
Hypersonic Flow and Preliminary Observations of Surface Ablation Grooves.
Boundary Layer Transition Study Group Meeting, Vol. III, William D. McCauley,
ed., BSD-TR-67-213, Vol. III, U.S. Air Force, Aug. 1967, pp. 17-1 − 17-30.

11. Potter, J. Leith:  The Influence of Ambient Pressure on Boundary-Layer Transition in an Aeroballistic Range.  Boundary Layer Transition Study Group Meeting, Vol. III, William D. McCauley, ed., BSD-TR-67-213, Vol. III, U.S. Air Force, Aug. 1967, pp. 20-1 — 20-16.

12. Schlichting, Hermann:  Boundary Layer Theory.  McGraw-Hill Book Co., Inc., 1955, pp. 553-556.

13. Van Driest, E. R.; and McCauley, W. D.:  The Effect of Controlled Three-Dimensional Roughness on Boundary-Layer Transition at Supersonic Speeds.  J. Aero/Space Sci., vol. 27, no. 4, Apr. 1960, pp. 261-271, 303.

14. Klebanoff, P. S.; and Diehl, Z. W.:  Some Features of Artificially Thickened Fully Developed Turbulent Boundary Layers With Zero Pressure Gradient.  NACA Rep. 1110, 1952.  (Supersedes NACA TN 2475.)

15. Holloway, Paul F.; and Sterrett, James R.:  Effect of Controlled Surface Roughness on Boundary-Layer Transition and Heat Transfer at Mach Numbers of 4.8 and 6.0. NASA TN D-2054, 1964.

16. Ferri, Antonio:  Some Heat Transfer Problems in Hypersonic Flow.  Aeronautics and Astronautics, Nicholas John Hopp and Walter Guido Vincenti, eds., Pergamon Press, Inc., 1960, pp. 344-377.

17. Rubin, Irving:  Shock Curvature Effect on the Outer Edge Conditions of a Laminar Boundary Layer.  AIAA J., vol. 1, no. 12, Dec. 1963, pp. 2850-2852.

18. Ferri, Antonio; and Libby, Paul A.:  Note on an Interaction Between the Boundary Layer and the Inviscid Flow.  J. Aeron. Sci. (Readers' Forum), vol. 21, no. 2, Feb. 1954, p. 130.

19. Wilson, R. E.:  Laminar Boundary-Layer Growth on Slightly Blunted Cones at Hypersonic Speeds.  J. Spacecraft and Rockets, vol. 2, no. 4, July-Aug. 1965, pp. 490-496.

20. Zakkay, Victor; and Krause, Egon:  Boundary Conditions at the Outer Edge of the Boundary Layer on Blunted Conical Bodies.  ARL-62-386 (Contract AF 33(616)-7661), U.S. Air Force, July 1962.

21. Schmidt, H.; and Van Tassell, W.:  Aerodynamic Effects of Blunting on Conical Bodies. Tech. Memo RAD-TM-62-110 (Contract AF 04(694)-264), U.S. Air Force, Feb. 15, 1963.

22. Sheetz, Norman W., Jr.:  Free-Flight Boundary Layer Transition Investigations at Hypersonic Speeds.  AIAA Paper No. 65-127, Am. Inst. Aeron. Astronaut., Jan. 1965.

23. Jones, Robert A.; and Hunt, James L.: Use of Fusible Temperature Indicators for Obtaining Quantitative Aerodynamic Heat-Transfer Data. NASA TR R-230, 1966.

24. Jones, Robert A.; and Hunt, James L.: Use of Temperature-Sensitive Coatings for Obtaining Quantitative Aerodynamic Heat-Transfer Data. AIAA J., vol. 2, no. 7, July 1964, pp. 1354-1356.

25. Jones, Robert A.; and Hunt, James L.: An Improved Technique for Obtaining Quantitative Aerodynamic Heat-Transfer Data With Surface Coating Materials. Paper No. 65-131, Am. Inst. Aeron. Astronaut., Jan. 1965.

26. Traiger, Harris L.; and Wentworth, Ralph L.: Thermophysical Properties Measurements Performed for NASA. Rep. No. 493, Dynatech Corp., Aug. 27, 1964.

27. Stainback, P. Calvin: Heat-Transfer Measurements at a Mach Number of 8 in the Vicinity of a 90° Interior Corner Alined With the Free-Stream Velocity. NASA TN D-2417, 1964.

28. Cohen, Nathaniel B.: Boundary-Layer Similar Solutions and Correlation Equations for Laminar Heat-Transfer Distribution in Equilibrium Air at Velocities up to 41,100 Feet Per Second. NASA TR R-118, 1961.

29. Eckert, Ernst R. G.: Survey on Heat Transfer at High Speeds. ARL 189 (Contract AF 33(616)-2214), U.S. Air Force, Dec. 1961.

30. Neal, Luther, Jr.; and Bertram, Mitchel H.: Turbulent-Skin-Friction and Heat-Transfer Charts Adapted From the Spalding and Chi Method. NASA TN D-3969, 1967.

31. Inouye, Mamoru; and Lomax, Harvard: Comparison of Experimental and Numerical Results for the Flow of a Perfect Gas About Blunt-Nosed Bodies. NASA TN D-1426, 1962.

32. Lomax, Harvard; and Inouye, Mamoru: Numerical Analysis of Flow Properties About Blunt Bodies Moving at Supersonic Speeds in an Equilibrium Gas. NASA TR R-204, 1964.

33. Whitfield, Jack D.; and Potter, J. Leith: The Unit Reynolds Number as a Parameter in Boundary Layer Stability. AEDC-TN-58-77, ASTIA Doc. No. AD-202731, U.S. Air Force, Oct. 1958.

34. Brinich, Paul F.: Boundary-Layer Transition at Mach 3.12 With and Without Single Roughness Elements. NACA TN 3267, 1954.

35. Laufer, John: Factors Affecting Transition Reynolds Numbers on Models in Supersonic Wind Tunnels. J. Aeron. Sci. (Readers' Forum), vol. 21, no. 7, July 1954, pp. 497-498.

36. Van Driest, E. R.; and Blumer, C. B.: Boundary Layer Transition: Freestream Turbulence and Pressure Gradient Effects. AIAA J., vol. 1, no. 6, June 1963, pp. 1303-1306.

37. Morkovin, Mark V.: On Transition Experiments at Moderate Supersonic Speeds. J. Aeron. Sci., vol. 24, no. 7, July 1957, pp. 480-486.

38. Brinich, Paul F.: Effect of Leading-Edge Geometry on Boundary-Layer Transition at Mach 3.1. NACA TN 3659, 1956.

39. Moeckel, W. E.: Some Effects of Bluntness on Boundary-Layer Transition and Heat Transfer at Supersonic Speeds. NACA Rep. 1312, 1957. (Supersedes NACA TN 3653.)

40. Stainback, P. C.: Some Effects of Roughness and Variable Entropy on Transition at a Mach Number of 8. AIAA Paper No. 67-132, Jan. 1967.

41. Ting, Lu: Effect of Shock-Induced Vorticity on the Compressible Boundary Layer Along a Flat Plate. AIAA J., vol. 2, no. 3, Mar. 1964, pp. 490-493.

42. Reshotko, Eli; and Beckwith, Ivan E.: Compressible Laminar Boundary Layer Over a Yawed Infinite Cylinder With Heat Transfer and Arbitrary Prandtl Number. NACA Rep. 1379, 1958. (Supersedes NACA TN 3986.)

High - temperature plastic

Aluminum

.00254

.00635

.0127

.127

.00635

1456

.0254

.102

724

High - temperature plastic

Aluminum

.00254

.00635

.05321

3049
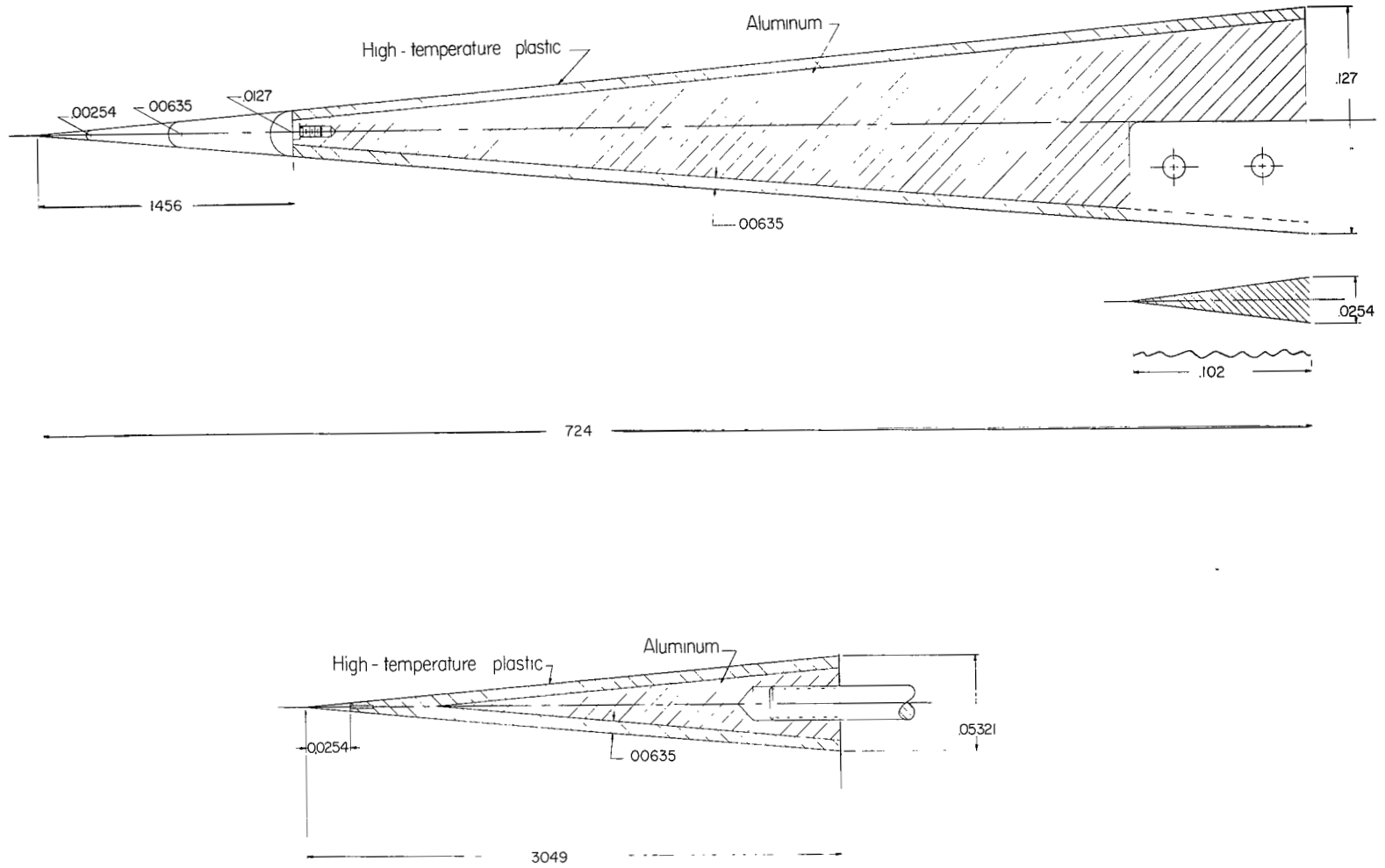
Figure 1.- Geometry of models. All dimensions are in meters.
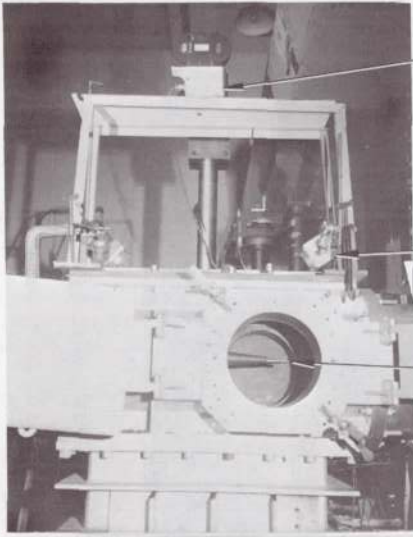
Camera

Strobe lights

Model in test section
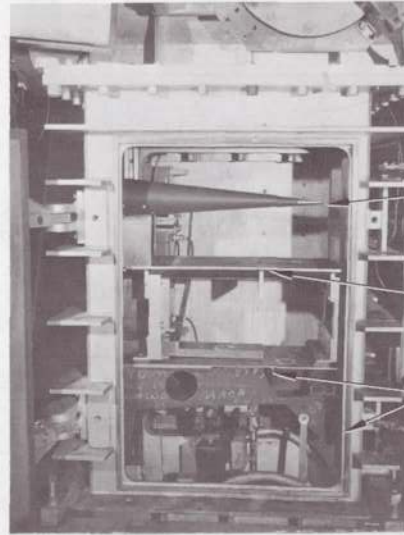
Model retracted from
test section

Moveable fairing plate

Injection mechanism
and housing

Figure 2.- Photograph of test setup.

L-68-8591
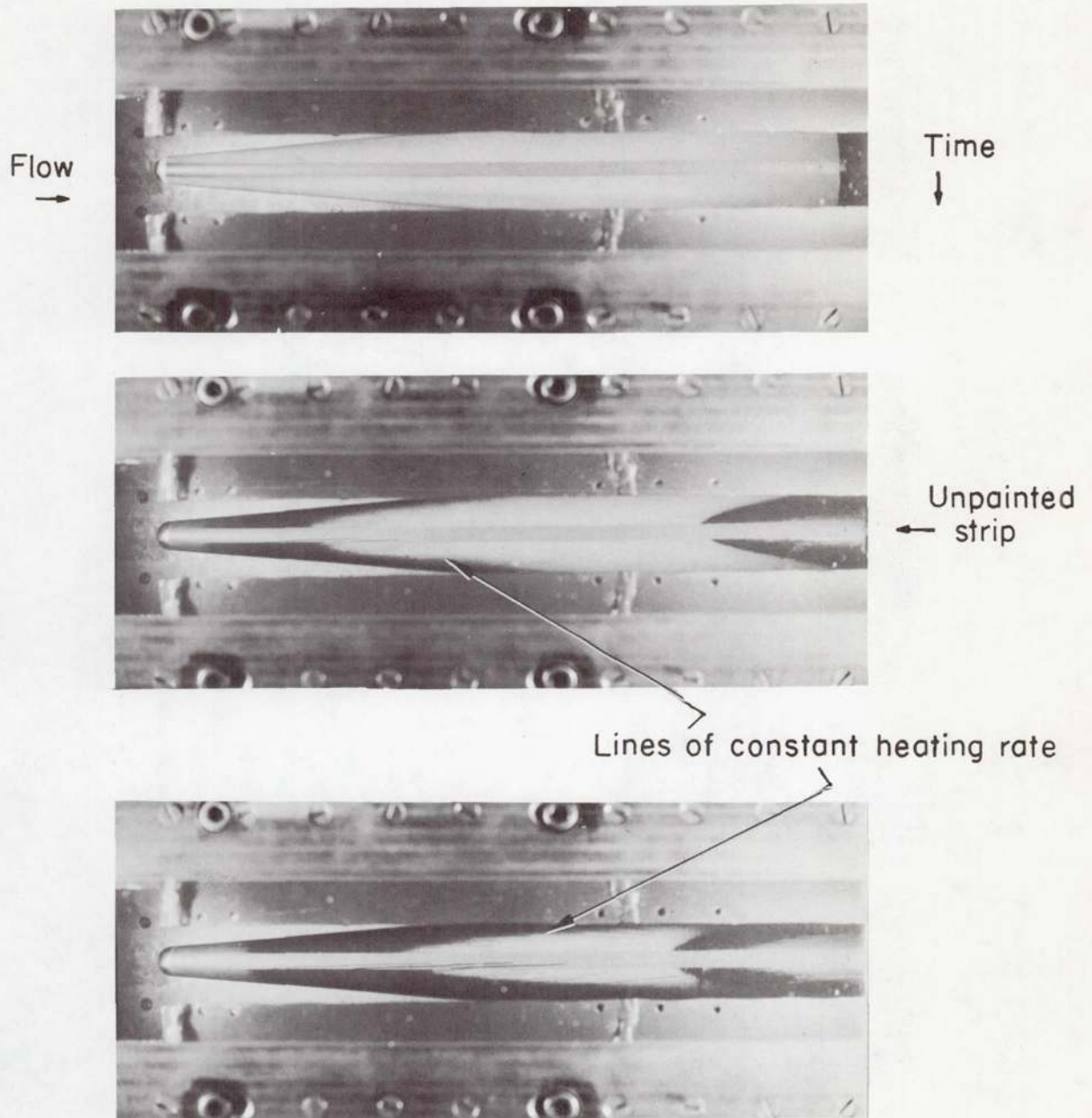
Figure 3.- Typical flow pattern obtained with temperature-sensitive paint. $\alpha = 1^0$ (lee side); $\theta_c = 5^0$; $r_n = 12.7$ mm; $R_s = 3.94 \times 10^7$ m$^{-1}$.
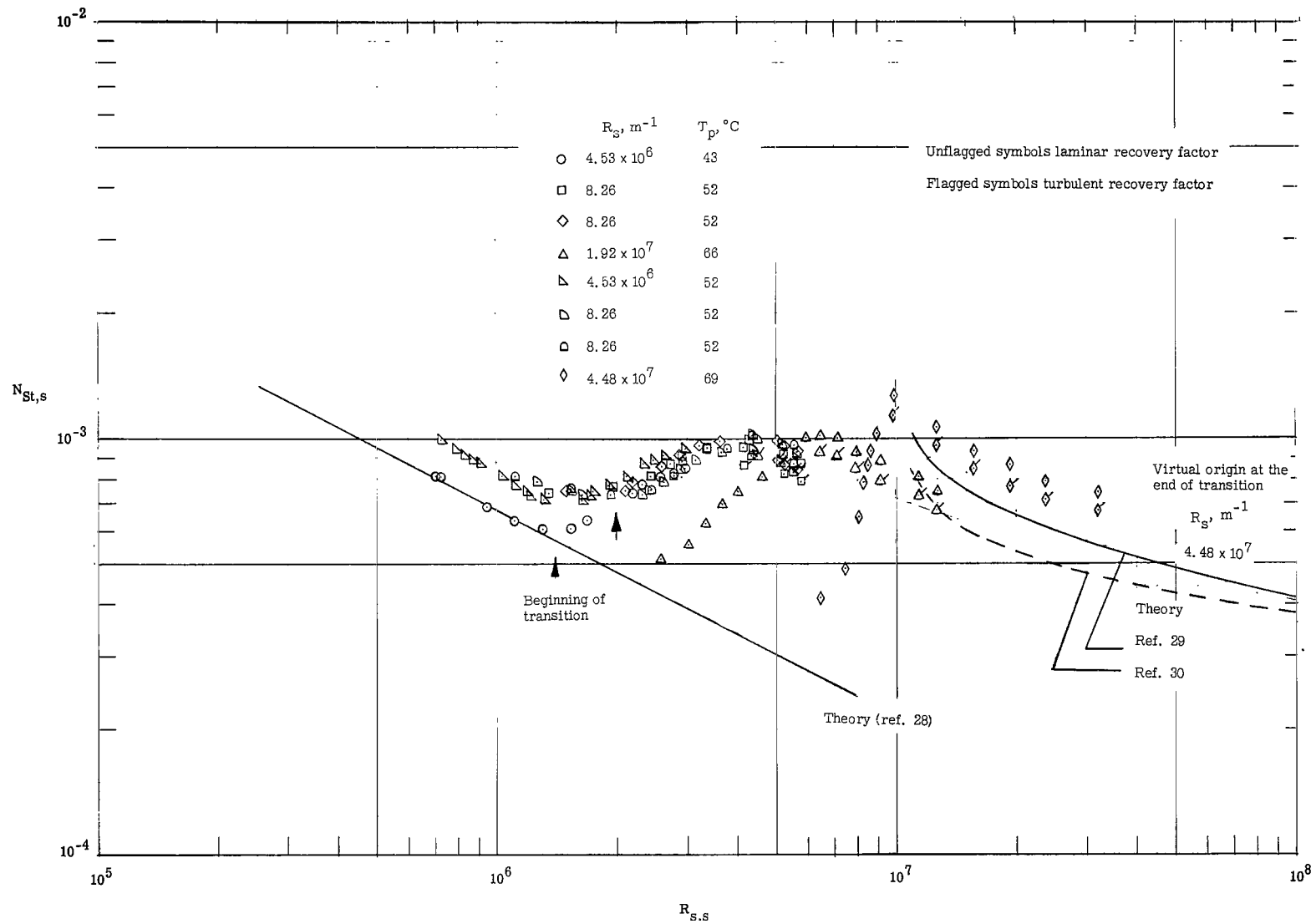
Figure 4.- Stanton-Reynolds number variation for $5^0$ sharp cone. $l = 0.7240$ m.

$R_S$, m.$^{-1}$

$\triangle$    $4.53 \times 10^6$

$\diamondsuit$    8.26

$\rangle$    $1.92 \times 10^7$

$\triangle$    4.48

Unflagged symbols laminar recovery factor

Flagged symbols turbulent recovery factor

Solid symbols - data reduced assuming model an infinite cylinder

—— —— Fairing through data

Theory

Ref. 29

Virtual origin at the
end of transition

$R_S = 4.48 \times 10^7 \, m^{-1}$

Ref. 30

$N_{St,s}$

Beginning of
metal mandrel

Theory (ref. 28)

Beginning of
transition

$R_{s,s}$
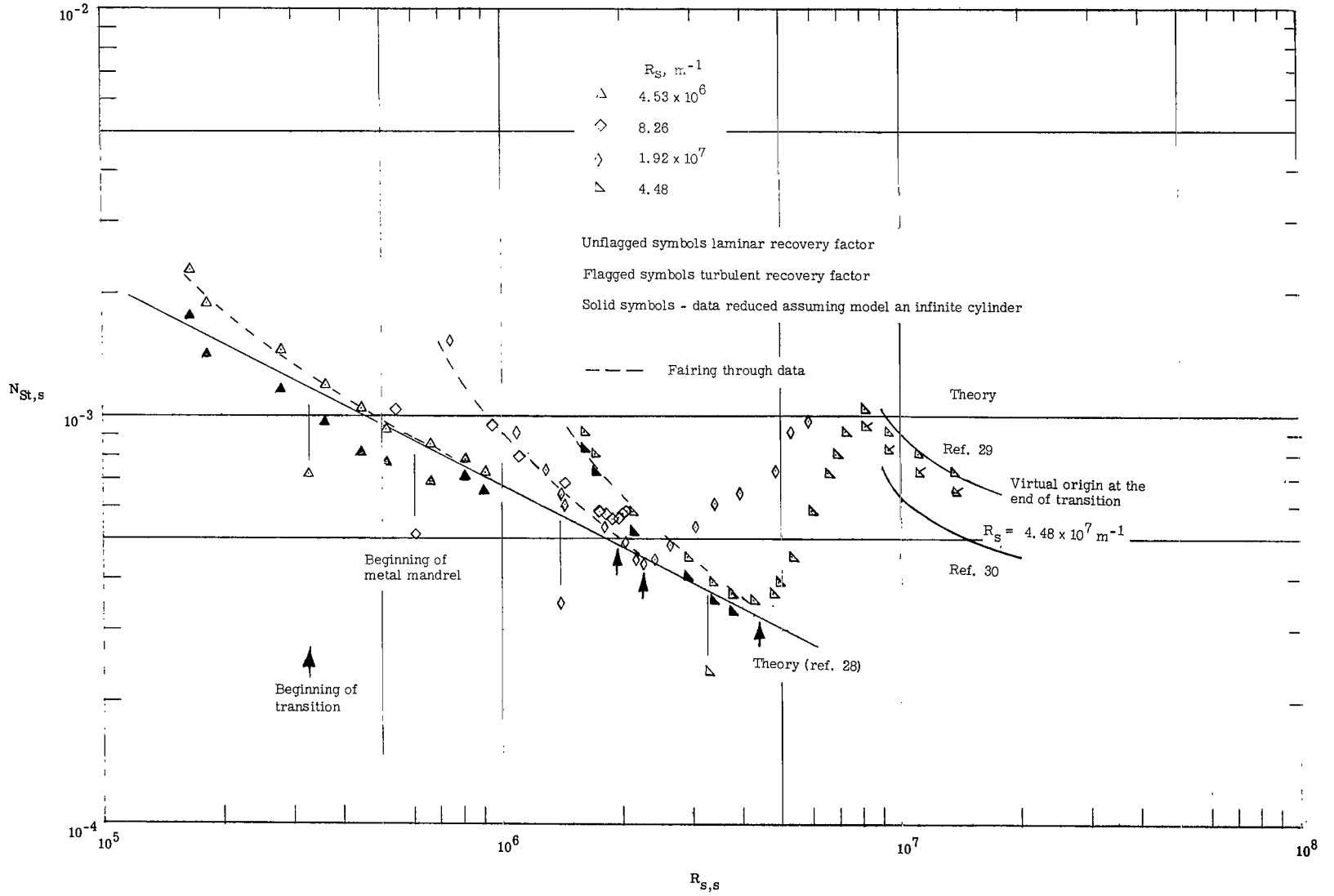
Figure 5.- Stanton-Reynolds number variation for $5^0$ sharp cone. $\it{l} = 0.3049$ m.
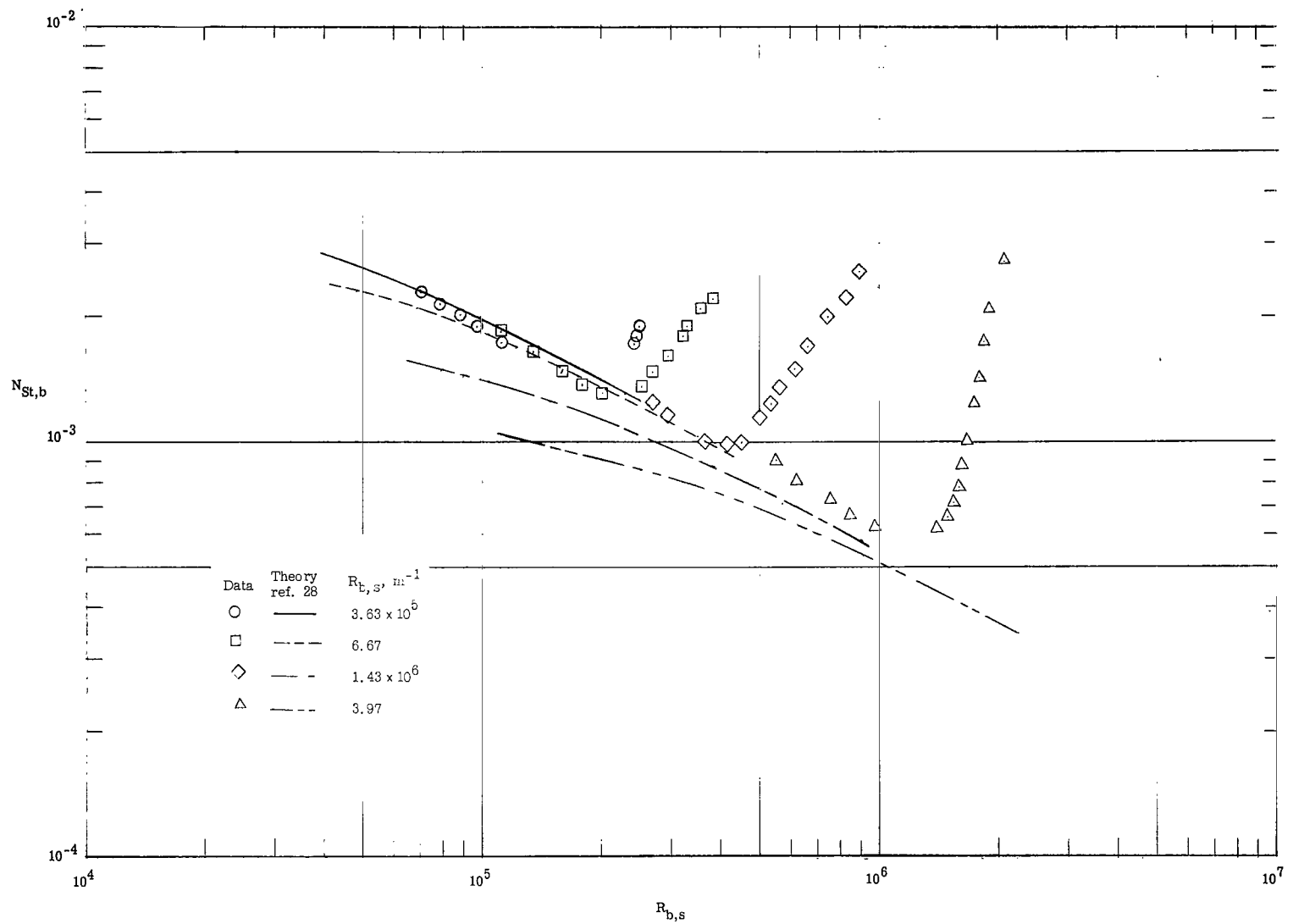
(a) $r_n$ = 2.54 mm.

Figure 6.- Variation of Stanton number with Reynolds number for blunt-cone data using normal-shock entropy.
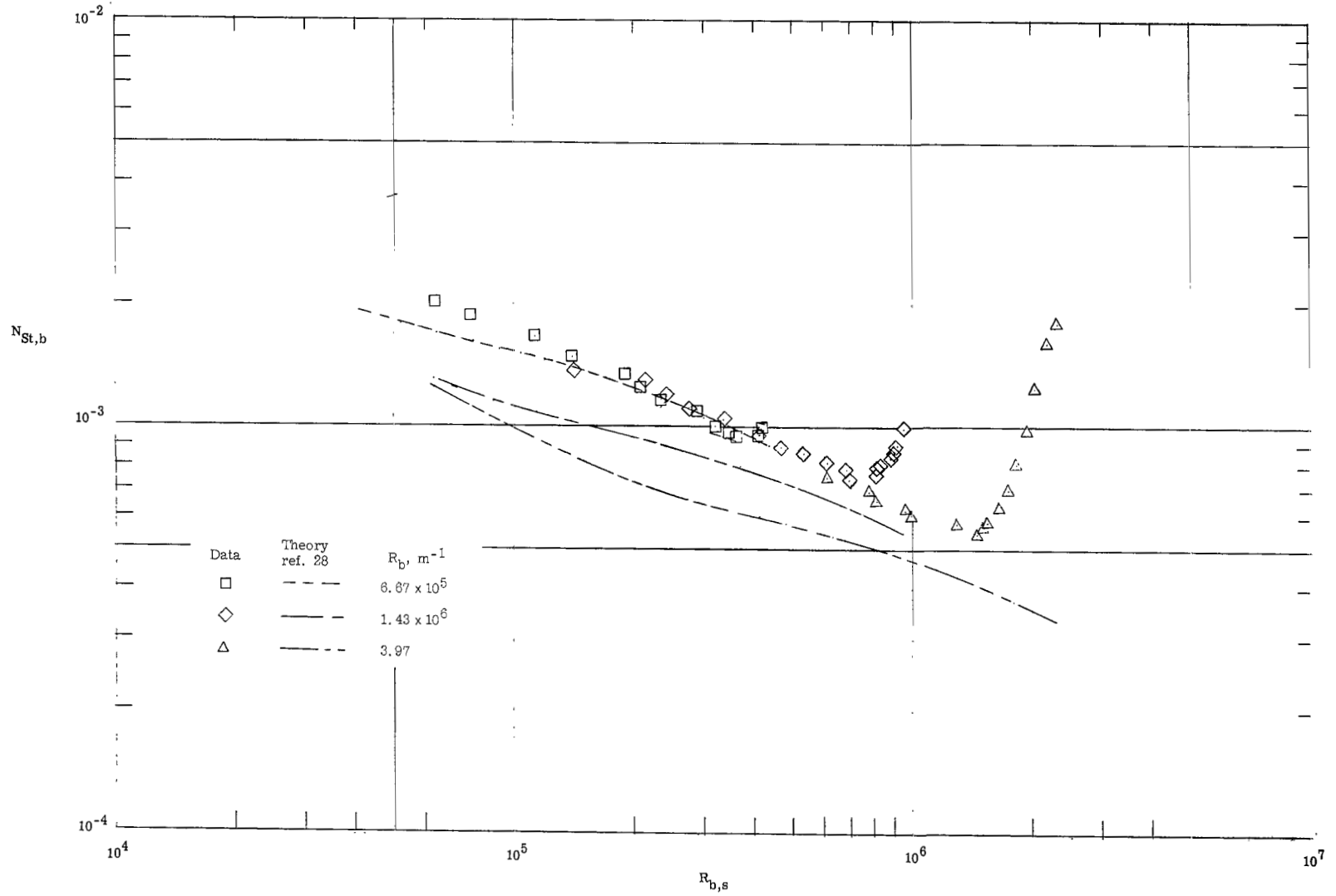
(b)  $r_n$ = 6.35 mm.

Figure 6.- Continued.
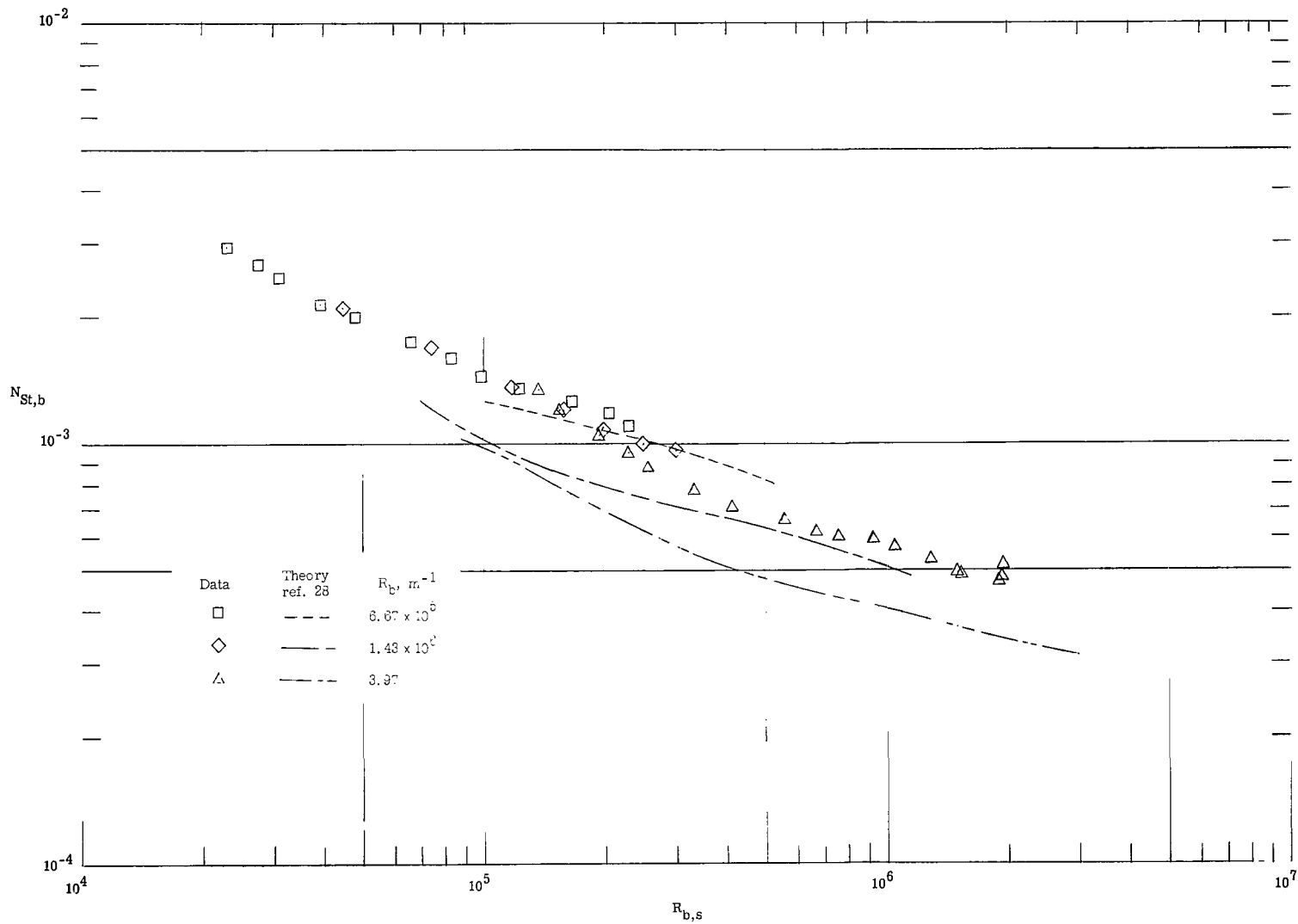
(c) $r_n$ = 12.7 mm.

Figure 6.- Concluded.
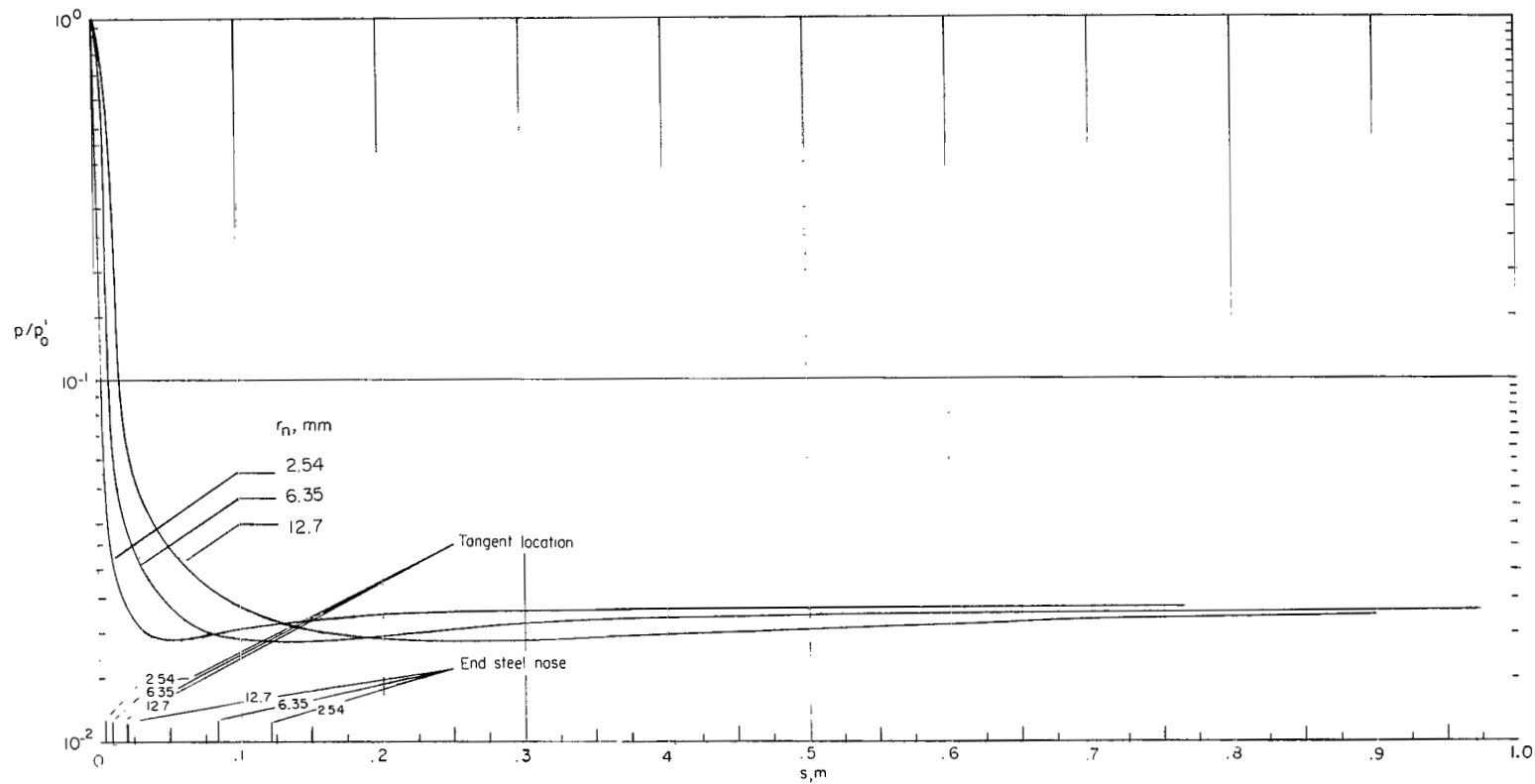
Figure 7.- Pressure distribution along blunted 5° cone.
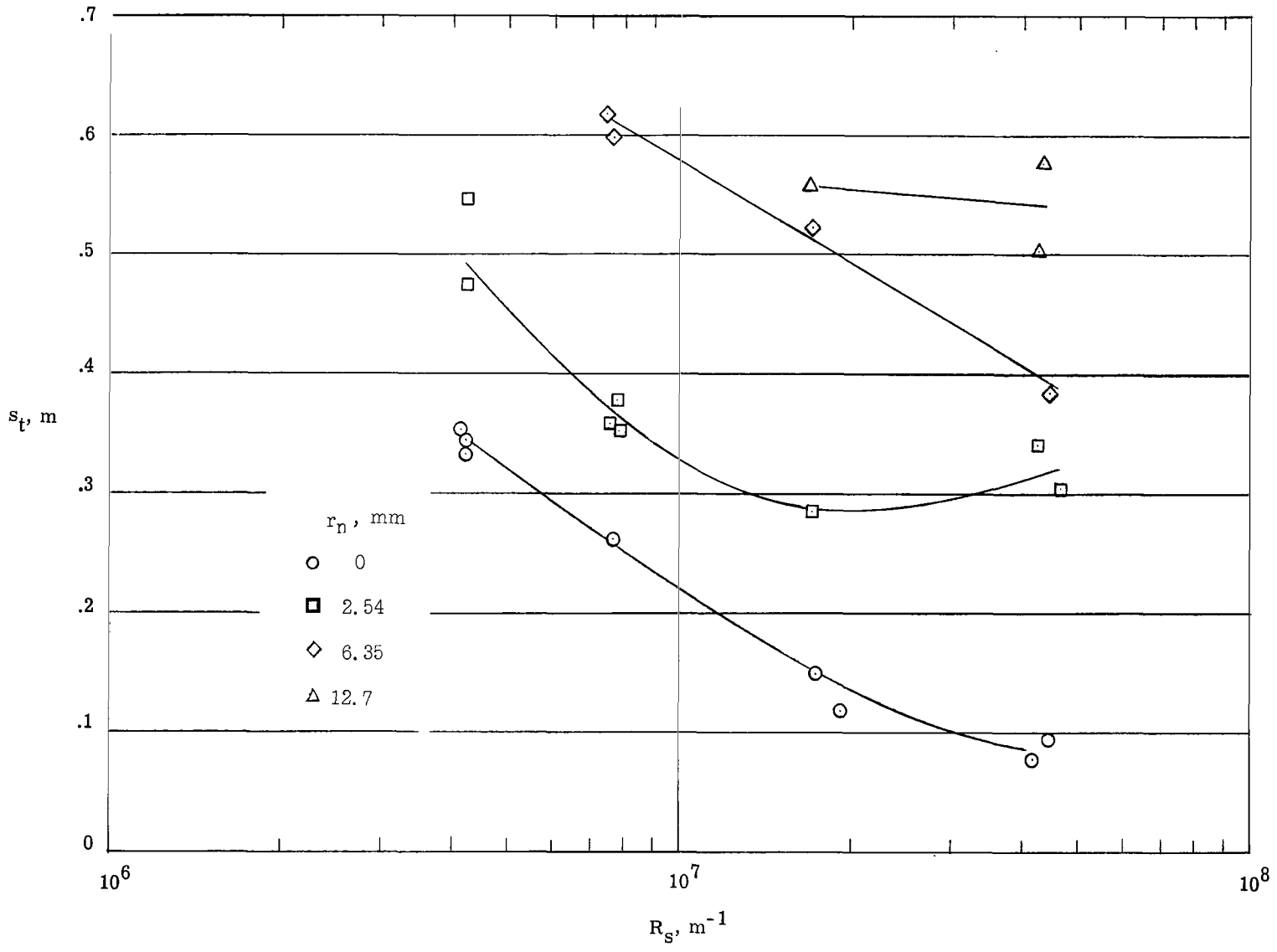
Figure 8.- Location of transition variation with unit Reynolds number. $\alpha = 0^0$.
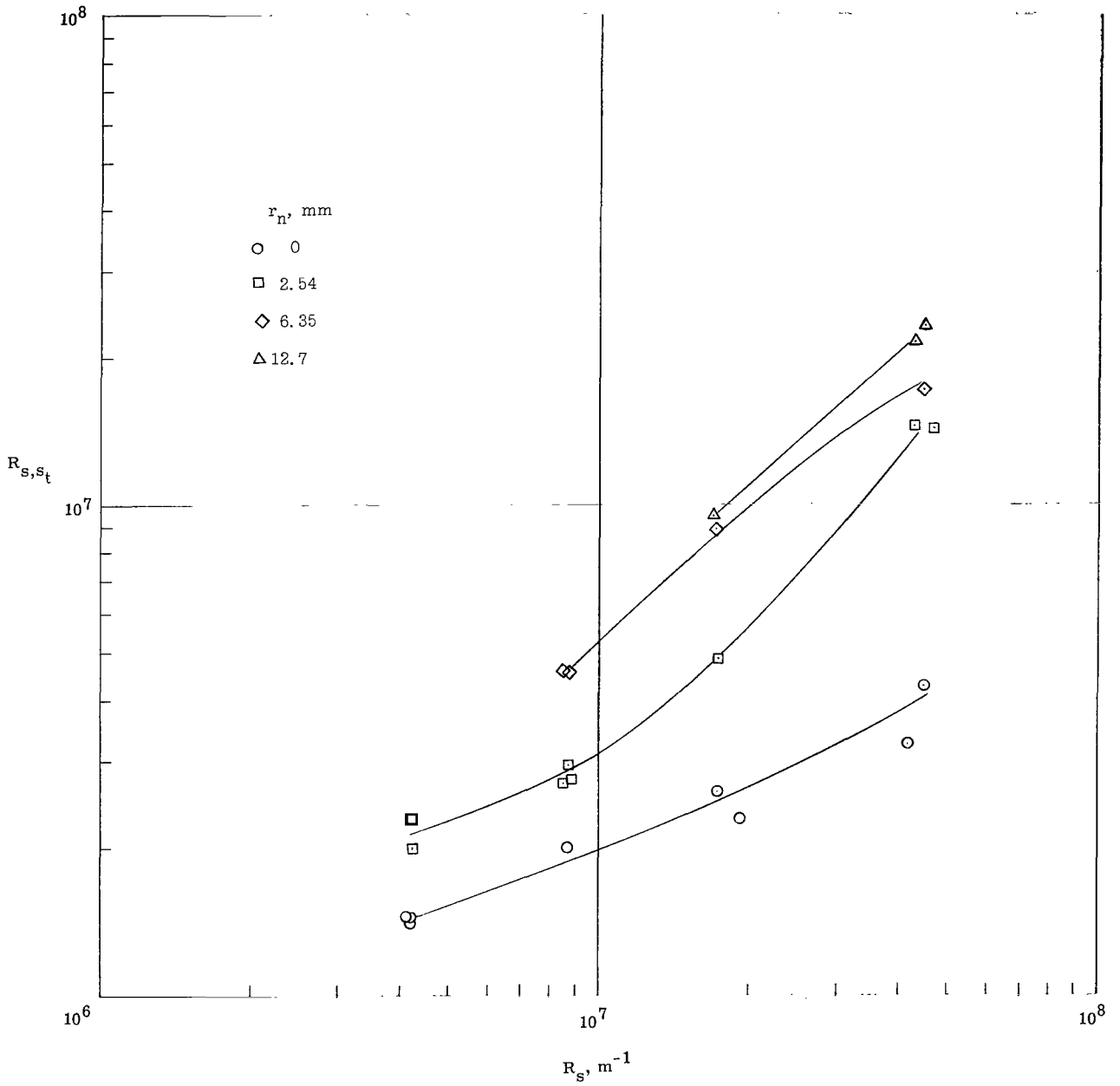
Figure 9.- The variation of transition Reynolds number with unit Reynolds number. $\alpha = 0^0$.
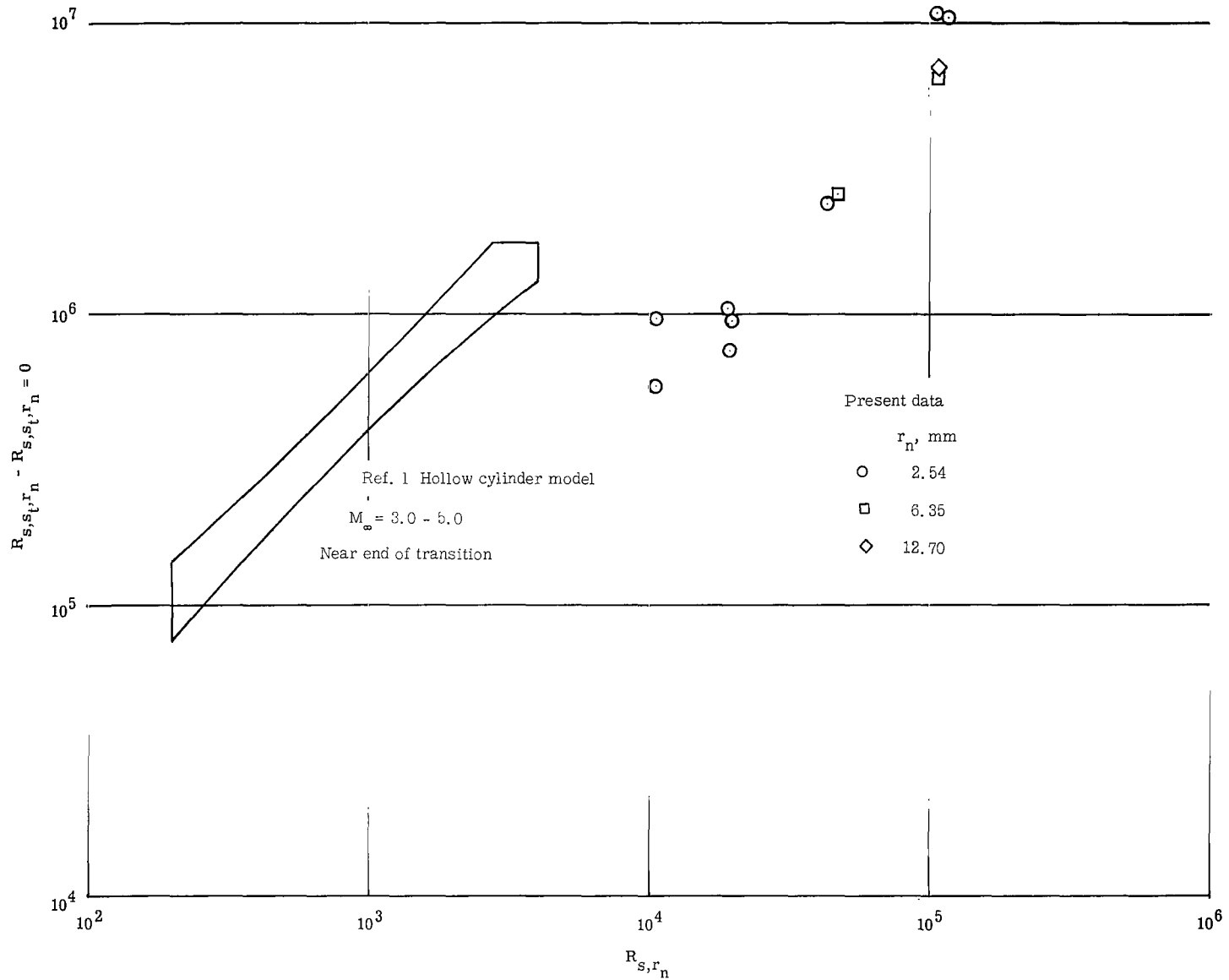
Figure 10.- The change in transition Reynolds number due to bluntness as a function of nose radius Reynolds number.
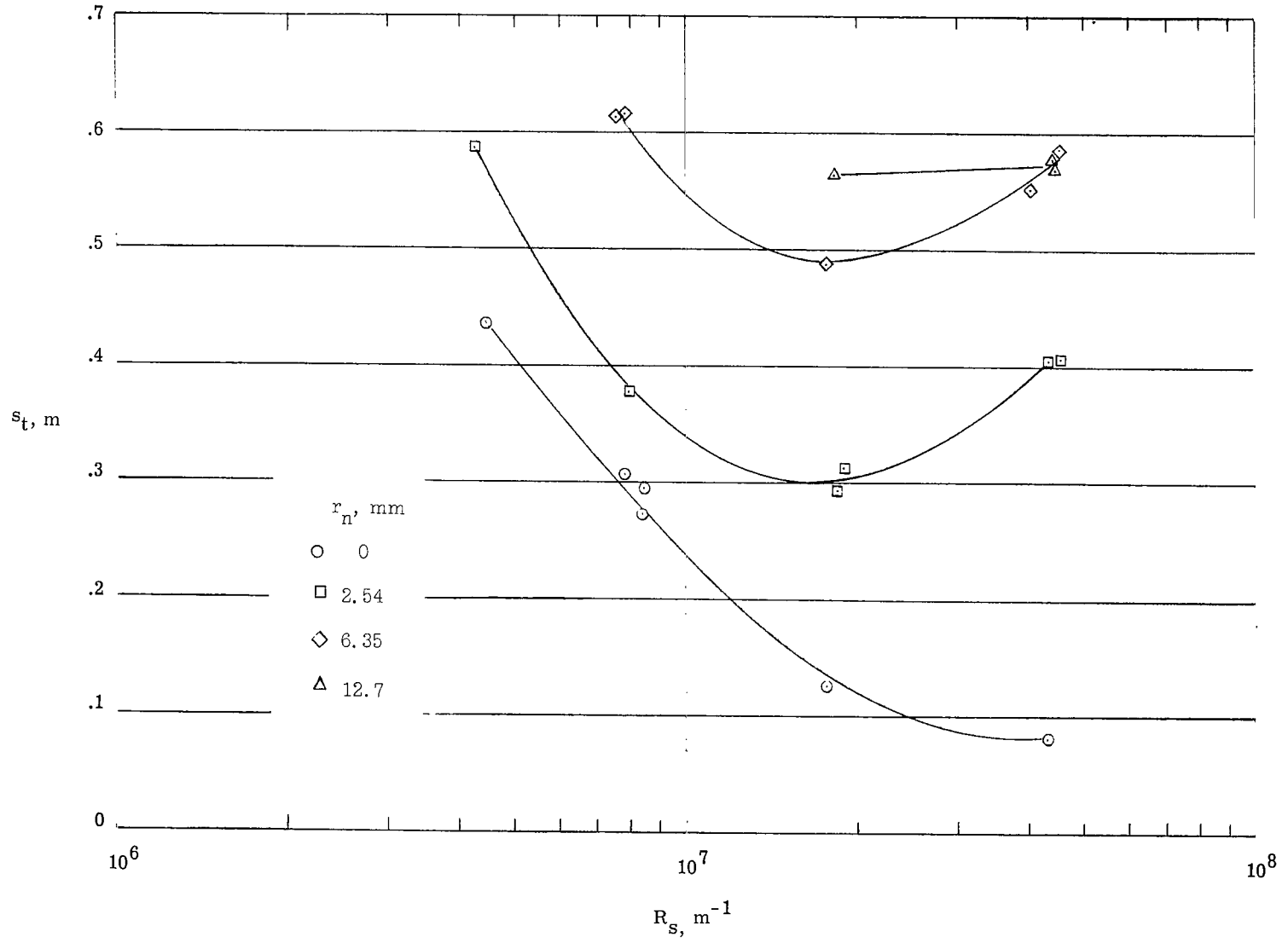
(a) $\alpha = 1^o$; windward ray.

Figure 11.- Location of transition as a function of unit Reynolds number.
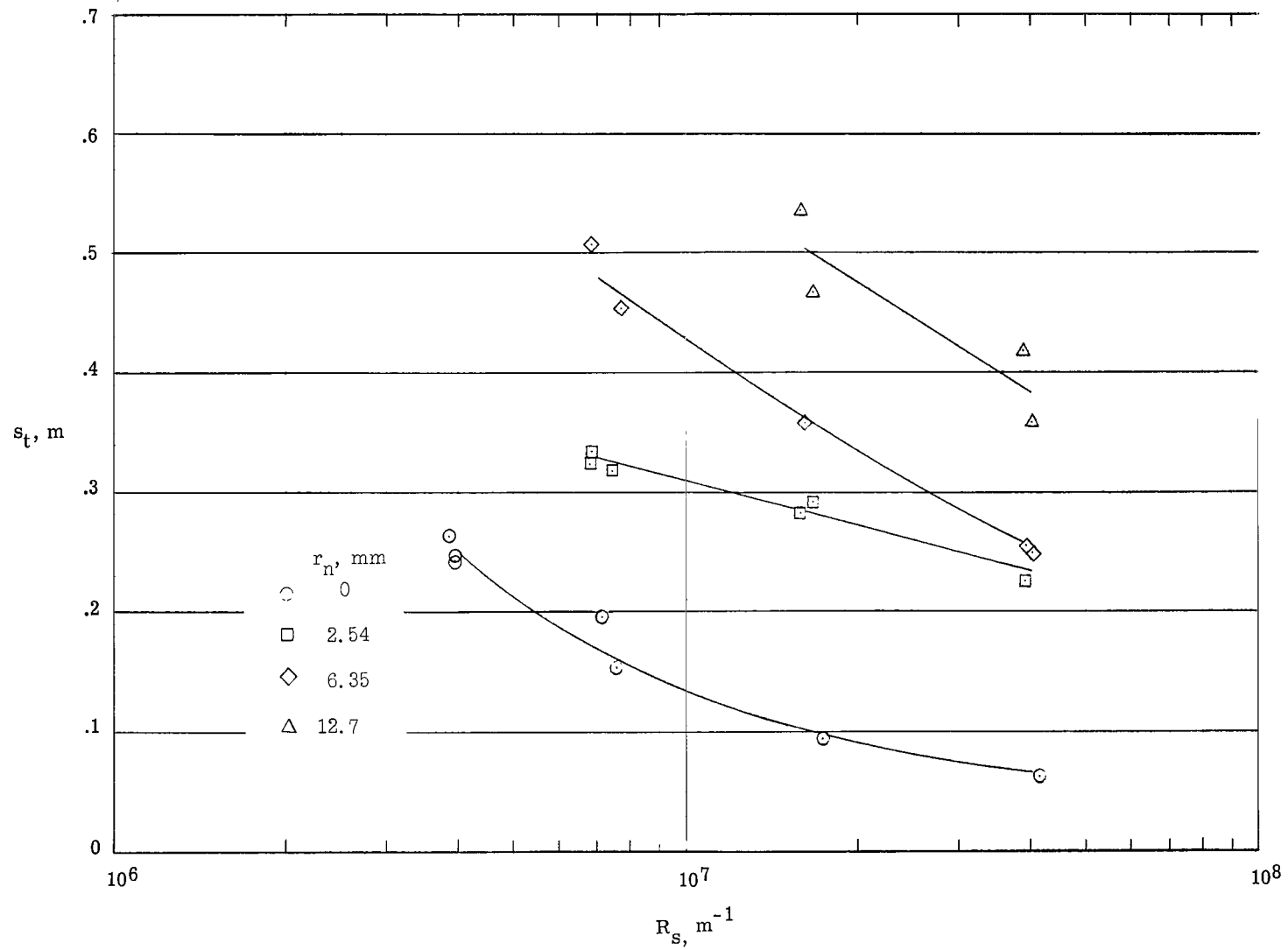
(b) $\alpha = 1^0$; leeward ray.

Figure 11.- Concluded.
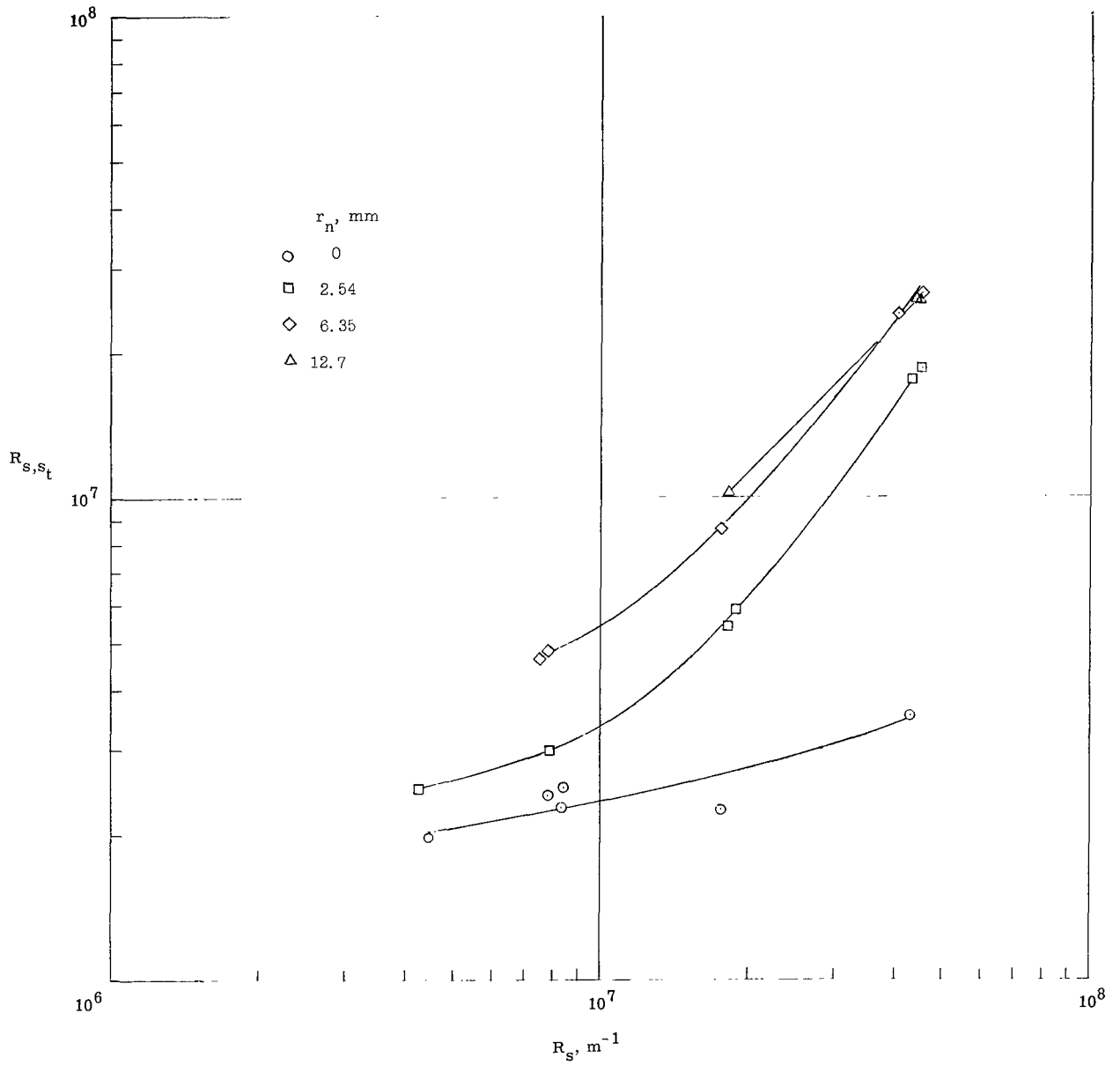
(a) $\alpha = 1^{\circ}$; windward ray.

Figure 12.- The variation of transition Reynolds number with unit Reynolds number.

42
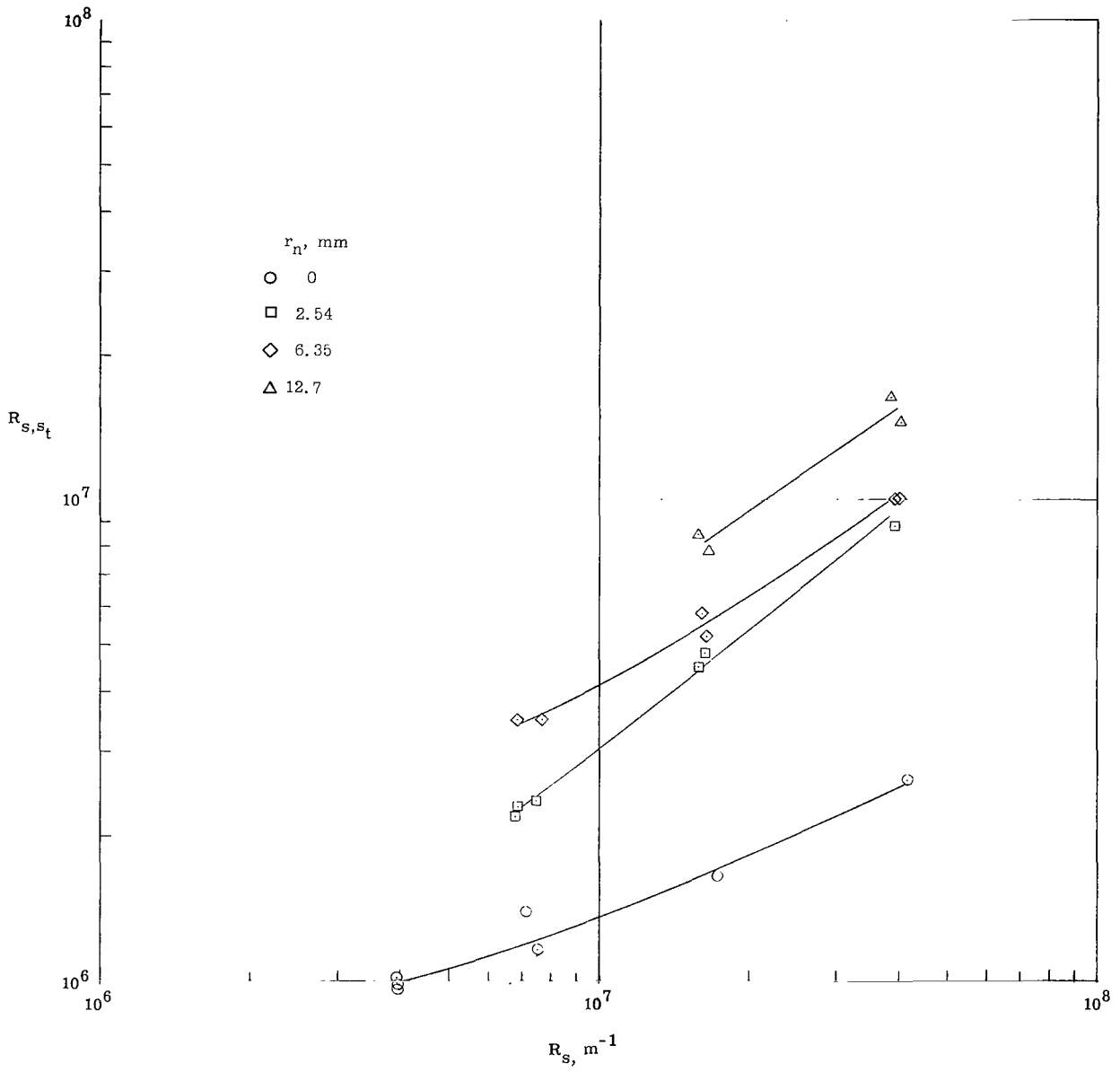
(b) $\alpha = 1^0$; leeward ray.

Figure 12.- Concluded.
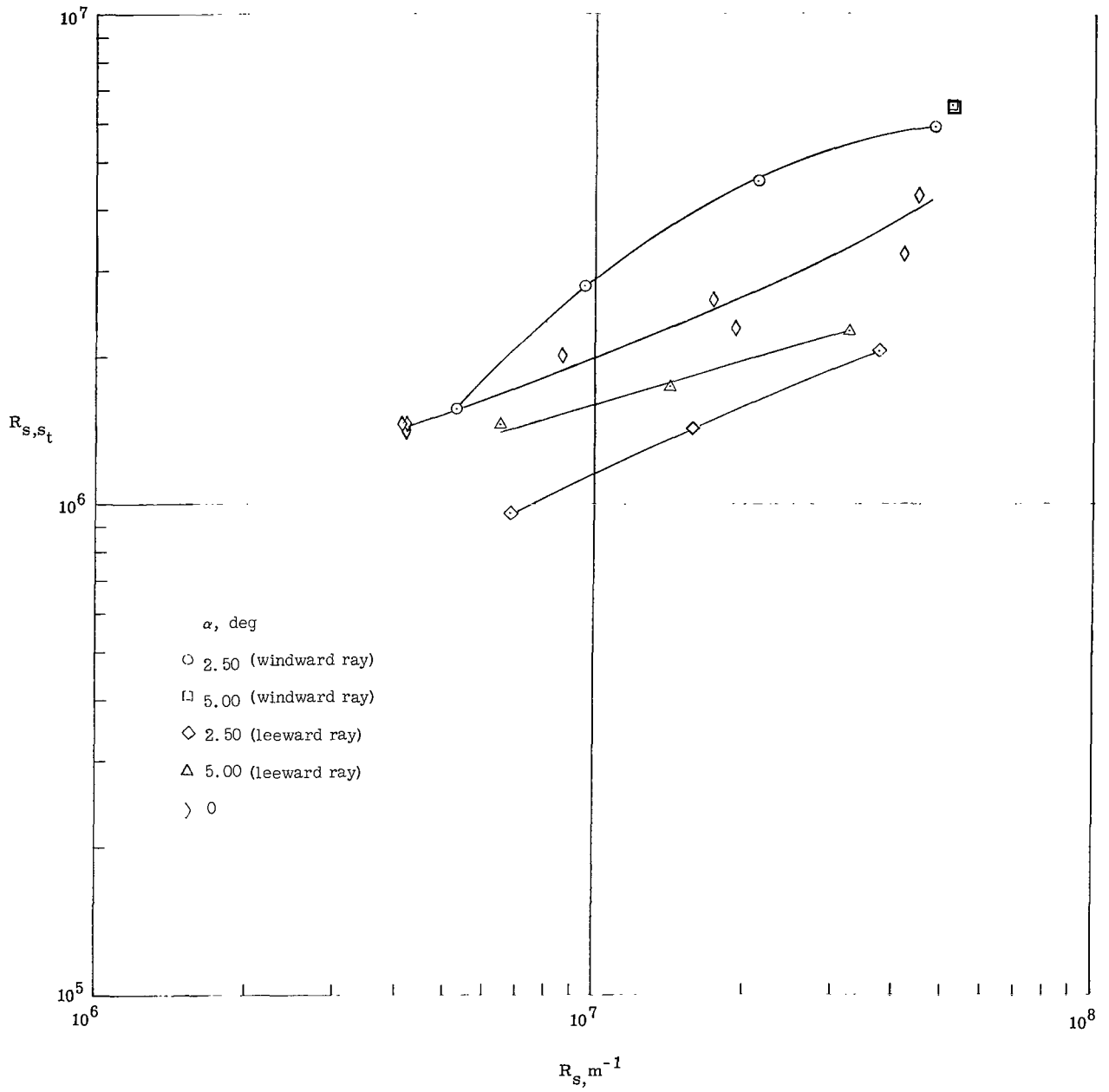
Figure 13.- The variation of transition Reynolds number with unit Reynolds number for sharp cone. $r_n = 0$.

The y-axis is labeled $R_{s,s_t}$ ranging from $10^5$ to $10^7$.

The x-axis is labeled $R_{s,}m^{-1}$ ranging from $10^6$ to $10^8$.

Legend:
$\alpha$, deg
- ○ 2.50 (windward ray)
- ◻ 5.00 (windward ray)
- ◇ 2.50 (leeward ray)
- △ 5.00 (leeward ray)
- ⟩ 0
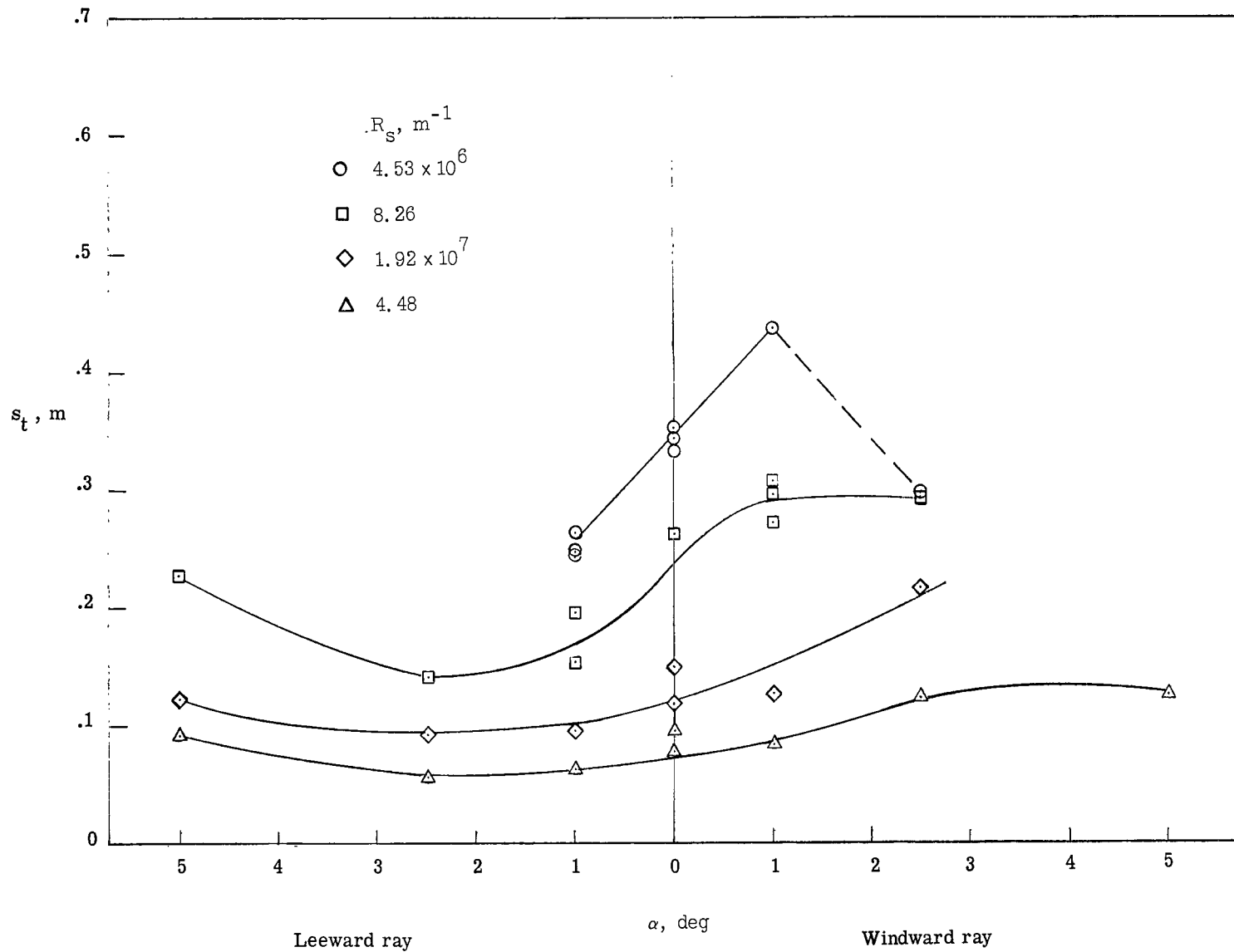
Figure 14.- The variation of transition location for a sharp cone with angle of attack.
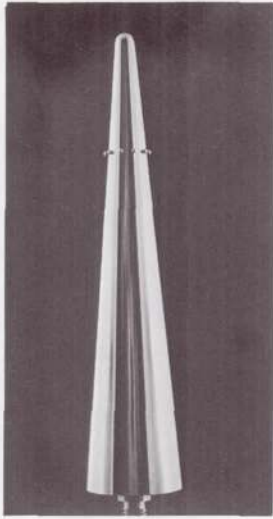
$r_n$ = 2.54 mm
$k$ = 1.194 mm
$x_k$ = 31.12 mm
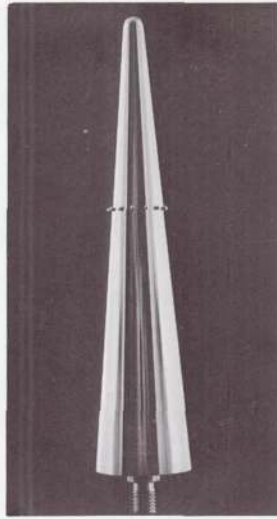
$r_n$ = 2.54 mm
$k$ = 1.194 mm
$x_k$ = 50.06 mm
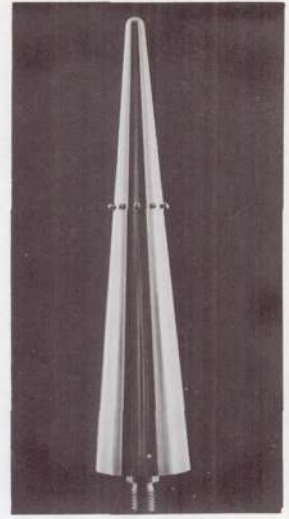
$r_n$ = 2.54 mm
$k$ = 1.600 mm
$x_k$ = 50.06 mm
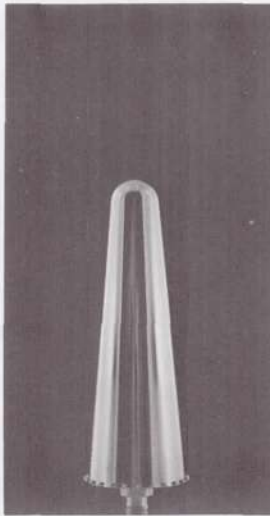
$r_n$ = 6.350 mm
$k$ = 1.194 mm
$x_k$ = 78.64 mm
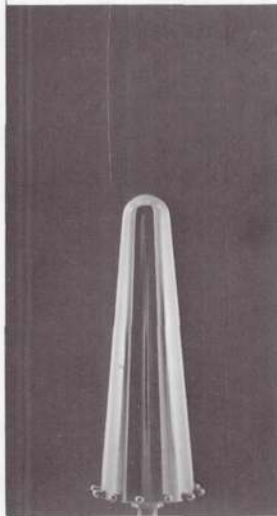
$r_n$ = 6.350 mm
$k$ = 2.388 mm
$x_k$ = 78.08 mm
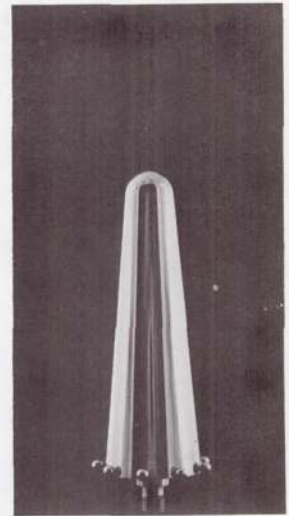
$r_n$ = 6.350 mm
$k$ = 3.175 mm
$x_k$ = 77.72 mm

Figure 15.- Nose and roughness geometry.                    L-68-8593

$r_n$ = 2.54 mm

k = 1.19 mm

$x_k$ = 31.11 mm

$R_S$ = 1.73 x $10^7$ $m^{-1}$

k/$\delta$* = 1.975
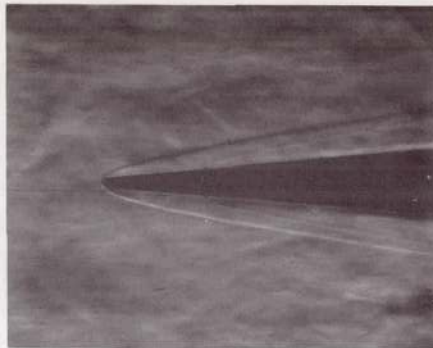
$r_n$ = 2.54 mm

k = 1.19 mm

$x_k$ = 50.23 mm

$R_S$ = 1.73 x $10^7$ $m^{-1}$

k/$\delta$* = 2.03

$r_n$ = 2.54 mm

k = 1.59 mm

$x_k$ = 50.04 mm

$R_S$ = 1.73 x $10^7$ $m^{-1}$

k/$\delta$* = 2.765
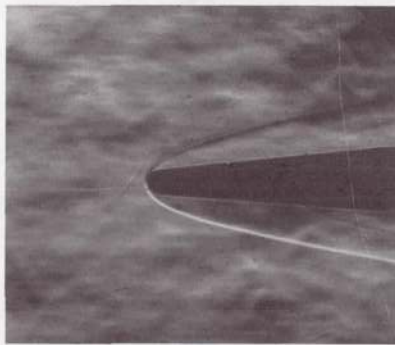
$r_n$ = 6.35 mm

k = 1.19 mm

$x_k$ = 78.6 mm

$R_S$ = 1.73 x $10^7$ $m^{-1}$

k/$\delta$* = 1.575
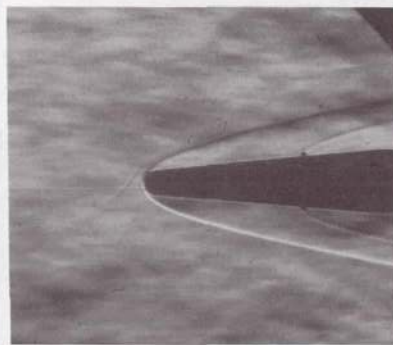
$r_n$ = 6.35 mm

k = 2.39 mm

$x_k$ = 78.1 mm

$R_S$ = 1.73 x $10^7$ $m^{-1}$

k/$\delta$* = 3.158

$r_n$ = 6.35 mm

k = 3.18 mm

$x_k$ = 77.7 mm

$R_S$ = 1.73 x $10^7$ $m^{-1}$

k/$\delta$* = 4.211

Figure 16.- Nose-roughness element shock geometry.

L-68-8594
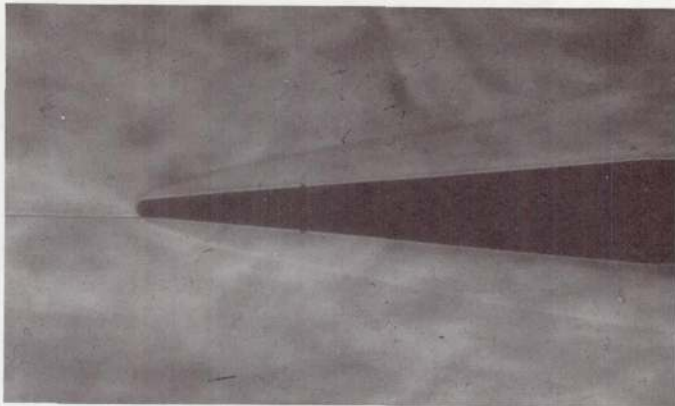
$r_n = 2.54$ mm

$k = 1.119$ mm

$x_k = 50.23$ mm

$R_S = 4.53 \times 10^6$ m$^{-1}$

$k/\delta* = .9835$
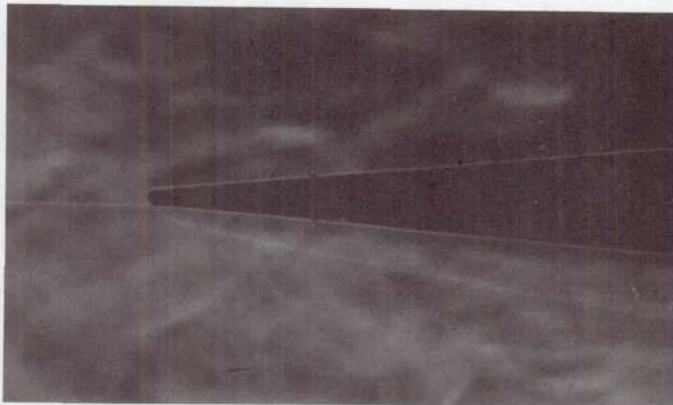


$r_n = 2.54$ mm

$k = 1.59$ mm

$x_k = 50.04$ mm

$R_S = 4.53 \times 10^6$ m$^{-1}$

$k/\delta* = 1.316$
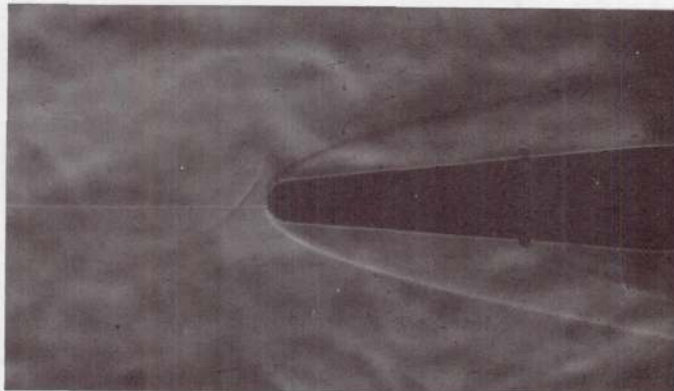


$r_n = 6.35$ mm

$k = 3.18$ mm

$x_k = 77.7$ mm

$R_S = 4.53 \times 10^6$ m$^{-1}$

$k/\delta* = 2.012$

Figure 16.- Concluded.

L-68-8595

| | $r_n$, mm | $k$, mm | $x_k$, mm | $\frac{s_k}{r_n}$ |
|---|---|---|---|---|
| ○ | 2.54 | 1.19 | 31.11 | 12.87 |
| □ | 2.54 | 1.59 | 50.04 | 20.35 |
| ◇ | 2.54 | 1.19 | 50.23 | 20.43 |

$s_t$, m

Faired curve from fig. 8

Effective $R_s$ for ◇

$s_k$

$R_s$, $m^{-1}$
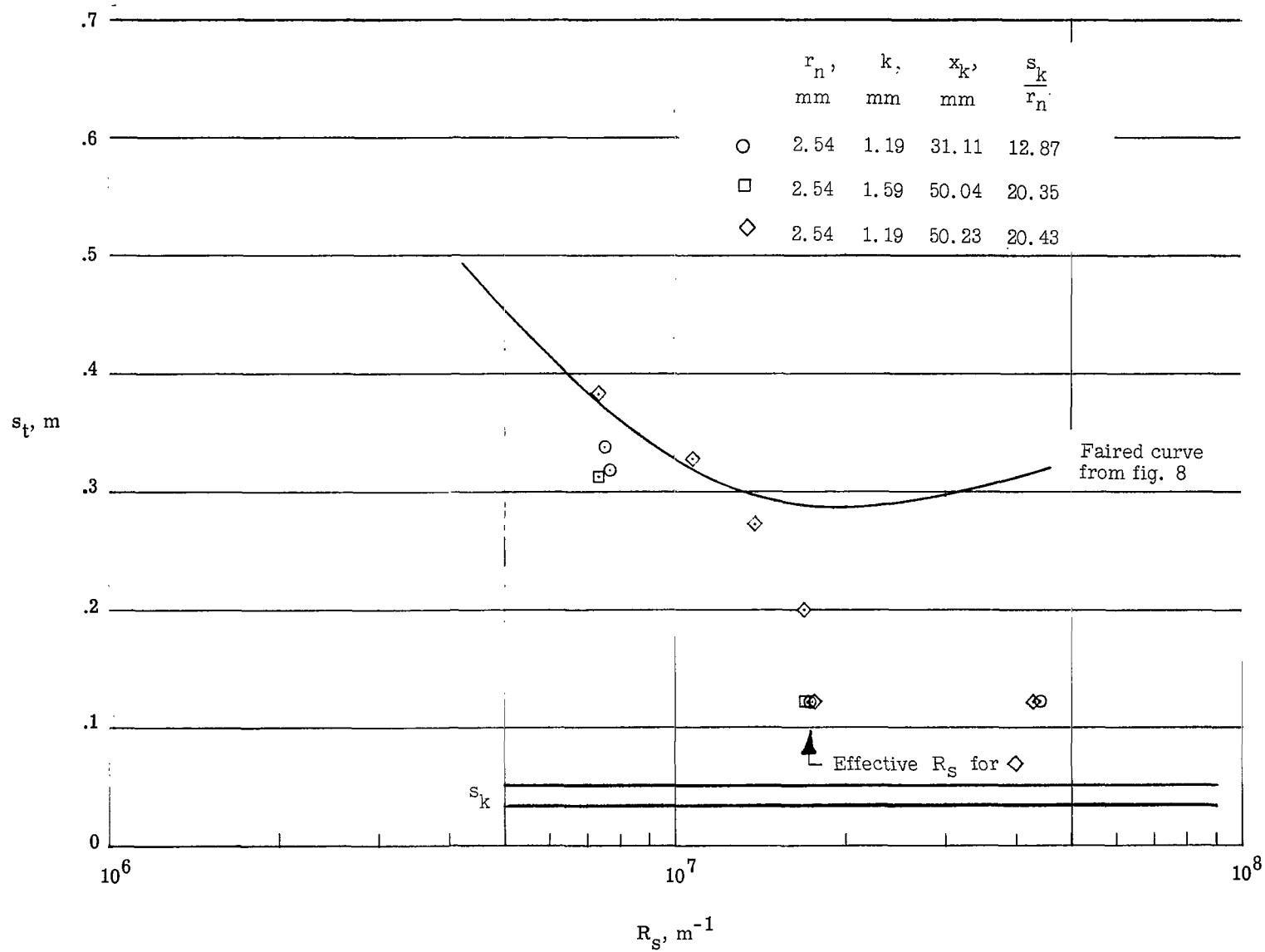
(a) $r_n$ = 2.54 mm.

Figure 17.- Effect of spherical roughness elements on location of transition.

|  | $r_n$, mm | $k$, mm | $x_k$, mm | $\dfrac{s_k}{r_n}$ |
|---|---|---|---|---|
| ○ | 6.35 | 1.19 | 78.6 | 12.99 |
| □ |  | 2.39 | 78.1 | 12.91 |
| ◇ |  | 3.18 | 77.7 | 12.85 |

Faired curve from fig. 8

$s_t$, m

$s_k$

$R_s$, m$^{-1}$
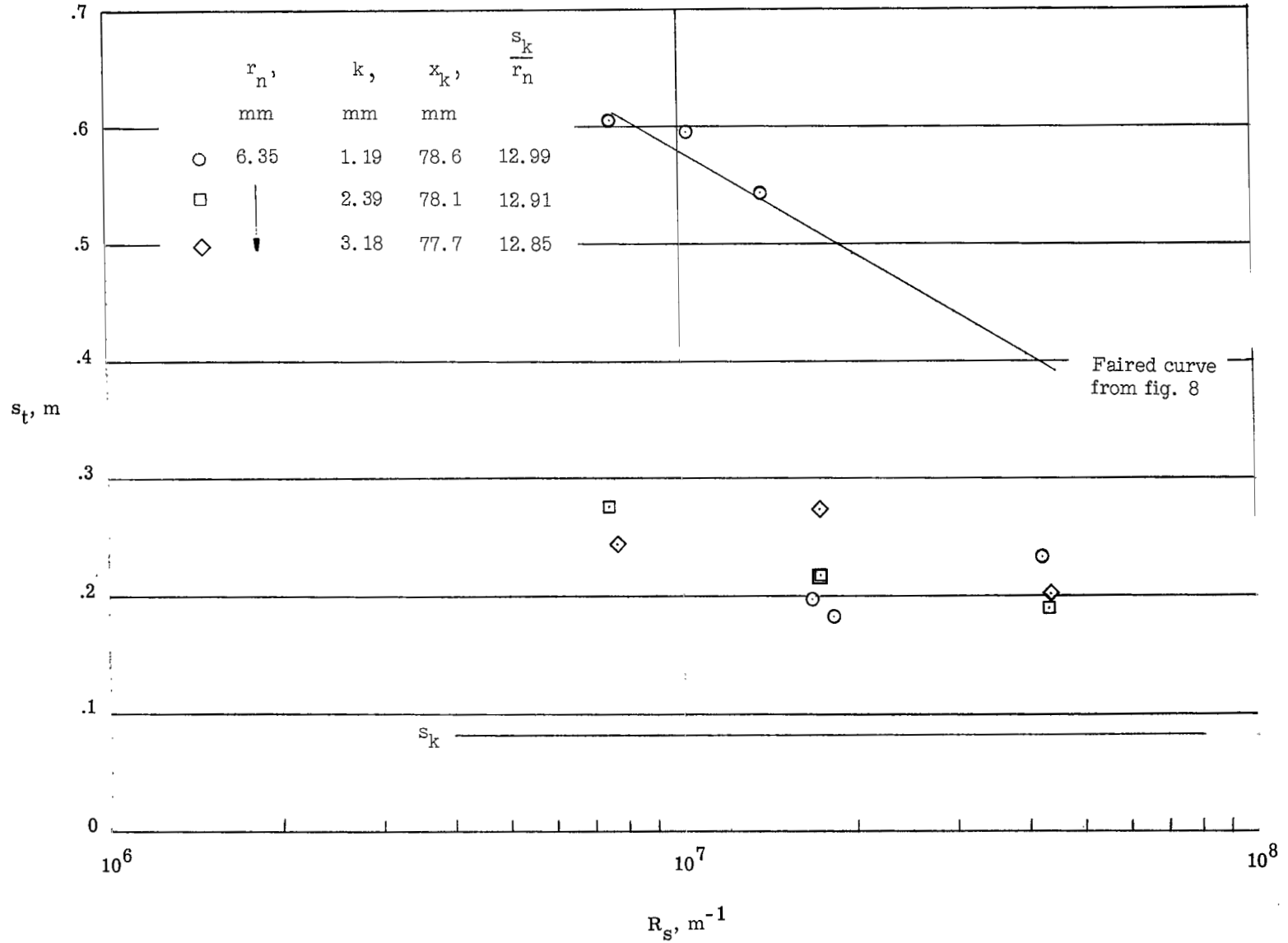
(b)  $r_n$ = 6.35 mm.

Figure 17.- Concluded.

Flow →    Time ↓
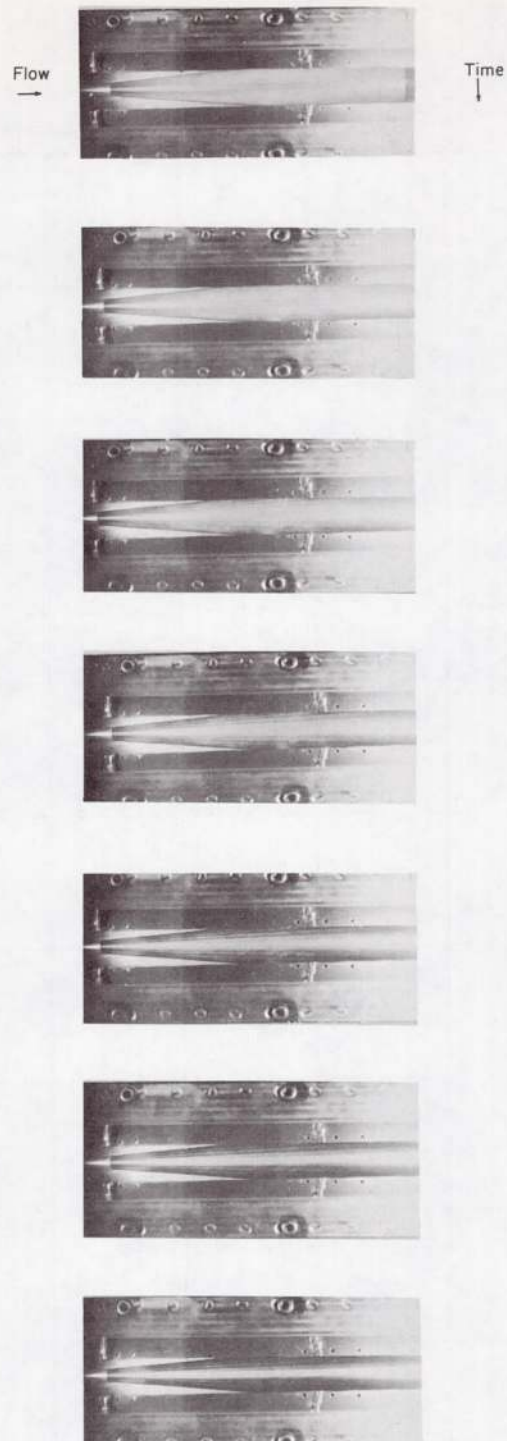
$r_n = 6.35$ mm    $\dfrac{k}{\delta^*} = 2.65$

$x_k = 78.6$ mm    $k = 1.19$ mm

Figure 18.- Photographs of striae on a model due to spherical roughness elements.    L-68-8596
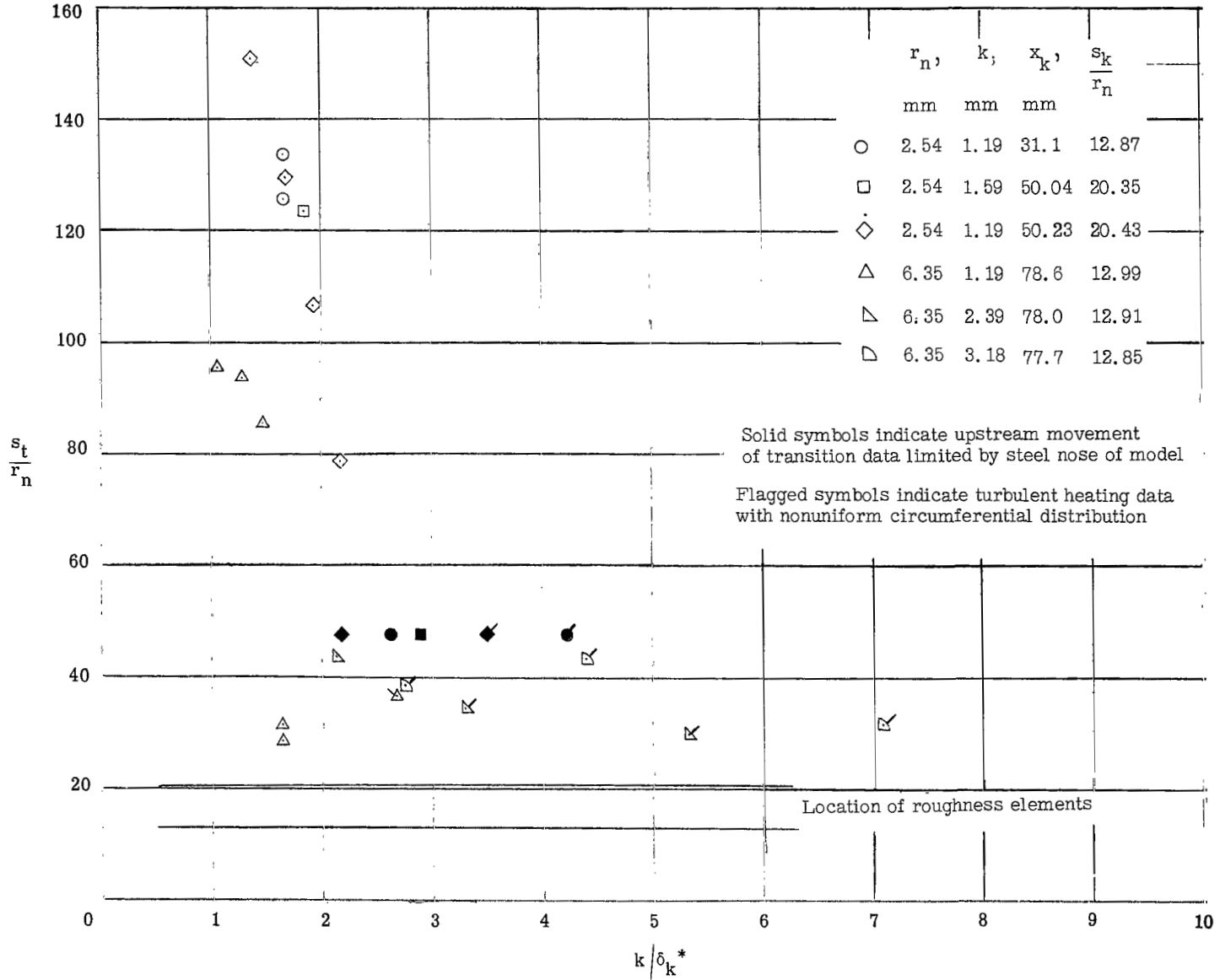
Figure 19.- Effect of $k/\delta_k^*$ on the location of transition for spherical roughness elements.

$r_n = 2.54$ mm , $x_k = 50.06$ mm , $k/\delta_k^* = 3.5$

$N_{St,s}$

High heating region

Virtual origin at roughness

Low heating region

Ref. 29 } Theory
Ref. 30 }

Roughness

End steel nose

$R_{s,s}$
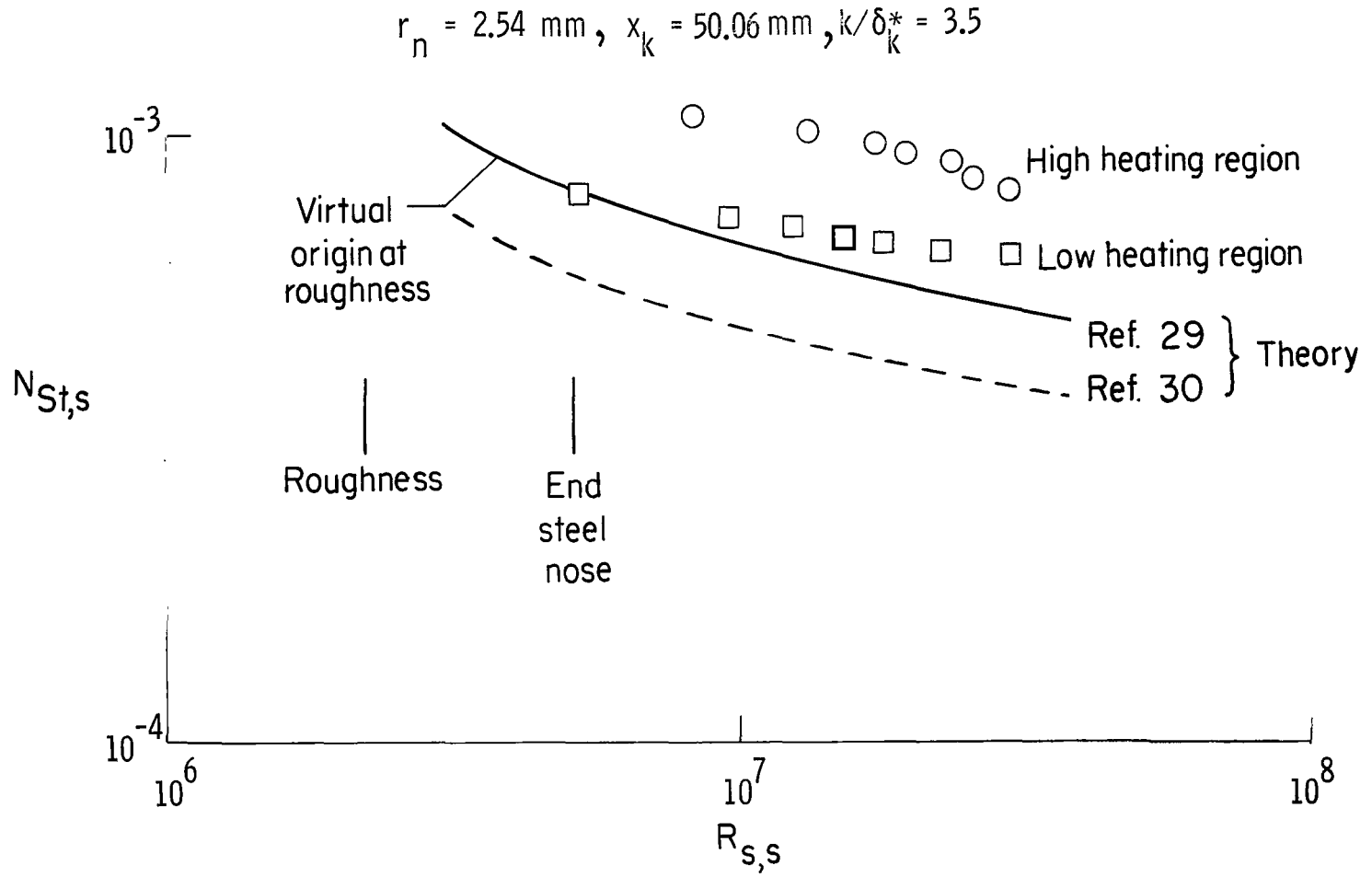
Figure 20.- Nonuniform turbulent heating downstream of spherical roughness elements.
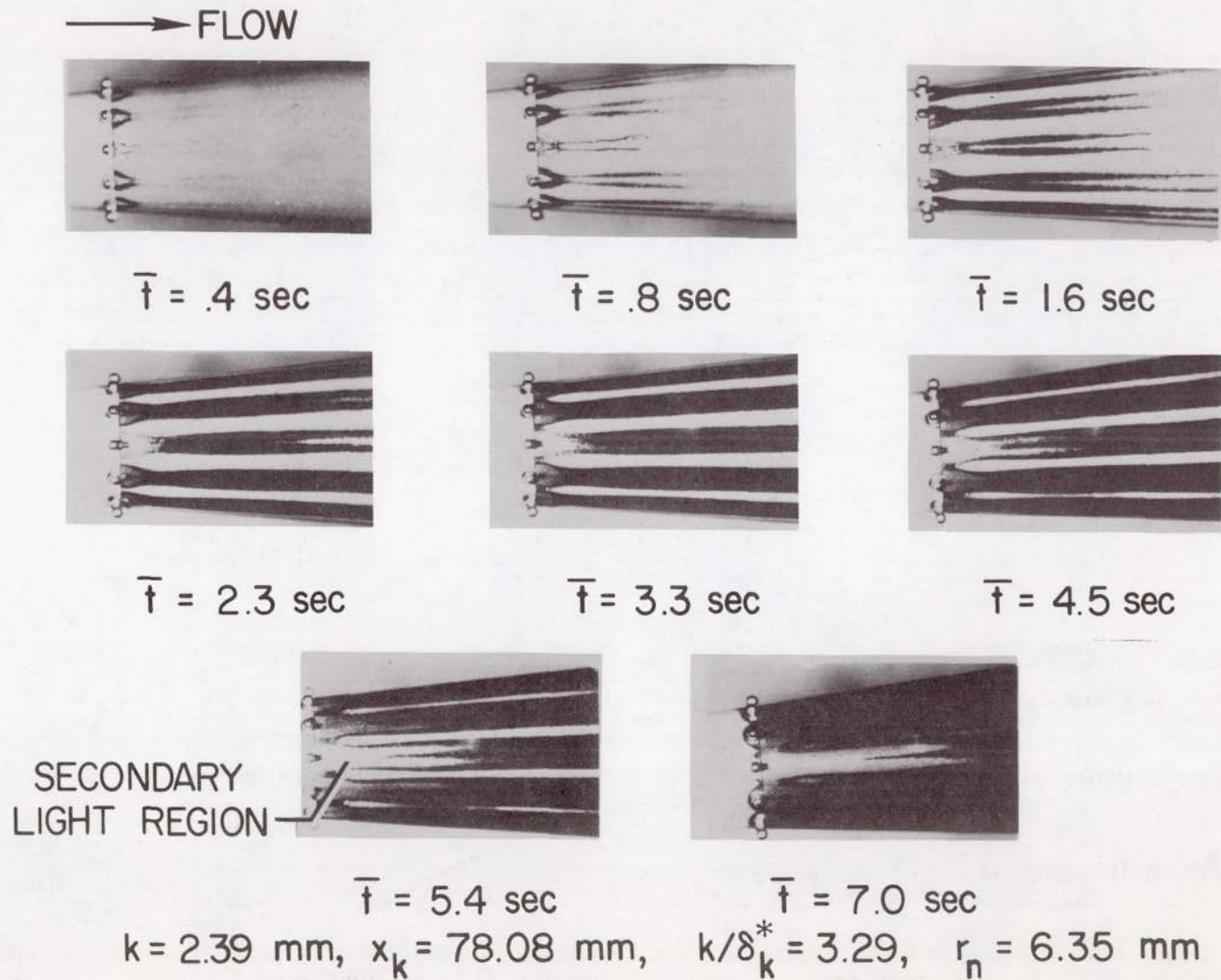
Figure 21.- Temperature-sensitive-paint patterns in vicinity of spherical roughness elements.       L-68-8597
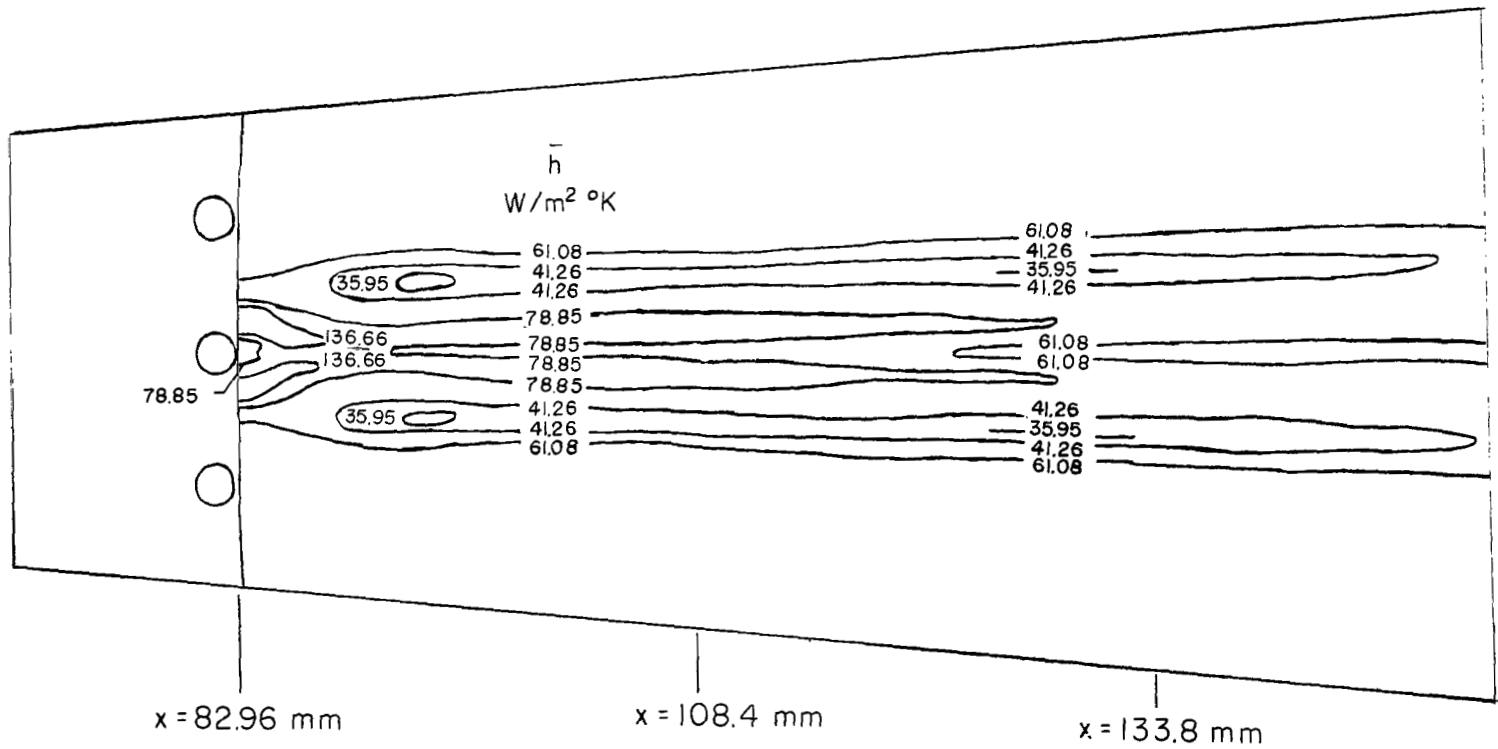
Figure 22.- Heat-transfer distribution behind a row of spherical roughness elements. $r_n$ = 6.35 mm; $k/\delta_k^*$ = 3.29.

Double row spheres

$r_n$ = 2.54 mm

k = 1.19 mm

$x_k$ = 50.06 mm
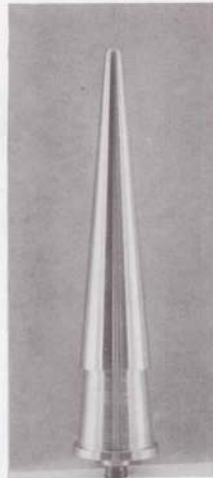


Annular groove

$r_n$ = 2.54 mm

k = 1.27 mm

$x_k$ = 94.00 mm
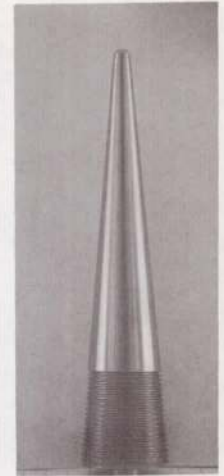


Screw threads

$r_n$ = 2.54 mm

k = 1.27 mm

$x_k$ = 94.00 mm
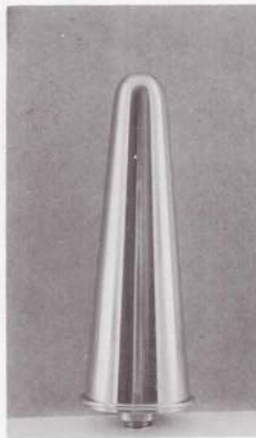


Two-dimensional wire

$r_n$ = 6.350 mm

k = 1.27 mm

$x_k$ = 78.64 mm
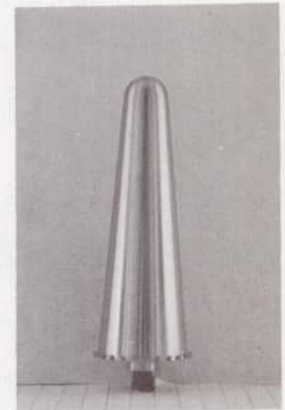


Cylinders

$r_n$ = 6.350 mm

k = 1.194 mm

$x_k$ = 78.64 mm

d = 1.194 mm

Figure 23.- Various types of roughness geometry.

L-68-8598
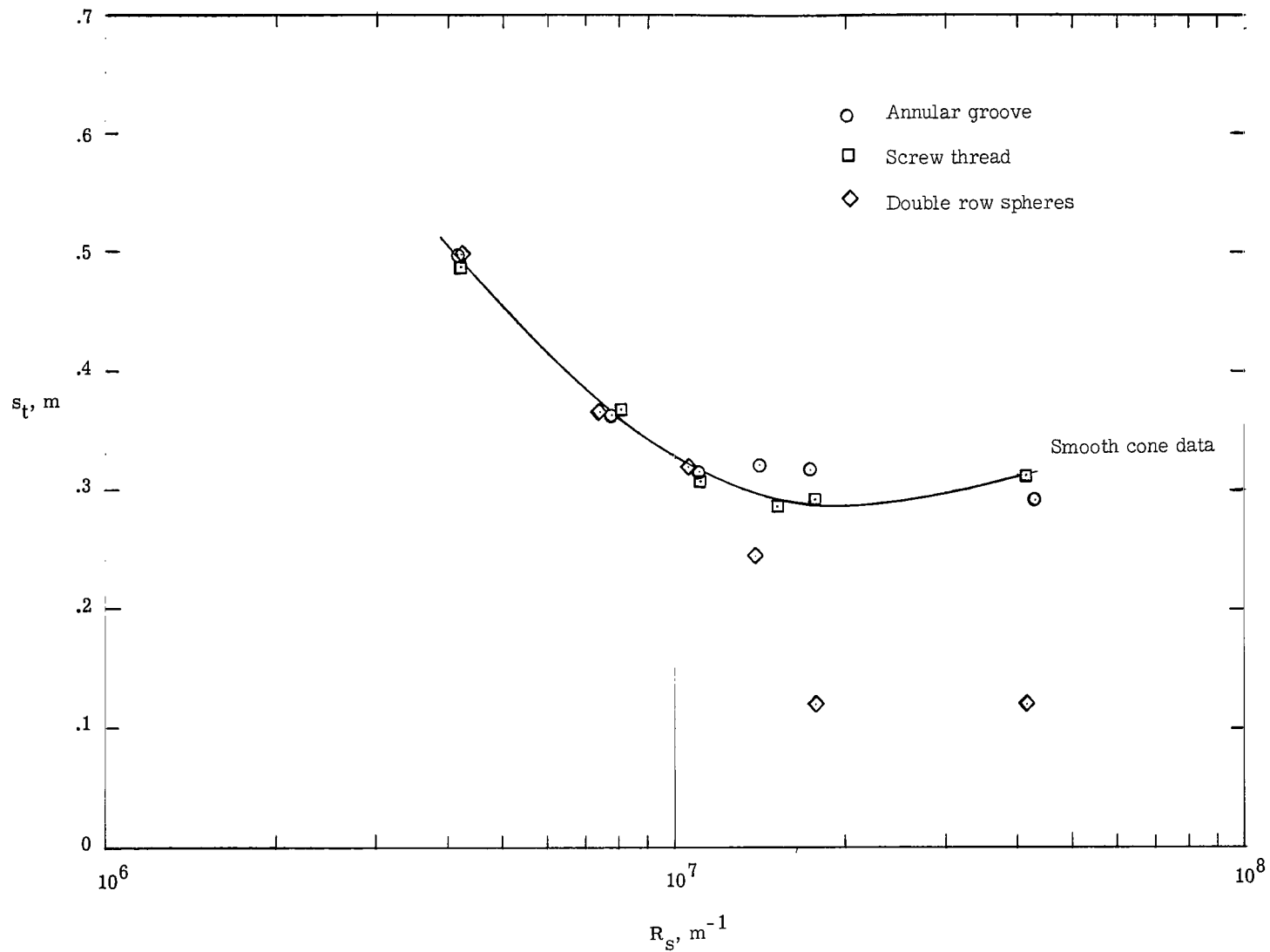
(a) $r_n$ = 2.54 mm.

Figure 24.- Effect of various types of roughness on the location of transition.
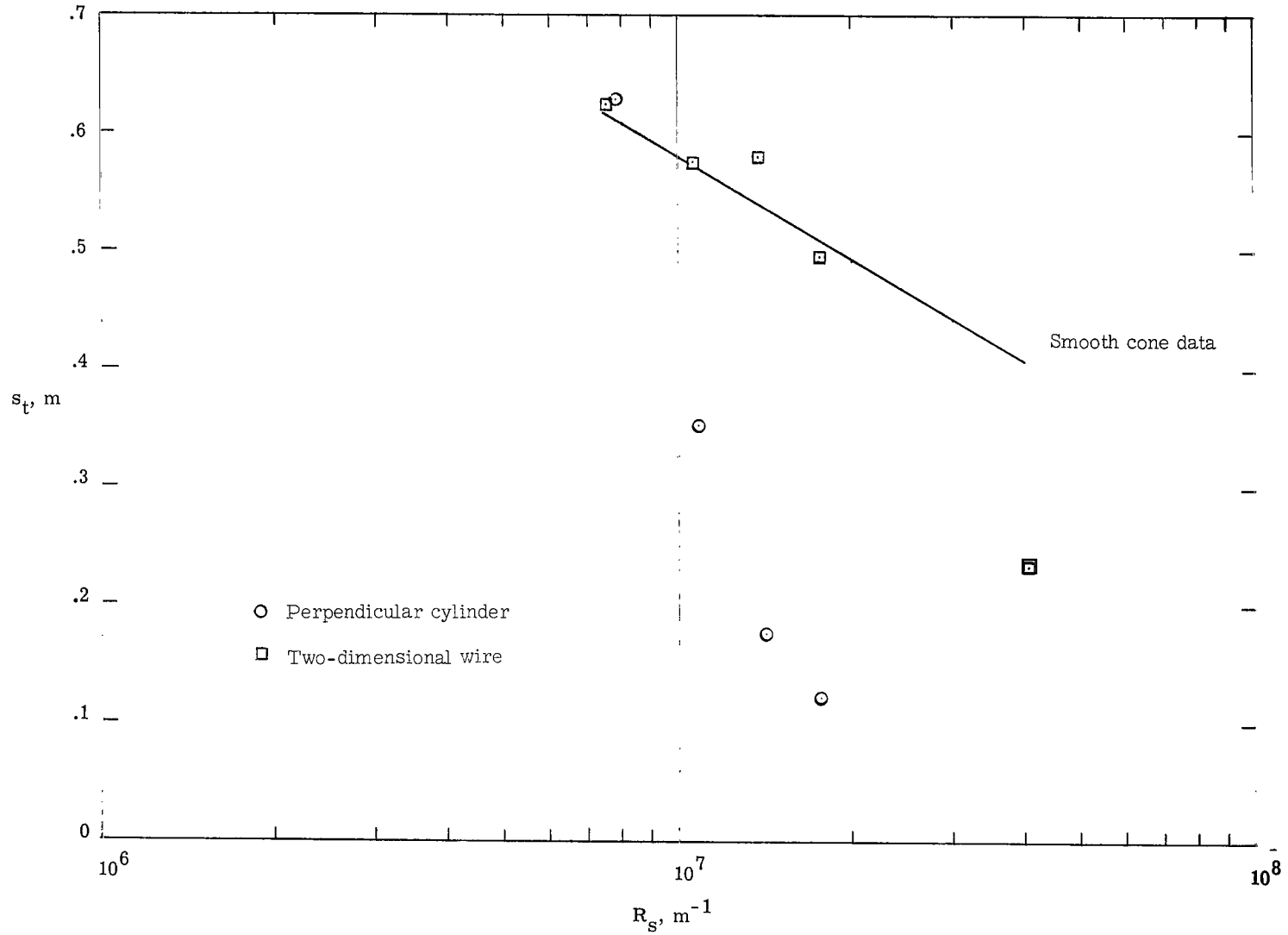
(b) $r_n$ = 6.35 mm.

Figure 24.- Concluded.

Legend:

○　Single row of spheres (k = 1.19 - 3.18 mm)

□　Annular groove (2.29 x 11.4 mm)

◇　Screw threads (1.22 x 1.22 x 25.4 mm)

△　Double row spheres (k = 1.19 mm)

$s_k$　Annular groove and screw thread

$s_k$　spheres
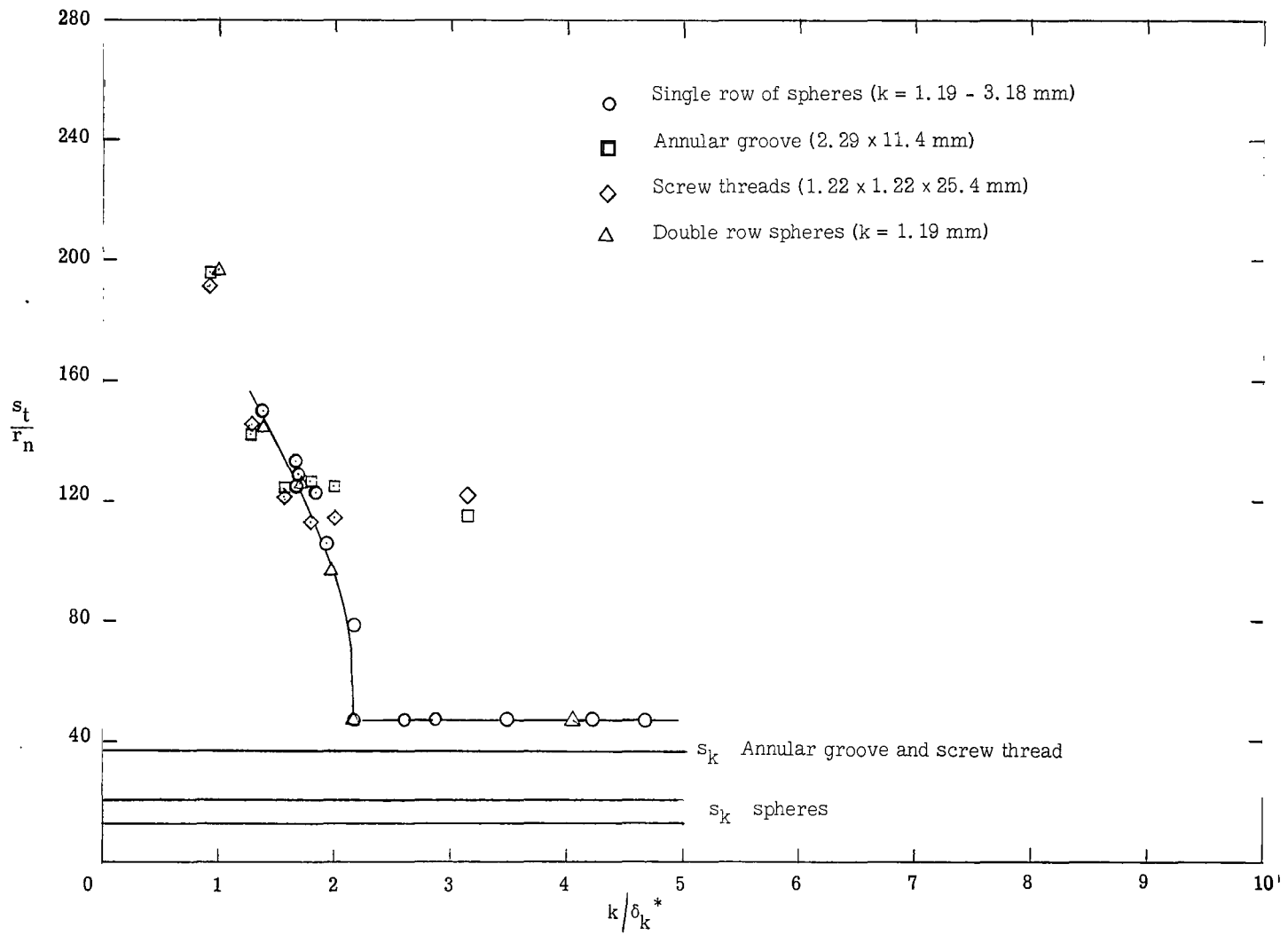
(a)  $r_n$ = 2.54 mm.

Figure 25.- Effect of various types of roughnesses on the location of transition.

Single row spheres (k = 1.19 to 3.18 mm)

Single row cylinders (1.19 x 1.19 mm)

Two-dimensional wire (k = 1.22 mm)
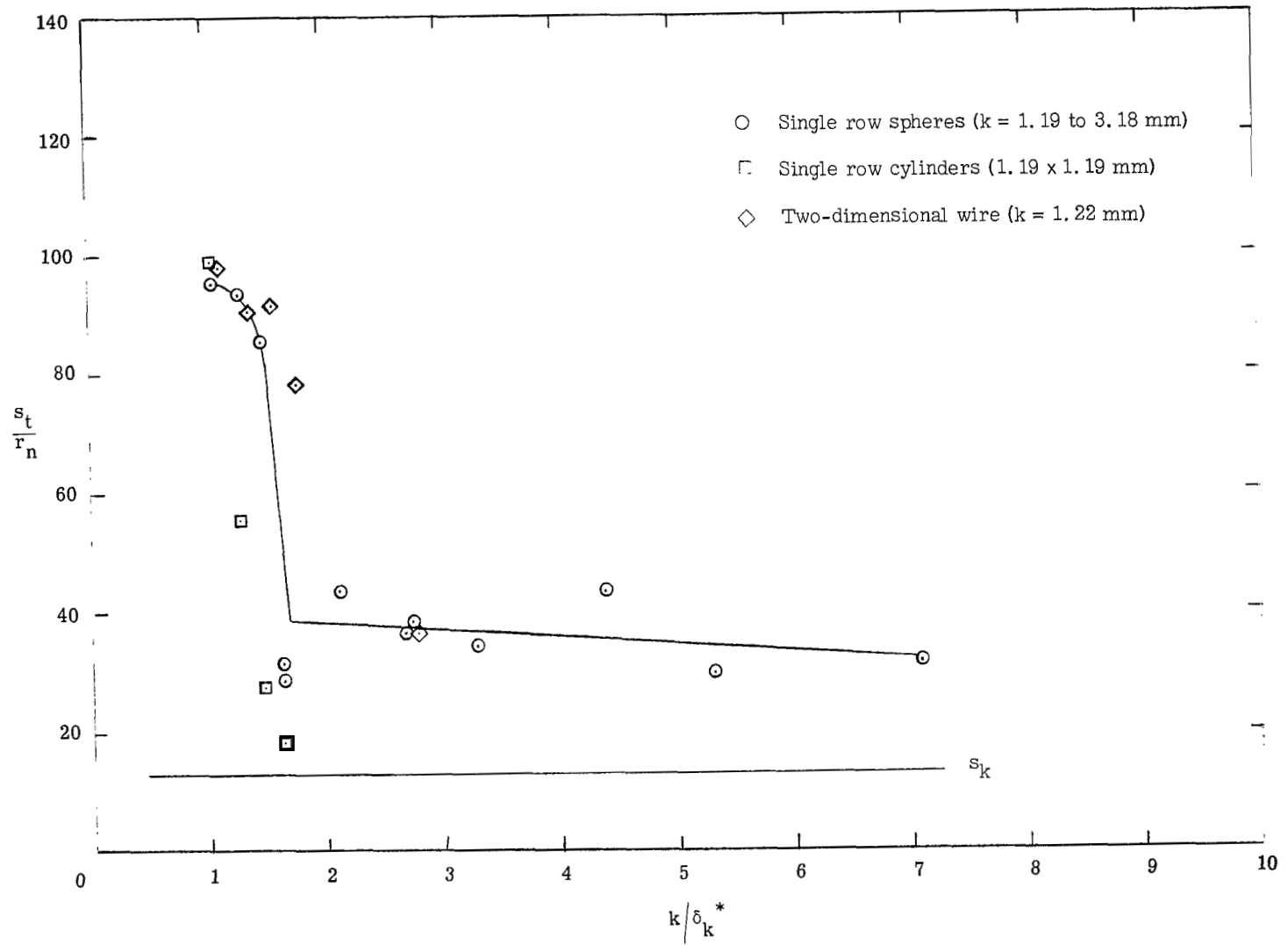
(b)  $r_n$ = 6.35 mm.

Figure 25.- Concluded.
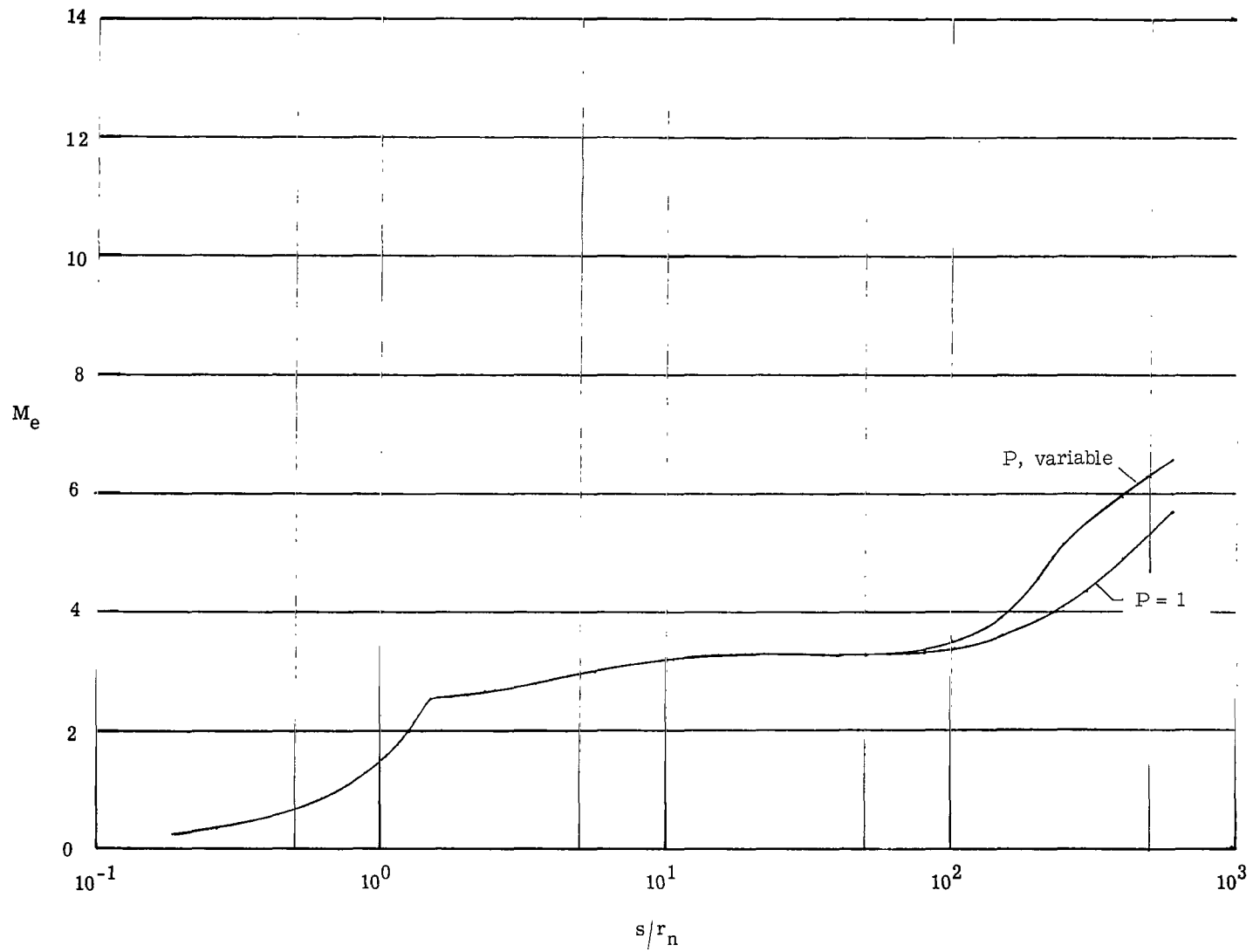
(a) Mach number.

Figure 26.- Effect of shear layer parameter $P$ on local fluid properties. $R_{0,r_n} = 10^7$.
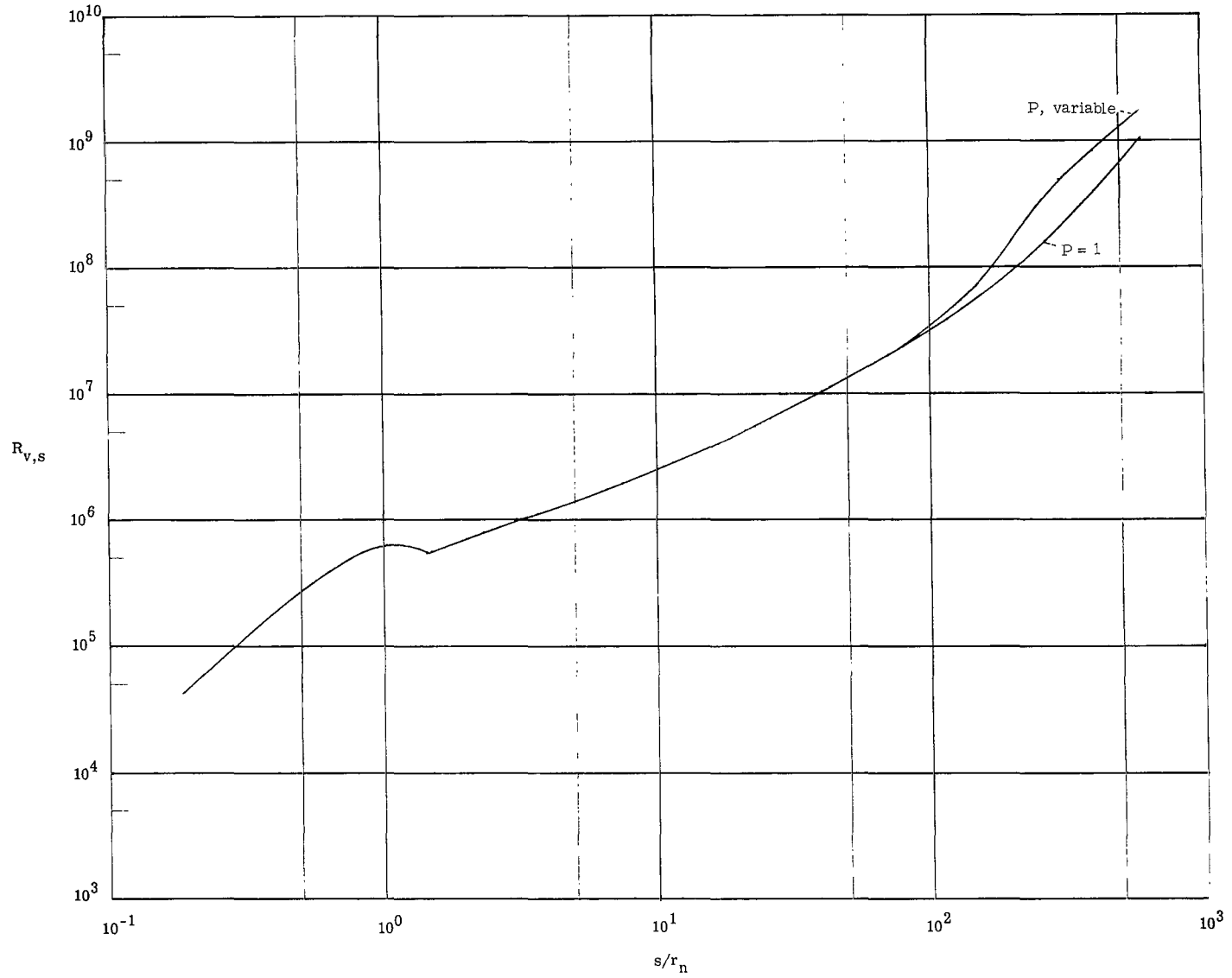
(b) Reynolds number.

Figure 26.- Concluded.
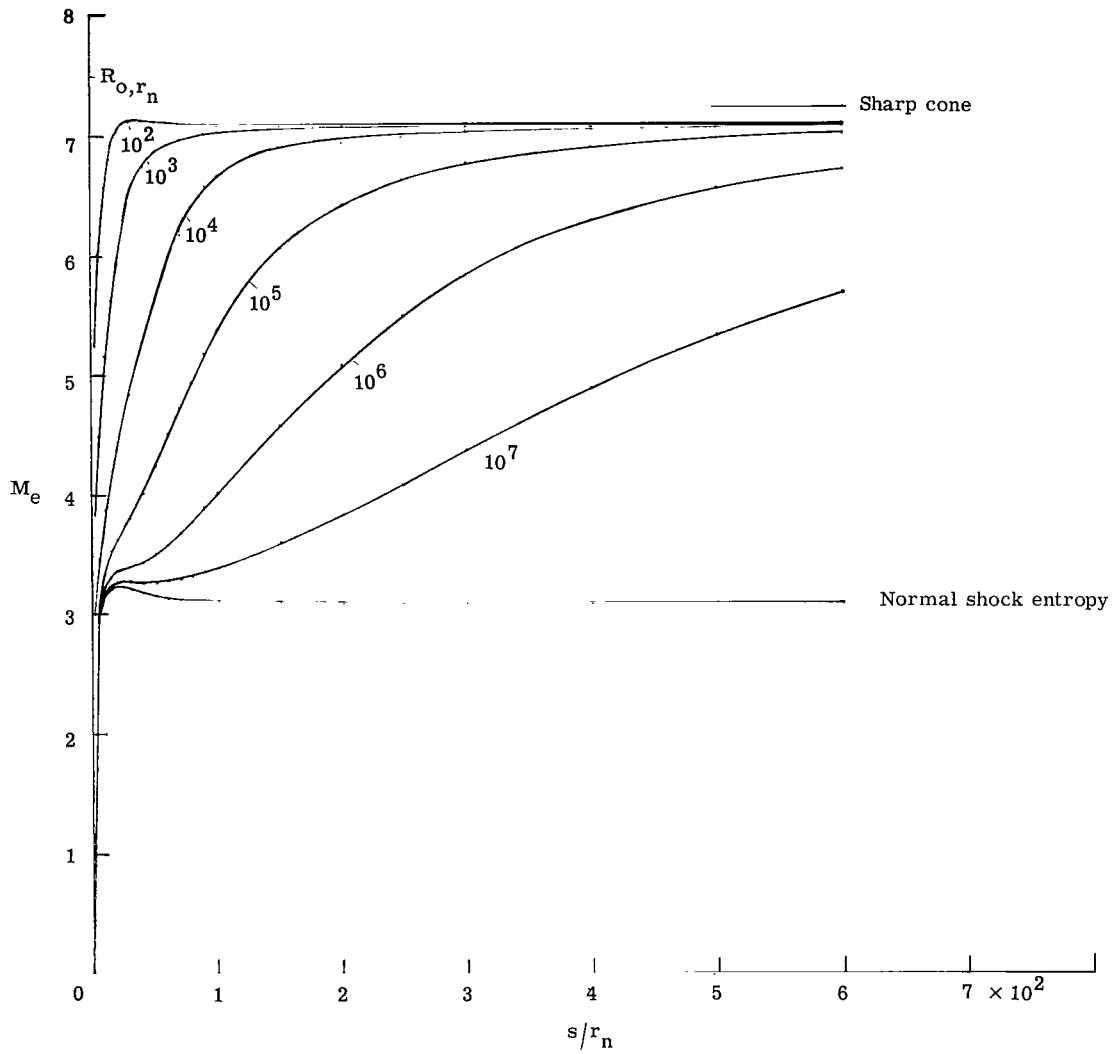
(a) Mach number.

Figure 27.- Effect of variable entropy on conditions at the edge of the boundary layer of a $5^0$ cone. $P = 1$.
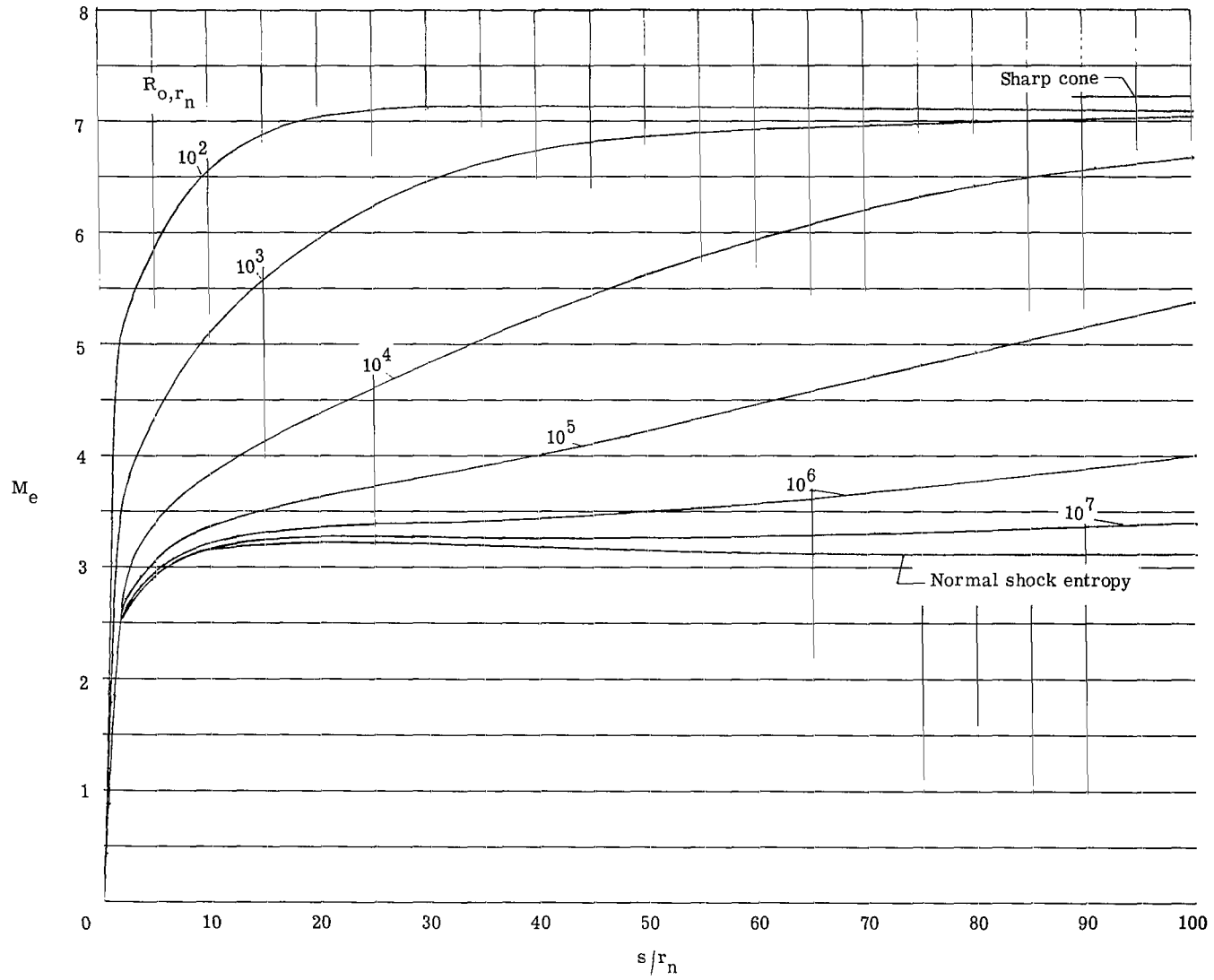
(b) Mach number.

Figure 27.- Continued.
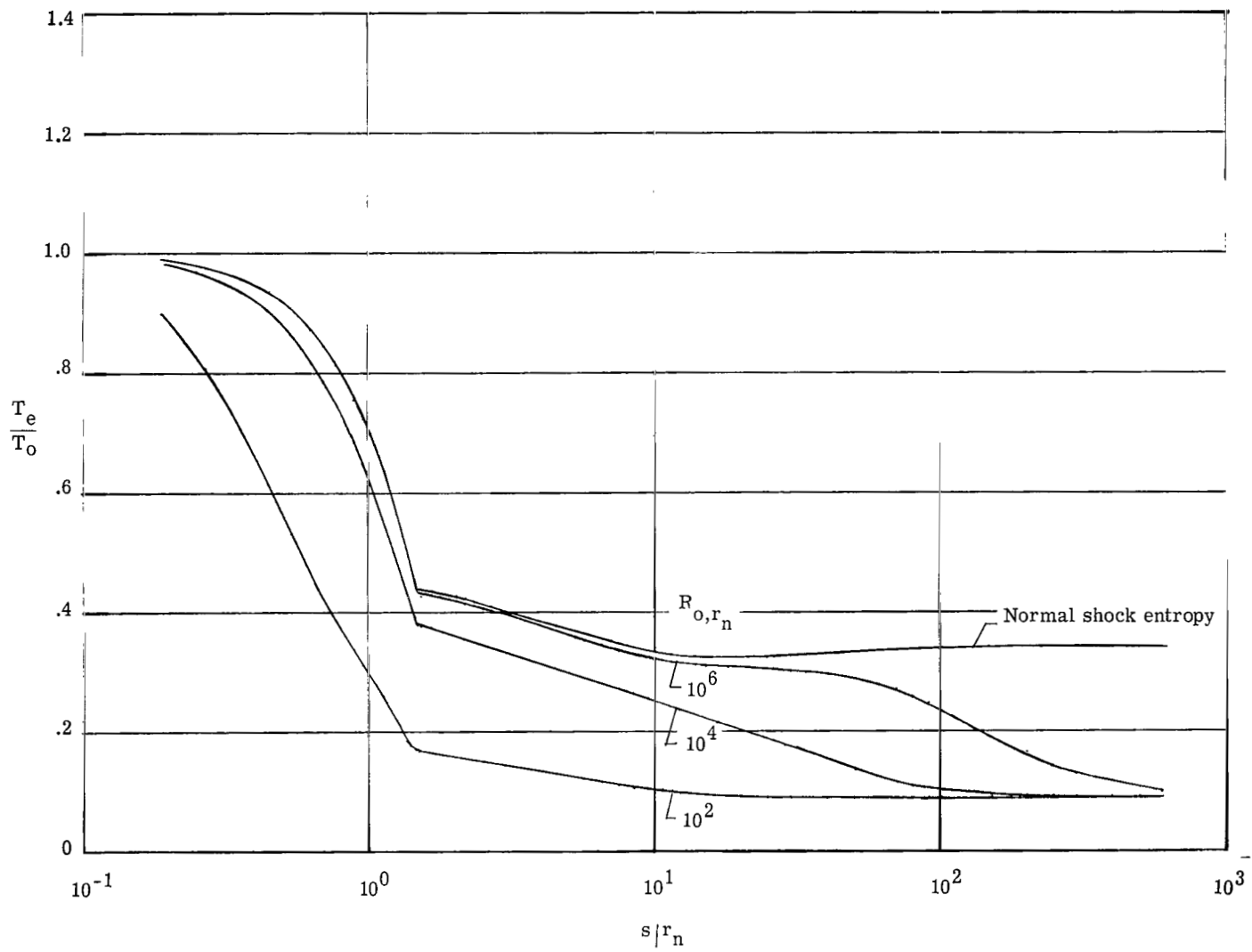
(c) Static temperature.

Figure 27.- Continued.
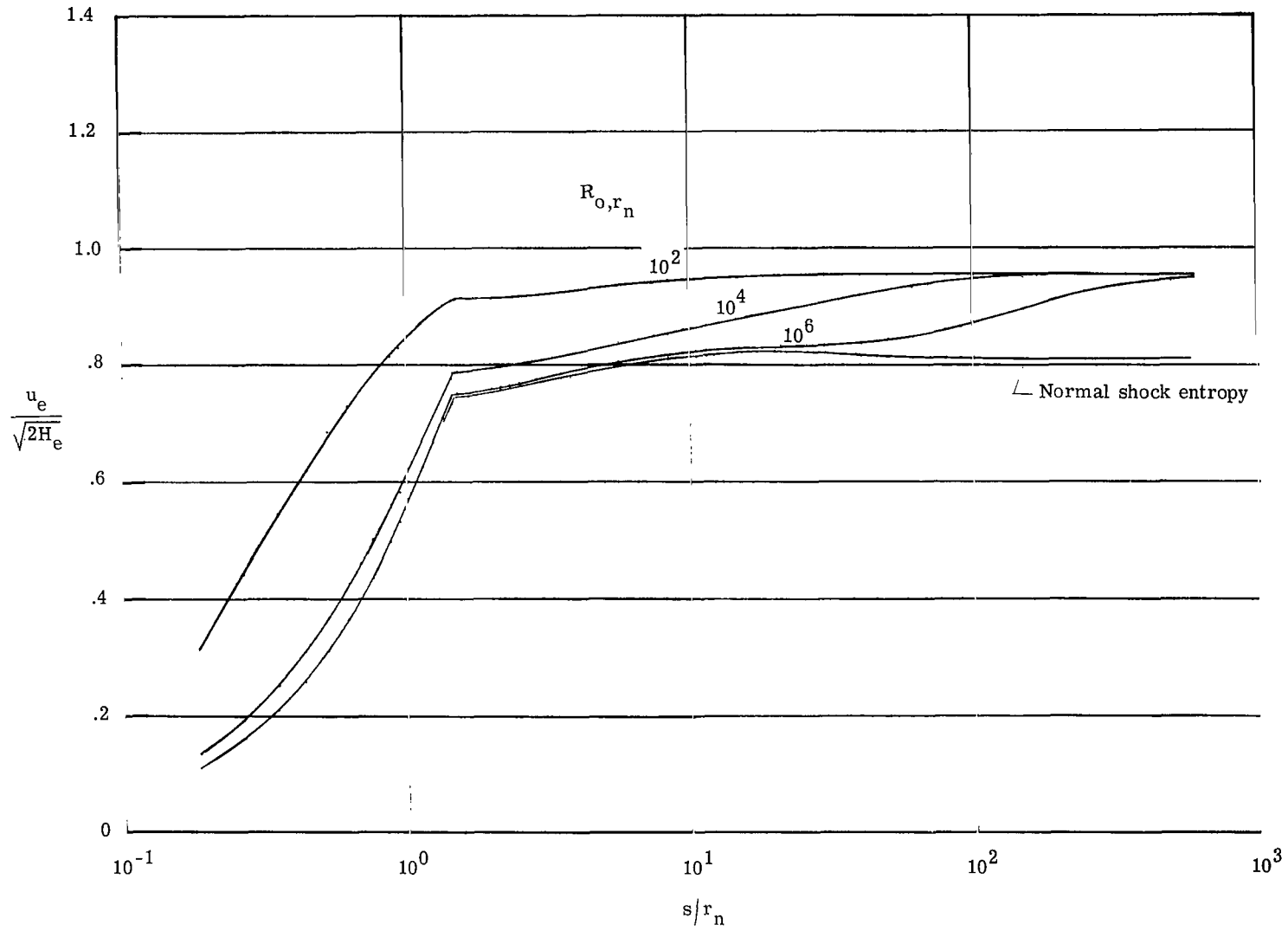
(d) Velocity.

Figure 27.- Concluded.
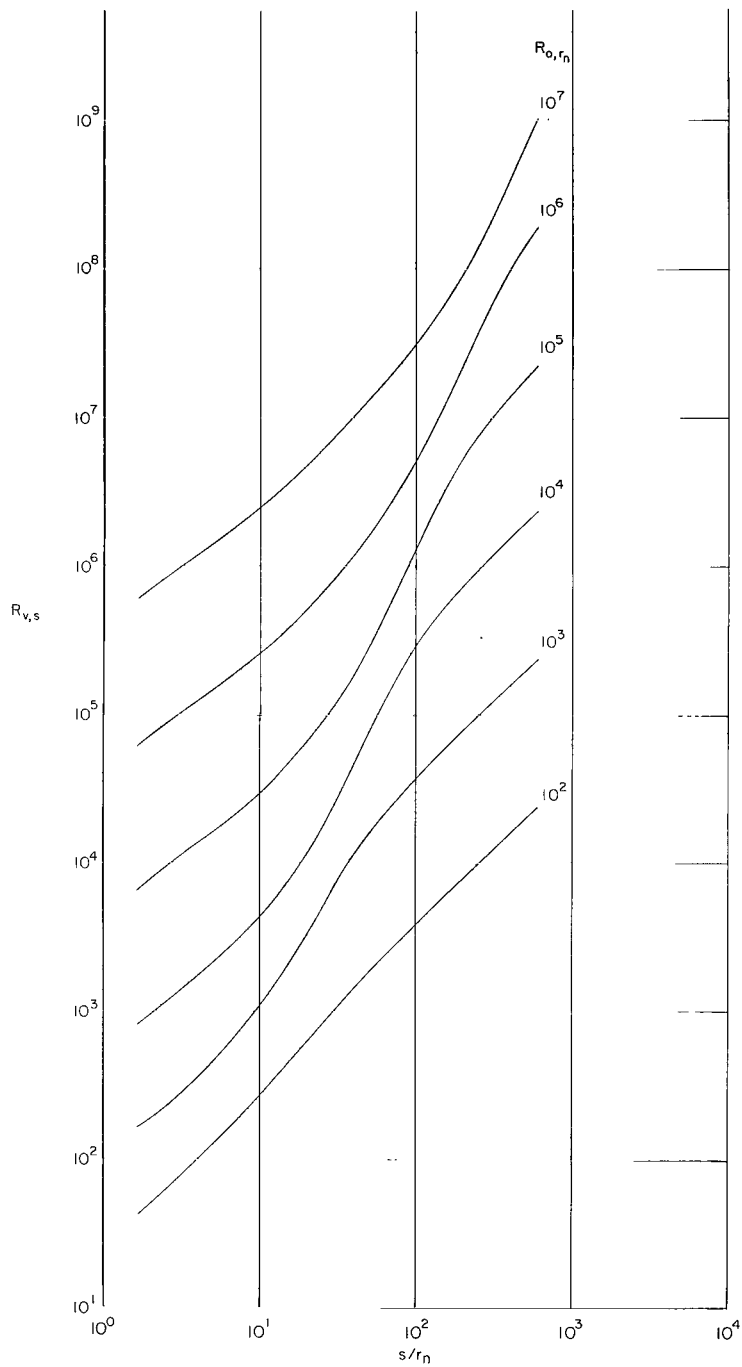
Figure 28.- Reynolds number based on variable-entropy conditions as a function of nondimensional surface distance. $P = 1$; $\theta_c = 5^0$; $M_\infty = 8$.

67
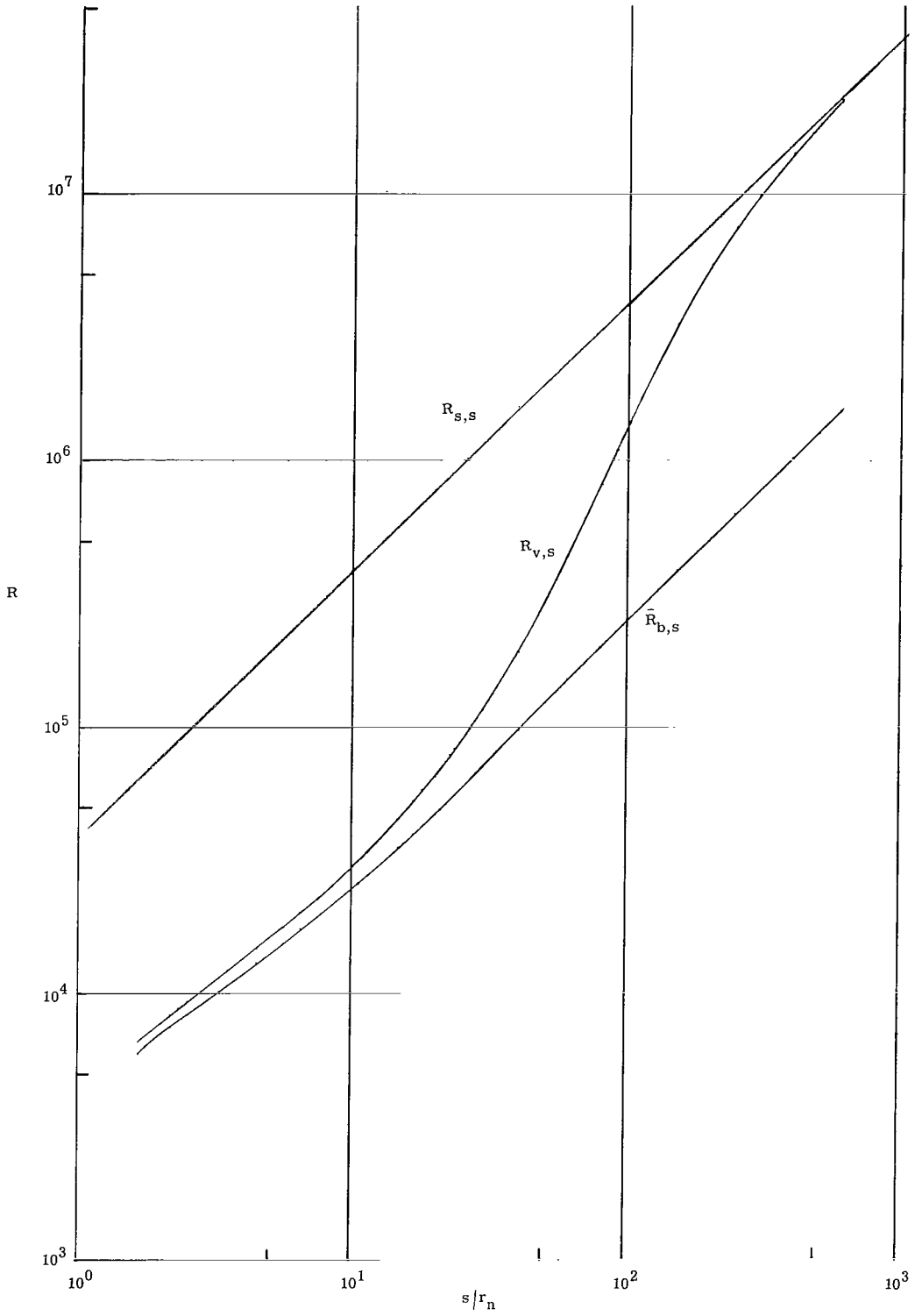
Figure 29.- Comparison of blunt-body constant-entropy and variable-entropy Reynolds number. $R_{0,r_n} = 10^5$; $P = 1$; $\theta_c = 5^0$.
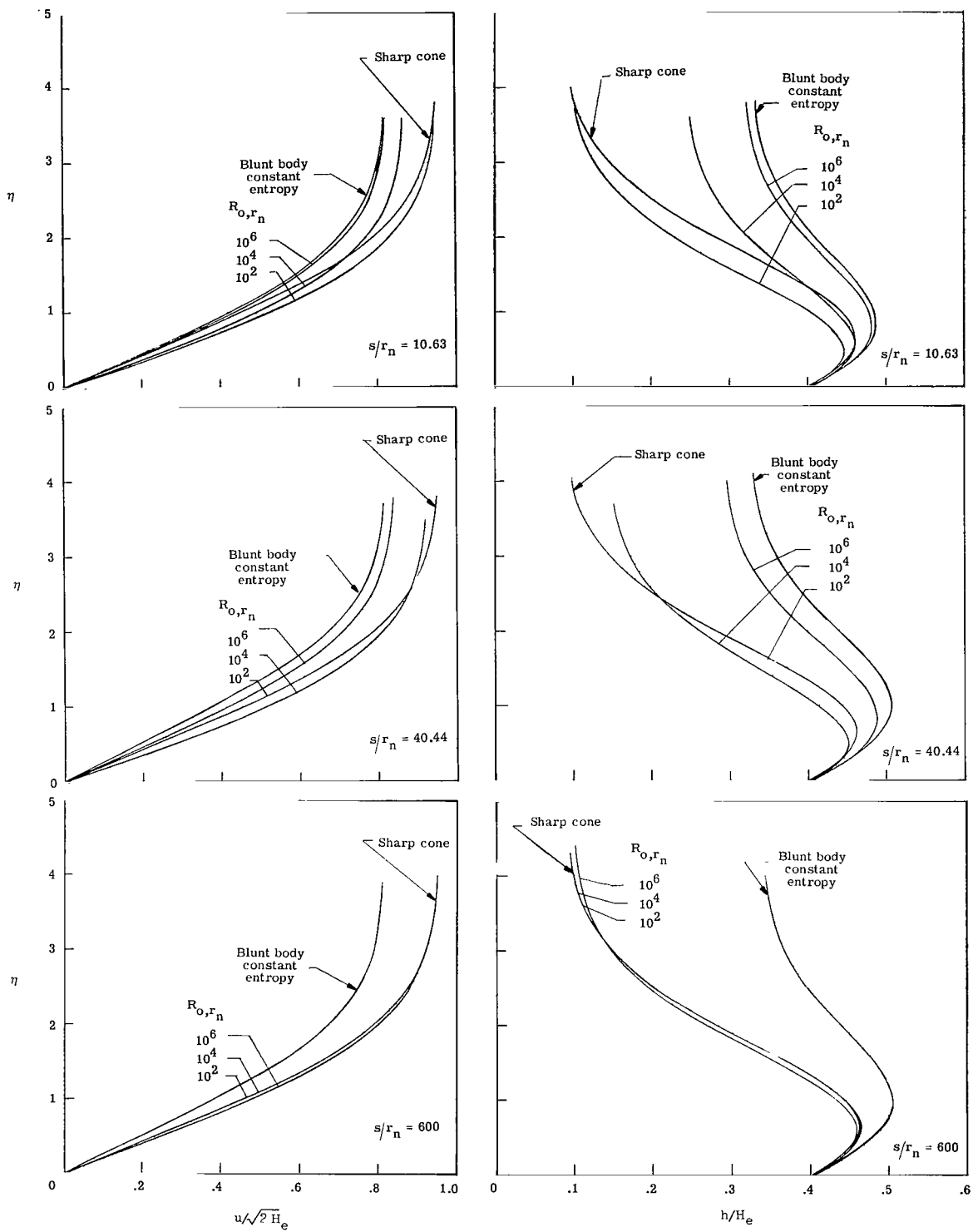
Figure 30.- Comparison of laminar boundary-layer profiles for constant- and variable-entropy methods. $P = 1$; $\theta_c = 5^0$.
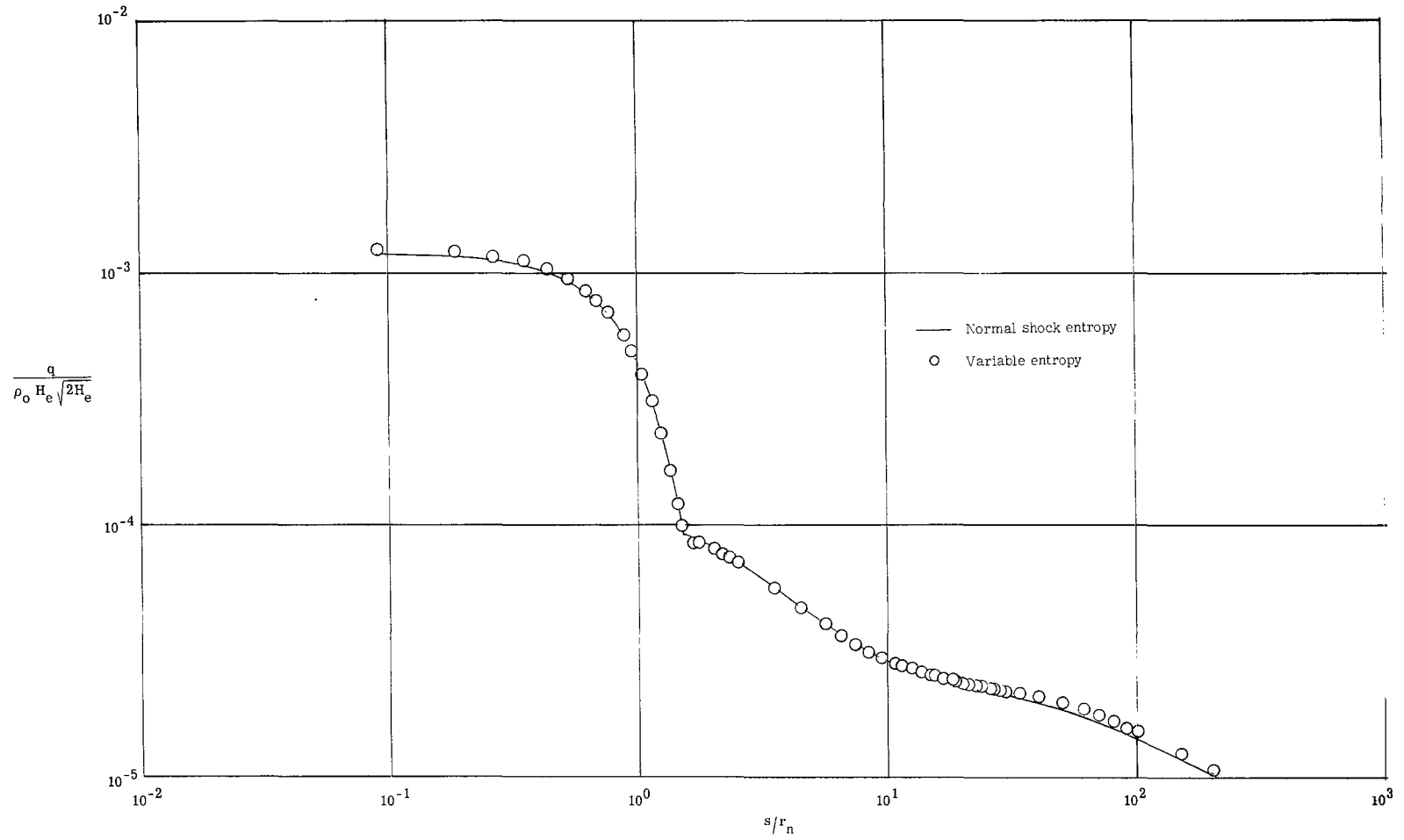
Figure 31.- Comparison of theoretical heating rate for constant- and variable-entropy conditions. $P = 1$; $\theta_c = 5^0$.
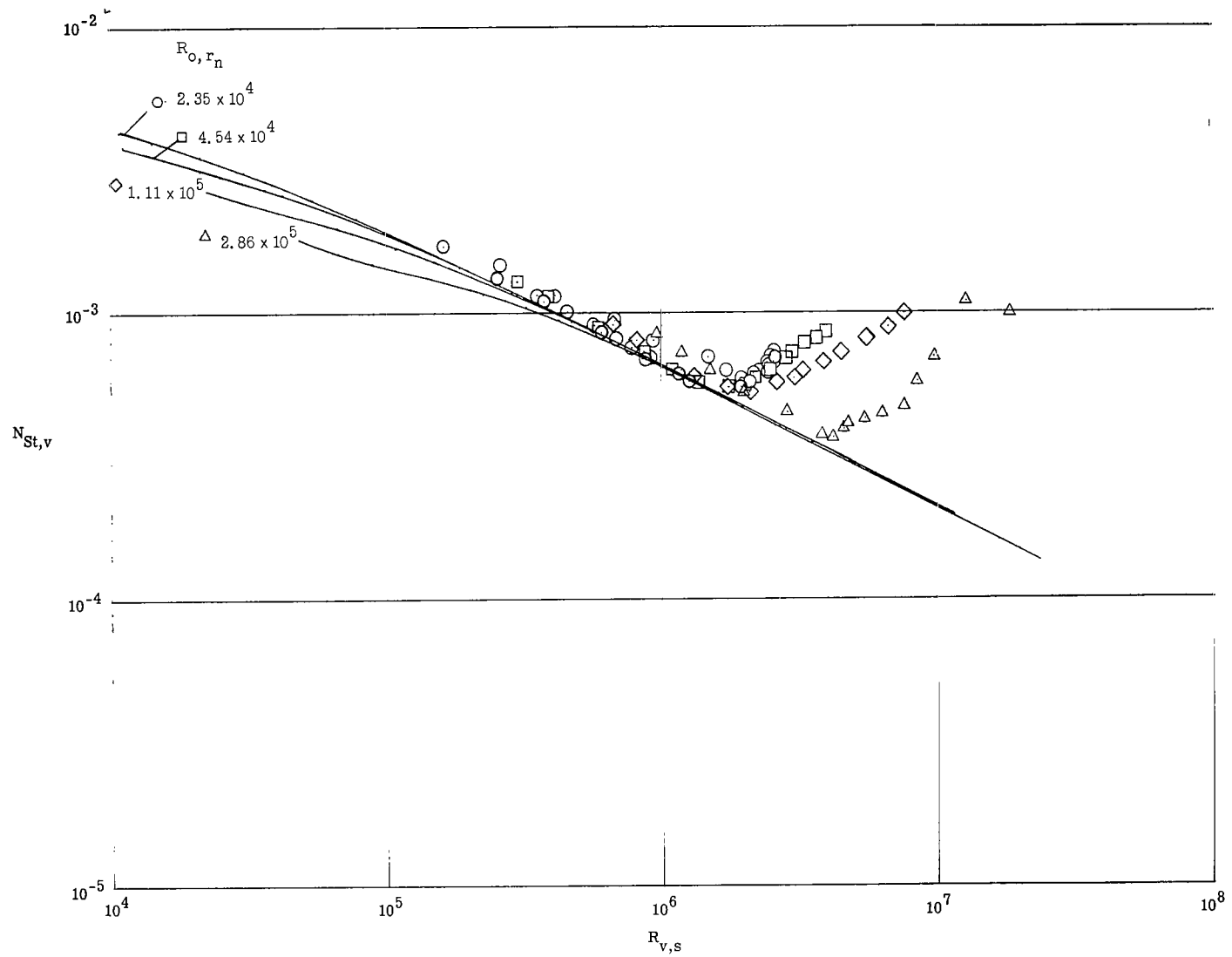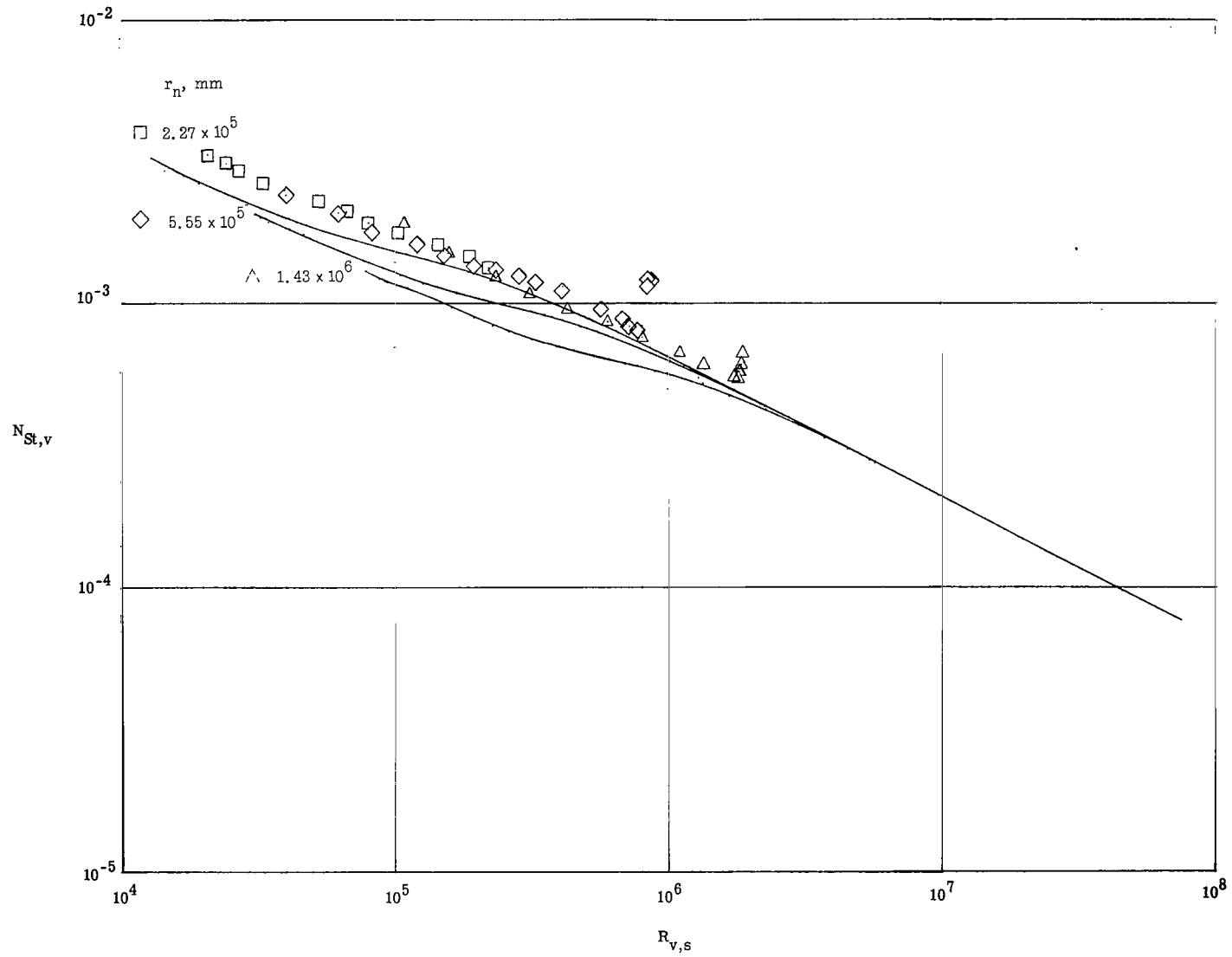
(a) $r_n = 2.54$ mm.

Figure 32.- Effect of variable entropy on the Stanton-Reynolds number variation for a blunt cone.
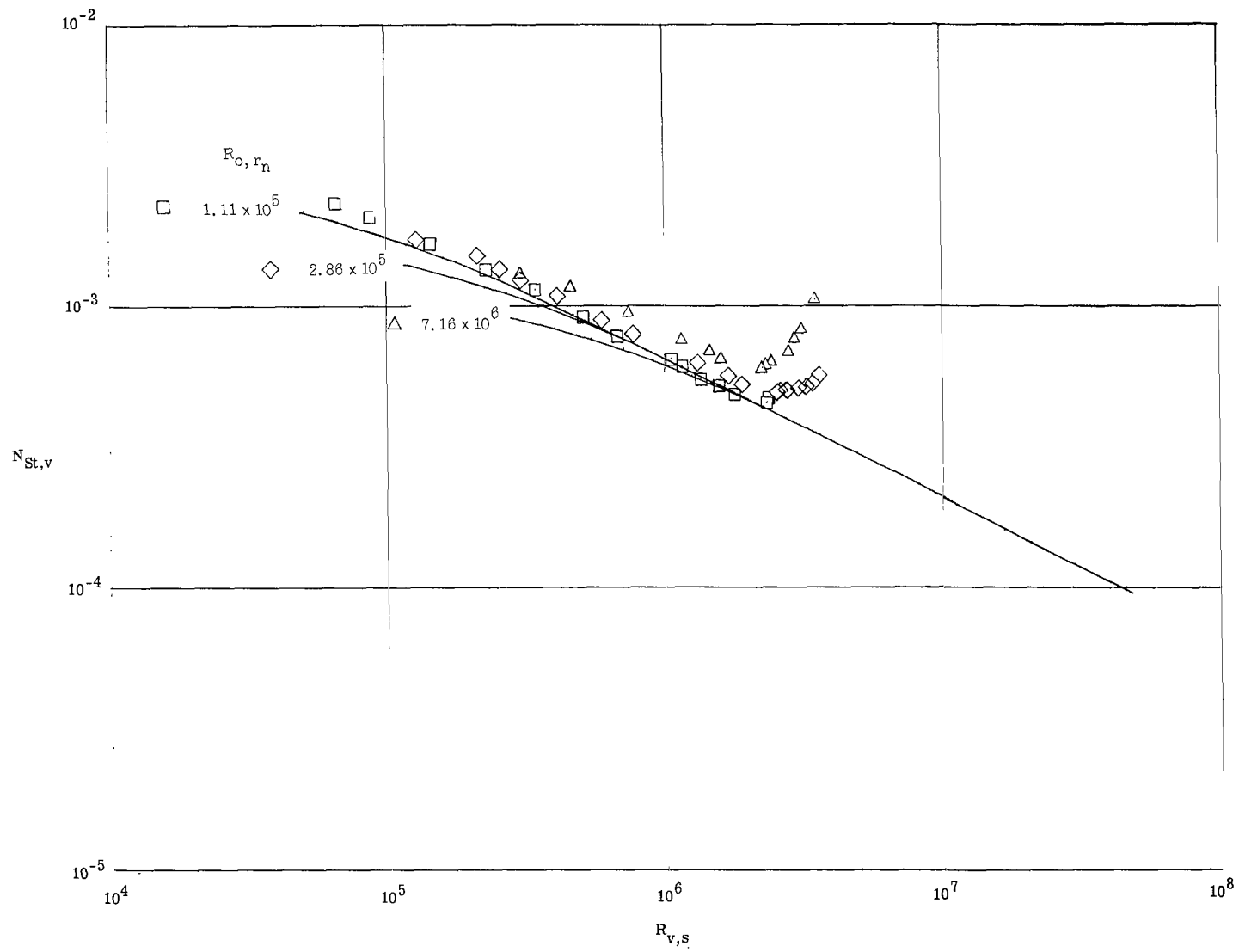
(b)  $r_n$ = 6.35 mm.

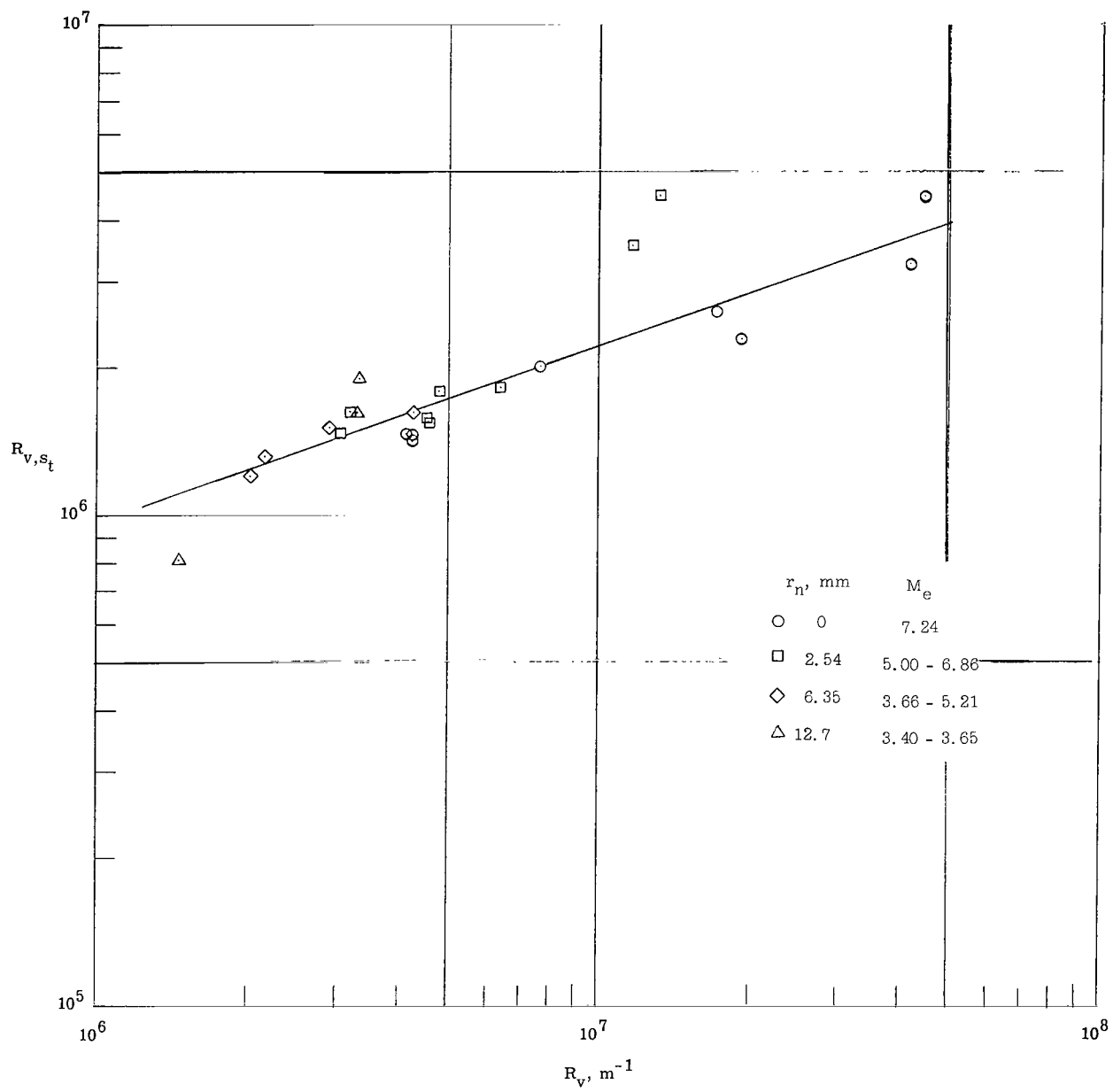Figure 32.- Continued.

(c)  $r_n$ = 12.7 mm.

Figure 32.- Concluded.

Figure 33.- Effect of variable-entropy unit Reynolds number on transition Reynolds number.
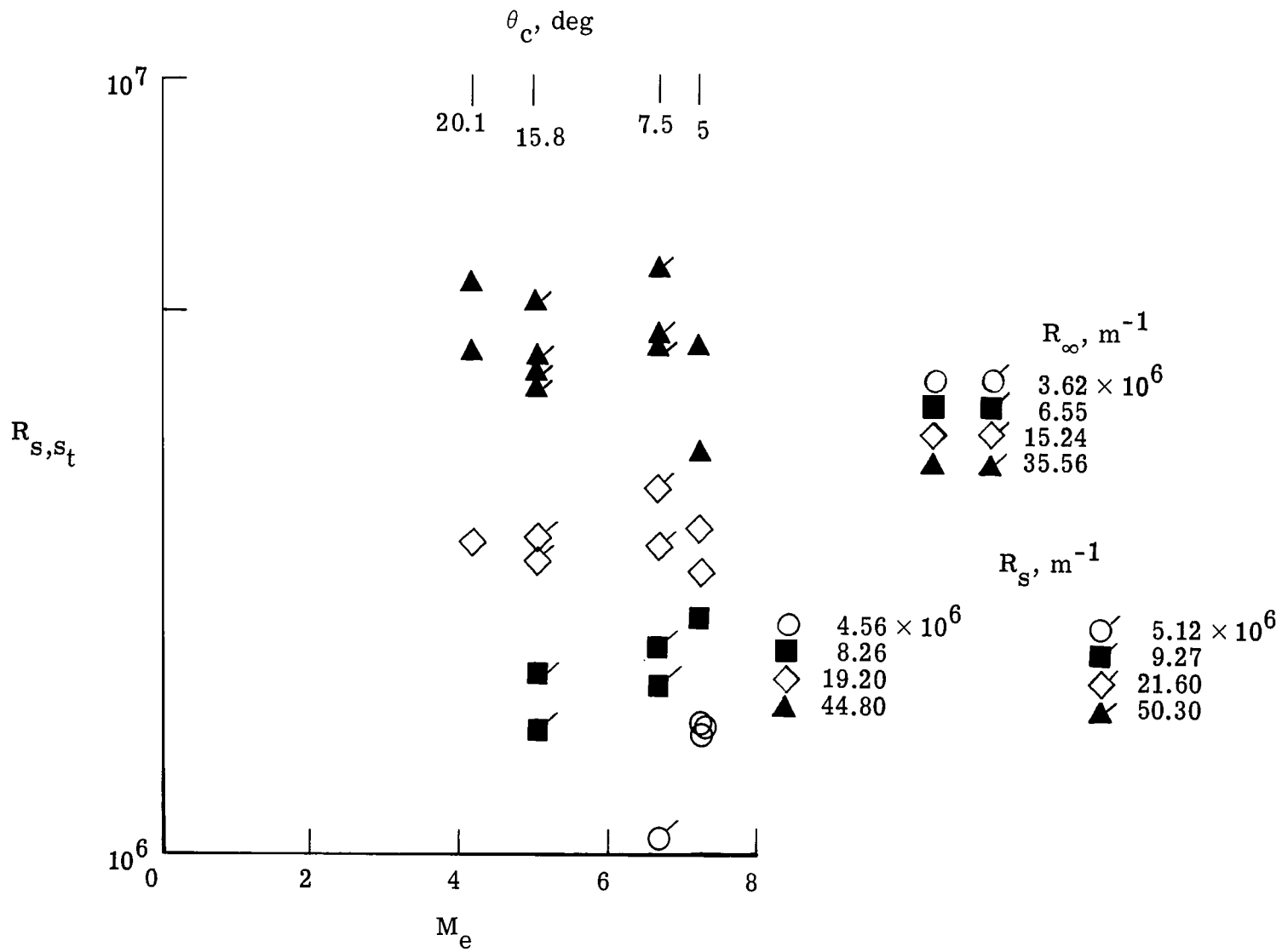
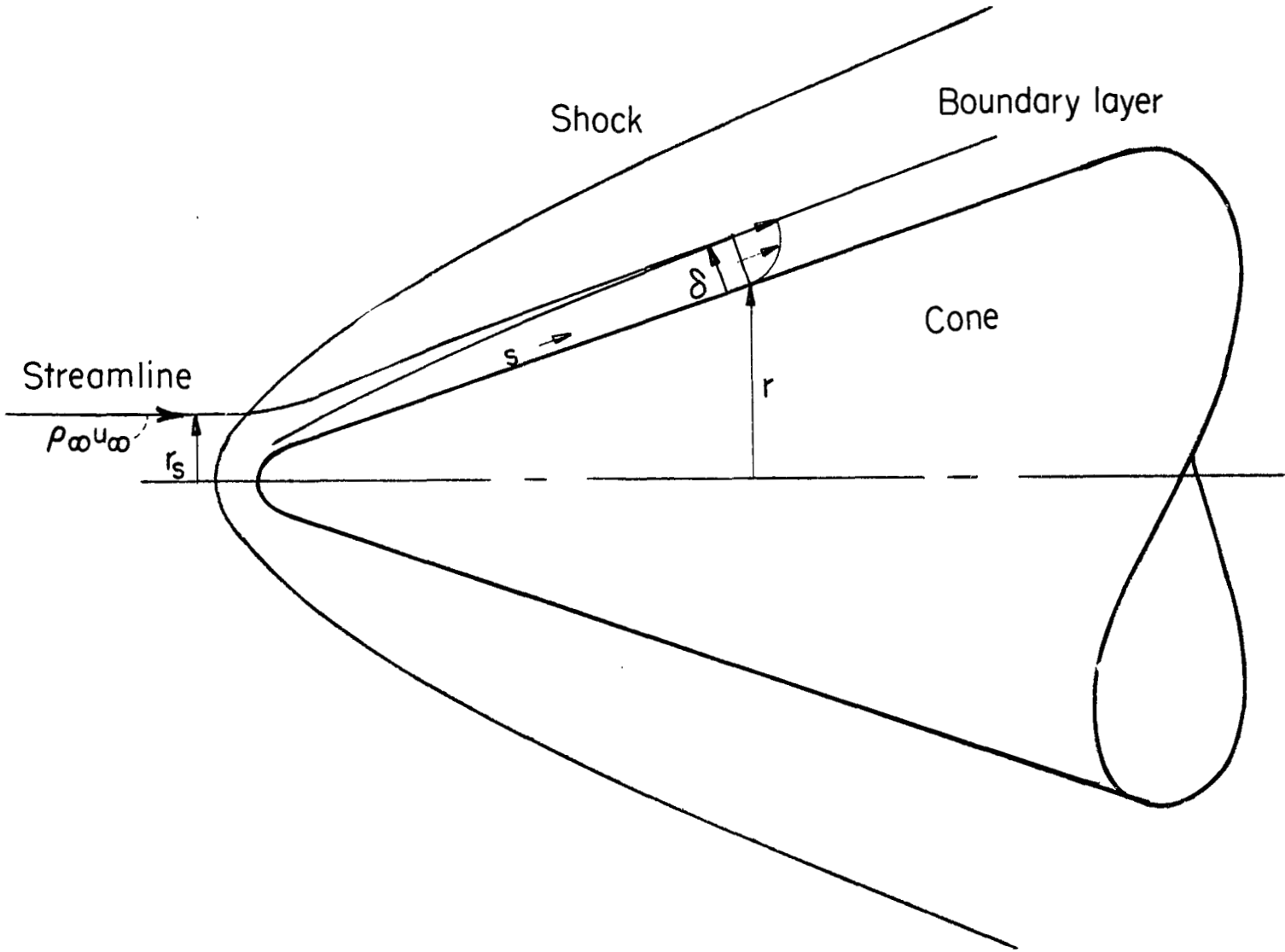Figure 34.- Transition Reynolds number for sharp cones with various semiapex angles. $M_\infty = 8$.

Figure 35.- Flow geometry for variable-entropy boundary-layer calculations.

"*The aeronautical and space activities of the United States shall be conducted so as to contribute . . . to the expansion of human knowledge of phenomena in the atmosphere and space. The Administration shall provide for the widest practicable and appropriate dissemination of information concerning its activities and the results thereof.*"

— NATIONAL AERONAUTICS AND SPACE ACT OF 1958

# NASA SCIENTIFIC AND TECHNICAL PUBLICATIONS

TECHNICAL REPORTS: Scientific and technical information considered important, complete, and a lasting contribution to existing knowledge.

TECHNICAL NOTES: Information less broad in scope but nevertheless of importance as a contribution to existing knowledge.

TECHNICAL MEMORANDUMS: Information receiving limited distribution because of preliminary data, security classification, or other reasons.

CONTRACTOR REPORTS: Scientific and technical information generated under a NASA contract or grant and considered an important contribution to existing knowledge.

TECHNICAL TRANSLATIONS: Information published in a foreign language considered to merit NASA distribution in English.

SPECIAL PUBLICATIONS: Information derived from or of value to NASA activities. Publications include conference proceedings, monographs, data compilations, handbooks, sourcebooks, and special bibliographies.

TECHNOLOGY UTILIZATION PUBLICATIONS: Information on technology used by NASA that may be of particular interest in commercial and other non-aerospace applications. Publications include Tech Briefs, Technology Utilization Reports and Notes, and Technology Surveys.

*Details on the availability of these publications may be obtained from:*

## SCIENTIFIC AND TECHNICAL INFORMATION DIVISION

# NATIONAL AERONAUTICS AND SPACE ADMINISTRATION
Washington, D.C. 20546